THE UNIVERSITY *of* EDINBURGH

DIRECTION OF CELLULAR PROTRUSIONS

BY CURVATURE

Kim Martin

Thesis submitted for the degree of Doctor of Philosophy

Centre for Integrative Physiology

Edinburgh Medical School: Biomedical Sciences

The University of Edinburgh

2017

Contents

Declaration

I declare that:

(a) this thesis was composed by me;

(b) the work presented here is my own unless clearly stated otherwise; and

(c) the work has not been submitted for any other degree or professional qualification

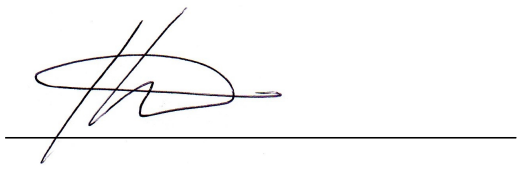

Kim Martin

Dedication

CHARLES JAMES DELMAR MARTIN

1949-2005

"My daughter is going to get a PhD some day."

Acknowledgements

I have much to be grateful for, and many to be grateful to. Some people I must mention:

Dr Melanie Lawrence and **Dr Elise Cachat** for friendship and tremendous support when I needed it the most.

Weijia Liu, **Roland Partridge**, **Chris Mills**, **Dr C-Hong Chang**, and other members of the Davies lab, past and present, for helping to create the collegial environment that made my time with the group so special.

Dr Mike Allerhand for introducing me to a powerful and satisfying tool through his "Introduction to R Programming" short course.

Dr Huabing Yin, **Dr Xiaofei Yuan**, and **Yahua Chim** for providing the variable-curvature micropatterns that this work is based on, and for the Atomic Force Microscopy (AFM) data.

Greg Stimac and **Kieran Bannerman** for tolerating my training, and for carrying out the initial work that motivated this thesis.

Professor Jamie Davies for gentle and effective direction, and for inspiring me with his vision of Synthetic Morphology.

The Anatomical Society for funding, encouragement, and the opportunity to present at Meetings. The Anatomical Society is registered as a Charity (number 290469) in England and Wales, and is a Company Limited by Guarantee (Registered Number 1848115).

Heinrich, for carrying me through at the end.

Abbreviations and acronyms

AFM	atomic force microscopy
APTMS	(3-aminopropyl)trimethoxylsilane
Arp2/3	actin-related protein-2/3 complex
BAPTA-AM	1,2-bis-(2-aminophenoxy)ethane-N,N,N',N'-tetraacetic acid tetra(acetoxymethyl) ester
BDM	2,3-butanedione monoxime
BSA	bovine serum albumin
C1, -2, -3	concave micropattern edge segments (numbered 1-3); refer to Fig. 3.2B (p.22)
CaMKII	Ca2+ /calmodulin-dependent protein kinase II
CI	confidence interval
Da	Damköhler number
DAPI	4',6-diamidino-2-phenylindole
DMSO	dimethyl sulfoxide
EDTA	ethylenediaminetetraacetic acid
F1, -2	flat micropattern edge segments (numbered 1-2); refer to Fig. 3.2B (p.22)
FACS	fluorescence-activated cell sorting
FCS	fetal calf serum
FITC	fluorescein isothiocyanate
FRET	fluorescence resonance energy transfer
GFP	green fluorescent protein
Glycyl-H-1152	glycyl-H-1152 dihydrochloride; (S)-(+)-4-glycyl-2-methyl-1-[(4-methyl-5-isoquinolinyl)sulfonyl]-hexahydro-1H-1,4-diazepine dihydrochloride

HDAC6	histone deacetylase 6
ImageJ	ImageJ image-processing program (version V1.45s used in this work)
Lifeact-GFP	genetic construct consisting of an actin-binding peptide (Lifeact) fused with GFP
Lifeact-MDCK	cell line derived from MDCK II that constitutively expresses Lifeact-GFP
MDCK II	type II Madin-Darby Canine Kidney cell line
MLC	myosin light chain, also known as the regulatory light chain
MLCK	myosin light chain kinase
Myosin IIA	non-muscle myosin isoform IIA
PBS	phosphate buffered saline
PDGF	platelet-derived growth factor
Pe	Péclet number
PEG-silane	2-(Methoxy(polyethyleneoxy)$_{6\text{-}9}$propyl)trichlorosilane
PFA	paraformaldehyde
QV500	Quasi-Vivo QV500 flow culture chamber system
R	R statistical computing language (version 3.2.1 used in this work)
RhoA	ras homolog gene family, member A
ROCK	rho-associated protein kinase
ROI	region of interest
S1004A	S100 calcium-binding protein A4
SAM	self-assembled monolayer
siRNA	small interfering ribonucleic acid
Tensegrity	tensional integrity
TER	transepithelial resistance
TGFβ1	transforming growth factor β1

Tpm3.1	tropomyosin isoform 3.1
TRITC	tetramethylrhodamine isothiocyanate
TRPM7	transient receptor potential cation channel, subfamily M (melastatin-related), member 7
TRPV2, -4	transient receptor potential cation channel, subfamily V (vanilloid-related), members 2 and 4
V1, -2, -3	convex micropattern edge segments (numbered 1-3); refer to Fig. 3.2B (p.22)
Y-27632	(+)-(R)-trans-4-(1-aminoethyl)-N-(4-pyridyl)cyclohexanecarboxamide dihydrochloride

Lay summary

All tissues and organisms in the human body are ultimately derived from a single, undifferentiated cell. From that one cell comes the host of daughter cells that must, unaided by externally-delivered scaffolds or moulding forces (with the exception of gravity), position themselves with respect to each other in such a way as to build a cohesive whole. Morphogenesis – the development of structures from constituent cells – is akin to origami that folds itself. The cells pull each other and themselves, and together they direct the shape changes of the tissues they make up.

How cells pattern and direct themselves to do this is a fascinating area of study. Recent work has suggested that one of the cues that cells use to organise themselves is the curvature that they experience; cells behave differently when they find themselves at a region at the edge of a tissue that is curved inwards (concave) or outwards (convex). Cells exposed to convex curvatures are more inclined to protrude and move. This is interesting because this behaviour could explain why cells form finger-like structures under some conditions.

In this study, cells were confined on two-dimensional shapes with variable-curvature edges to test hypotheses about how they sense and respond to curvature. A previously-published work suggested that cells sense curvature by all secreting chemical signals, which collect in well-like concave regions and so are present in stronger doses to cells there. This work provides evidence against this idea, as flushing fresh liquid over the cells to wash away any chemical signals did not change the way they behaved.

Treating cells with drugs that interfere with their ability to sense and exert physical force did have some effects on their response to curvature, suggesting that the cells are able to sense curvature by how stretched out they are. In addition, cells at the most convex regions were shown to have characteristics that set them apart from those at other regions, giving more support to the idea that curvature may be a significant cue during tissue morphogenesis.

Abstract

Developmental processes involving symmetry-breaking of homogeneous cell populations into leaders and followers are found in many important contexts. Cells constrained by culture on two-dimensional scaffolds, as well as in three-dimensional shapes, appear to respond to convex curves with an increasing propensity to protrude, while concave curves in contrast appear to inhibit protrusion. This has interesting implications in terms of a potential positive feedback loop. This feedback may act in symmetry-breaking, through amplification of initial stochastic differences in cell shape, and also in collective migration, through reinforcing and directing the coherent movement of collectives.

In this study, epithelial cells were cultured on two-dimensional micropatterns with variable curvatures to examine the effect of edge geometry and other variables on the likelihood of protrusions forming. This platform allowed the quantification of F-actin-based protrusions at the periphery of multicellular epithelial clusters, in segments defined by cluster edge curvature. The initial observations confirmed reports in the literature of preferential localisation of protrusions at more convex regions, and relative inhibition at more concave regions.

A previously-published work has postulated a role for secreted modulators of motility, with the shape of a group of cells determining the concentration of diffusing morphogen each individual cell is exposed to. To test this hypothesis, a low-shear flow culture chamber was used to disrupt the putative gradients. Despite theoretical and empirical support for the sufficiency of the flow condition to disrupt autocrine signalling, micropatterned cells cultured under flow showed no significant differences from the control condition. These findings form the basis of a manuscript which has been accepted for publication by the Journal of Anatomy.

The results of an Atomic Force Microscopy (AFM) study carried out by collaborators were suggestive of a role for cellular mechanotransduction in sensing and responding to micropattern curvature. Differential calcium channel mechanoactivation was hypothesised as being one potential mechanism underlying the response to curvature, given the known involvement of mechanosensitive ion channels in cellular responses to force and substrate stiffness, and the multiple roles of calcium in cellular motility.

Artificially increasing cytosolic calcium levels with Ionomycin reduced protrusion rates at convex curves. However, treatment with BAPTA-AM to sequester intracellular calcium had no effect on protrusion rates. ROCK inhibitor, in contrast, increased protrusion rates at concave curves, and Blebbistatin increased protrusion rates globally. These results together are suggestive of differential control of myosin depending on local curvature: cyclic and driven by calcium-activation of MLCK in the convex regions (with lamellipodia undergoing protrusion-retraction cycles), versus sustained and controlled by ROCK in the concave regions (where lamellipodia are inhibited).

The unexpected finding that protrusions at convex regions were resistant to the actin cytoskeleton-disrupting drug Cytochalasin D may point to a role for a tropomyosin isoform in defining the differing mechanical characteristics of the actin cytoskeleton in response to local curvature. In addition, the previously-noted lack of effect of BAPTA-AM treatment (which has been shown to interfere with dynamic microtubules) is suggestive of a role for stabilised microtubules in protrusions at convex regions. These indications of unique characteristics to the protrusions promoted by convex curvature give added support to the curvature-protrusion feedback model, and its relevance to tissue morphogenesis.

In summary, this work provides evidence against a previously-published suggested mechanism for the curvature-protrusion feedback loop that is proposed to act during epithelial morphogenesis, and evidence in support of a role for a calcium-based mechanism in driving the initiation and maintenance of leader cells in migrating epithelial sheets. Further work is called for in characterising the protrusions promoted by convex curvature, and the mechanisms controlling them. This area is of significance in gaining greater understanding of tissue morphogenesis in pathogenesis and development, and of potential value in tissue engineering applications.

List of Figures

List of Tables

Chapter 1

INTRODUCTION

1.1 Patterning epithelial morphogenesis

All tissues and organisms in the human body are ultimately derived from a single, undifferentiated cell. From that one cell comes the host of daughter cells that must position themselves with respect to each other in such a way as to build a cohesive whole, unaided by externally-delivered scaffolds or moulding forces (with the exception of gravity). Morphogenesis – the development of structures from constituent cells – is akin to origami, without the need for pushing and pulling fingers. The cells pull each other and themselves, and together they direct the shape changes of the tissues they make up.

Epithelial morphogenesis is fundamental to metazoan evolution and development (Davies, 2013), and is an attractive subject for study, given its ubiquity and importance, and its frequently visually striking presentation. This is especially the case for the branching structures, which reflect exquisite control of tubule dimensions and positioning given the functional demands on the tissue.

Coordination between the individual cells making up epithelial sheets is crucial during morphogenesis, to restore and maintain the unbroken barrier that characterises functional epithelia. Some forms of collective migration are characterised by the emergence of specialised 'leader' cells, which are characterised by a highly migratory phenotype, and associated with large traction forces exerted against the underlying substrate (Reffay et al., 2014). In contrast, the 'follower' cells appear to be dragged passively behind the leader, although it has been shown that they extend protrusions under the cells in front of them, in a sign of active crawling (Farooqui and Fenteany, 2005).

Developmental processes involving symmetry-breaking of homogenous cell populations into leaders and followers are found in many important contexts. Branching morphogenesis is central to the construction of kidneys, lungs, and blood vessels, among others. Similarly, cases where groups of cells migrate collectively in clusters or flat sheets, with followers streaming behind leaders, can be seen in many key stages such as in wound healing and the early development of the vertebrate nervous system (Khalil and Friedl, 2010). This symmetry-breaking – from a homogenous sheet of cells to protruding fingers composed of leader cells at the tip and 'follower cells' bringing up the rear – relies on mechanisms that have yet to be made clear.

1.2 Role for geometry in directing leader cell initiation

Recent experimental work with cells in culture has directed increasing attention towards parameters such as cell shape as being a potential factor in directing symmetry-breaking of leaders and followers. Cells constrained by culture on two-dimensional scaffolds, as well as in three-dimensional shapes, appear to respond to convex curves with an increasing propensity to protrude, while concave curves in contrast appear to inhibit protrusion.

These responses can be shown to be proportional to the radius of curvature, which has interesting implications in terms of a potential positive feedback loop involved in symmetry-breaking (through amplification of initial stochastic differences in cell shape) and in collective migration-based developmental processes (through reinforcing and directing coherent movement of the collectives) (Davies, 2013; Mark et al., 2010).

The curvature-protrusion feedback model was proposed based on observations of epithelial cells in culture (Mark et al., 2010), which were reported to break symmetry when released undamaged from a linear boundary, and spontaneously form finger-like shapes with leader cells directing cohorts of followers (Poujade et al., 2007). Simulation of the model gave a good approximation of the empirical observations, supporting a possible role for this feedback loop in shaping collective processes in morphogenesis.

1.3 Curve sensing and response

While the empirical relationship between cell curvature and protrusion seems clear, the underlying mechanism controlling this phenomenon is not. There have been arguments made that the shape of a group of cells could modify the amount of diffusing morphogen sensed by each cell, dependent on the curvature of the edge it forms part of. For example, in a hypothetical case where all cells secrete an autocrine inhibitor of protrusion, the concentration of the inhibitor could be expected to be highest in 'pockets' where cells form a concave edge, thus inhibiting protrusion more effectively in concave regions (Nelson et al., 2006). Alternatively, arguments can be made for the application and sensing of differential tension by the cells in the collective being the mechanism by which curvature directs protrusion rate (Rausch et al., 2013).

Given the importance of directed migration of cell collectives in various contexts in development (and in pathologies such as cancer metastasis), an understanding of the underlying mechanisms would be invaluable. With the increasingly sophisticated methods of manipulating cell behaviour – particularly within the engineering-inspired paradigm of synthetic biology – our understanding of natural developmental processes, our ability to intervene in pathological states, and potentially our ability to create novel 'designer tissues' can all be expected to reap dividends.

The aim of this work is to explore the relationship between curvature and cell protrusions, and to address the currently open questions of what mechanisms underlie the response to curvature.

Chapter 2

BACKGROUND

2.1 Structural determinants of epithelial cell shape

Cell shape results from the active rearrangement of structural elements, including interactions with the environment, which serve to resist a passive rounding effect which is analogous to surface tension (Davies, 2013). One fruitful model of how cells form a diversity of shapes is 'tensegrity' (tensional integrity), which is a concept that was developed by the architect Buckminster Fuller in 1961, and subsequently introduced to cell biology by Ingber twenty years later. Viewing the cell as a tensegrity structure, focus is placed on elements under tension, such as the contractile actin-myosin cables and the dense mesh that forms the cell cortex, and how they are balanced by compressive elements such as microtubules, along with support from extracellular adhesion sites (Ingber et al., 2014).

Cells in suspension, such as is the case with freshly-trypsinized epithelial cells, superficially appear to have a round bubble-like shape. However, even in the absence of external support, suspended cells deviate from the simple sphere. Small actin-lined blebs have been reported to form in the case of detached epithelial cells, and argued to serve to package excess membrane when the actin cortex contracts, which gives suspended cells a degree of protective rigidity (Pietuch and Janshoff, 2013).

Similar observations and conclusions have been made with endothelial cells, and in both cases, blebbing cells were successfully replated; confirming that blebbing is not strictly a sign of apoptosis (Norman et al., 2010). Lymphocytes extend dramatic sheet-like protrusions which resemble lamellipodia, and also involve the branched actin nucleator Arp2/3 (Nicholson-Dykstra and Higgs, 2008). Relatively recently, a new type of protrusion in suspended cells has been identified which is independent

of actin: thin 'tubulin microtentacles' that are composed of microtubules stabilised with the intermediate filament vimentin, and which are distinct from cilia (Whipple et al., 2008).

Following initial contact with a substrate that permits adhesion, cells begin to flatten, bringing a progressively larger membrane area in close apposition with the underlying surface. This requires a release of tension in the cell cortex at the site of adhesion, which permits the change in shape, and releases excess membrane to form extended contact with the surface (Pietuch and Janshoff, 2013). The stiffness of the cell cortex has been shown to be determined by cortical actin dynamics, with actin depolymerisation and reduction in myosin motor activity both shown to cause a softening of the cortex (Fels et al., 2012; Schillers et al., 2010).

Integrins engage with various substrates and cluster to serve as platforms for structural and signalling components via specialised scaffold proteins, forming the mechanosensitive nascent adhesions. The 'adhesome' functions cooperatively to mechanically connect the contractile actin-myosin cytoskeleton to the substrate, and to direct the remodelling of the cytoskeleton to meet the demands of the environment (Huda et al., 2014). Nascent adhesions are competent to activate the small GTPase Rac within minutes after forming, which in turn promotes the formation of the dense, branched actin characteristic of lamellipodial protrusions (Xia et al., 2008).

Cell spreading is a bimodal process which has recently been characterised in terms of the contact angle formed by the substrate and the cell cortex. The initial phase is rapid, driven by local remodelling of the actin cytoskeleton, including Rac-driven lamellipodia extension. Integrin-based adhesions are small and distributed homogeneously across the cell-substrate interface. The second, slower phase begins as the cell-substrate angle approaches a 90° angle, at which point the contractile actin-myosin cortex is able to exert force increasingly efficiently on peripheral adhesions, with the component perpendicular to the substrate translating into traction. This phase is associated with the adaptive growth of focal adhesions at the periphery of the spreading cell (Fouchard et al., 2014).

When cells spread on rigid substrates, stress fibers are observed to form, consisting of bundles of antiparallel actin filaments crosslinked by nonmuscle myosin II motor proteins, which may connect adhesion sites under isometric tension. The small GTPase RhoA is inextricably linked to central stress fibers, acting in a feedback loop in response to tension on adhesions to activate myosin via its effector ROCK, thus generating further tension (Bhadriraju et al., 2007). Myosin activation at peripheral stress fibers, on the other hand, is associated with the calcium-activated kinase

MLCK (Katoh et al., 2011).

Peripheral stress fibres are believed to play a role in constraining cell motility, and it has been proposed that these structures serve to sequester monomeric actin, inhibiting the formation of actin-based protrusions locally. Inhibition of myosin or ablation of the myosin IIA isoform destabilises stress fibers and induces otherwise static cells to migrate (Lomakin et al., 2015). In a complementary model, MLCK levels in migrating keratocytes have been shown to correlate with the number and size of protrusions that form; higher levels of MLCK oppose the formation of a single large protrusion, instead promoting multiple smaller protrusions and poor migration persistence. This was also linked to myosin IIA activity, and inhibition of MLCK was found to slow the rate of myosin-mediated leading edge retraction (Lou et al., 2015).

On contact with neighbouring cells, the epithelial phenotype starts to establish itself. Homophilic adhesions are made via E-cadherin, and lamellipodia extend the zone of contact before being remodelled into the peripheral actin belt linking the newly-formed adherens junctions. Activation of myosin tightens the belt, reducing the footprint and increasing the height of cells in the monolayer, and generating tissue-level tension (Harris et al., 2014). Such clusters of mutually-adhesive cells can be seen as analogous to a single cell; subject to the same tendency to round up, which must be resisted by adhesions. This view is supported by the observation that multicellular collectives act as mechanically coherent entities to exert traction forces against their substrate in a similar pattern to single cells: with high, typically inward-directed forces at peripheral regions, balanced by lower forces distributed within the interior (Reffay et al., 2014).

In response to acute wounding, epithelial cells at the edge of the monolayer remodel peripheral actin at the wound-facing edge, accumulating active myosin in a contractile ring that forms a mechanically continuous structure through the cells bordering the wound. As this supracellular cable contracts, it moves from its original position close to the apical cell surface down to the level of the substrate (Tamada et al., 2007). The assembly and maintenance of this contractile ring has been shown to be dependent on the small GTPase RhoA and its effector kinase ROCK, while the subsequent contraction has been found to depend on the kinase MLCK (Russo et al., 2005).

Contraction of this ‘purse string’ cable has been reported to be the mechanism underlying the closure of small holes in wounded monolayers (Tamada et al., 2007), while in larger wounds it is considered to play a role in ensuring the wound mar-

gin advances coherently (Farooqui and Fenteany, 2005). This cable, also variously known as the 'pluricellular belt' has been suggested to be key to mechanical communication between leaders and followers during collective migration (Poujade et al., 2007), and it has been shown that disruption of this cable by various means results in the loss of ordered progression in migrating collectives (Danjo and Gipson, 1998; Reffay et al., 2014).

2.2 Experimental manipulation of cell shape

Traditional in vitro cell culture involves growing cells on two-dimensional (2D) surfaces of glass or plastic, with the surfaces treated to be conducive to cell adhesion. Adherent cells are free to spread and migrate, and tend to assume varied shapes, which makes it difficult to study relationships between cell shape and other variables (Marek et al., 1982).

Some early attempts to control cell shape were driven by the observation that normal cells in suspension fail to proliferate, in contrast to cells that are allowed to adhere to an appropriate substrate. Folkman and Moscona hypothesised that cell shape was the key variable controlling this switch: while cells in suspension are spherical, adherent cells are able to spread and flatten to varying degrees. They developed a novel method of controlling cell shape by tunable restriction of cell spreading, using different concentrations of nonadhesive poly(2-hydroxylethyl methacrylate) to coat the substrate. While they were able to show that inhibited spreading of isolated cells correlated with reduced DNA synthesis, to a similar degree to that seen in confluent cells with similar dimensions (the latter controlled by crowding, rather than reduced adhesion), they acknowledged that they could not confirm whether the results were directly due to varying cell shape, or rather due to the varying nature of the substrate (Folkman and Moscona, 1978). It was clear that there was a need for methods of accurately constraining cells while maintaining homogeneous substrate characteristics (Ireland et al., 1987).

One approach for precise patterning of cells on 2D substrates was pioneered by Carter in the 60s (Folch and Toner, 2000). Carter heated palladium wire under vacuum in close proximity to (adhesion-resistant) cellulose acetate film, using proximity and partial masking of the film to control the location and density of the deposited (adhesion-promoting) metal; the latter quality was later found to be due to selective adsorption of serum proteins such as vitronectin (Carter, 1965; Turner et al., 2004). This in turn determined where on the substrate cells could adhere, and to what extent. He used the technique to give the first experimental demonstration

of directed migration along a gradient of increasingly-adhesive substrate (coining the term 'haptotaxis' to describe the phenomenon), and subsequently developed it further, using micrometer-scale stencils to create micropatterns of defined shape with a sharp border separating the differentially-adhesive regions (Carter, 1965; Folch and Toner, 2000).

Cells cultured on such micropatterned substrates showed a strong preference for the more-adhesive regions, but were able to escape into the less-adhesive regions, particularly in response to crowding (confluence) (Harris, 1973). Other researchers improved on Carter's method by utilising alternative substrates that were superior to cellulose acetate in preventing cell adhesion, and so restricting cells exclusively to the metallic micropatterns (O'Neill et al., 1986; Westermark, 1978). Westermark observed that groups of cells confined strictly to micropatterns showed a density-dependent inhibition of proliferation that mimicked the effect of true confluence, despite having cell-free edges that were superficially similar to a 'wounded' monolayer (Westermark, 1978).

Many modern methods for constraining cells in defined geometries are based on photolithographic techniques, originally developed as a fundamental technology for microelectronics fabrication. A common approach involves careful layering of a photosensitive polymer on to a base substrate, followed by exposure to ultraviolet light through a mask which determines which areas are exposed (the patterning step). The polymer's solubility is modified depending on whether or not it is irradiated, allowing selective removal of the polymer to expose the substrate, and thus the pattern. Cells may be seeded directly on the photolithographically-patterned substrate, or else it may be used as a mould to shape an elastomeric replica. The latter can then be used as a 'stencil' to physically restrict cells, or else as a 'stamp' or 'mould' to create adhesive patterns on a blank substrate (Folch and Toner, 2000; Huda et al., 2014). Although requiring some technical sophistication and specialised resources, these approaches to patterning cells have opened up new avenues for probing the interplay between cellular shape and other variables.

O'Neill and colleagues were able to reproduce Folkman and Moscona's findings with isolated cells under the more controlled conditions permitted by photolithographic micropatterning, adding more support for the importance of cell shape in determining important aspects of cell behaviour (Ireland et al., 1987; O'Neill et al., 1986). They found that the number of adherent cells carrying out DNA synthesis increased with the size of the micropattern, with levels that ranged between that of cells in suspension and unconstrained cells. For the two larger cell lines studied, this relationship between micropattern area and proliferation appeared to support

a role for the area of the cell surface exposed to the medium, as the results showed a dip in the number of labelled cells corresponding to a predicted minimum exposed area (where adherent cells could be expected to be hemispherical, with an exposed area less than that of fully suspended cells). However, this relationship did not hold true for a third, smaller cell line included in the study (O'Neill et al., 1986).

Chen and colleagues were able to exploit the high precision afforded by photolithographic approaches to pattern endothelial cells across multiple regular adhesive spots with diameters as small as 5 μm, allowing them to vary the shape of adherent cells, while keeping the total adhesive contact area constant. They showed that proliferation increased with the total area that the cell was allowed to extend over (Chen et al., 1997). Together, these studies demonstrated that neither exposed surface area, nor total adhesion contact area, could be identified as being fundamentally responsible for the differences in cell behaviour when constrained on micropatterns of different sizes.

While the majority of micropatterning work discussed so far was done with fibroblasts, the importance of cell shape in modulating phenotype is generalisable to epithelial and other cell types. Micropatterned keratinocytes constrained by small micropatterns (thus forced to assume a rounded shape), showed low levels of proliferation and high levels of terminal differentiation (using involucrin expression as a marker), whereas increasing micropattern size showed the opposite effects (Watt et al., 1988). Similar results were shown with isolated primary hepatocytes, which lost albumin expression and increased proliferation rates with increased micropattern size (Singhvi et al., 1994).

2.3 Effects of geometry on motility in single cells

Along with early work focused on the effects of overall cell shape and spreading area on proliferation and differentiation, other studies were conducted into the effects of micropattern perimeter geometry on the ultrastructure and behaviour of adherent cells. Marek, Ireland, and colleagues carried out the first detailed studies into the organisation of the cytoskeleton and adhesions of micropatterned cells, using fibroblasts cultured on micropatterns with a range of shapes and sizes.

Isolated cells confined to relatively large square micropatterns were found to develop pronounced stress fibres that ran diagonally between corners. Stress fibres terminated at adhesions strictly within the bounds of the micropattern, although limited overlap of the surrounding nonadhesive substrate by a randomly orientated

'lacework' at these points was noted (Marek et al., 1982).

When cells were constrained to much smaller micropatterns (ranging from 400 μm^2 to 5000 μm^2, compared to upwards of 8000 μm^2 in the previous work), interesting phenotypes emerged in response to island size and shape. Larger, more stable adhesions were found to form at the perimeter of larger micropatterns, accompanied by island-spanning stress fibres. In contrast, smaller islands formed smaller, less stable adhesions, and lacked central stress fibres (Ireland et al., 1987).

Focal adhesion distribution was found to depend on the perimeter geometry: forming in a ring at the perimeter of circular micropatterns, and accumulating at the corners in the case of triangular micropatterns (Ireland et al., 1987; O'Neill et al., 1990). O'Neill and colleagues made the observation that cells grown on linear islands had an equivalent total focal adhesion area as those on larger islands with a smaller aspect ratio, and were stimulated to proliferate to the same degree. This led them to suggest that the force applied against the adhesions, as determined by the degree to which the cell was stretched, could be responsible for the effect on cellular phenotype (O'Neill et al., 1990).

The groups headed by Ingber and Whitesides were the first to explicitly note and explore the relationship between micropattern perimeter geometry and the direction (control of the spatial organisation) of cellular protrusions. Work in 2002 using flexible substrates confirmed the earlier speculation by O'Neill et al. that cellular traction forces were concentrated at corners at the periphery of micropatterns, as reflected by the increased size of the clusters of focal adhesions at those points. Parker et al. stimulated fibroblasts and endothelial cells to increase the rate of lamellipodia extension, and observed that the protrusions were preferentially formed at the corners of square micropatterns (Parker et al., 2002).

Parker and colleagues applied several drug treatments to PDGF-stimulated fibroblasts to attempt to establish a link between the positioning of protrusions and the orientation of cellular traction forces defined by micropattern geometry. The drug 2,3-butanedione monoxime (BDM), used as an inhibitor of myosin, caused the abrupt arrest of protrusions. Two other chemical manipulations aimed at reducing cellular contractility, the Rho-kinase (ROCK) inhibitor Y–27632, and the intracellular calcium chelator BAPTA-AM, were also reported to abolish protrusions (Parker et al., 2002). Further work by this group using a wide range of simple polygonal shapes showed that sharper angles had a higher likelihood of protrusion formation, and tended to form narrower protrusions (Brock et al., 2003).

Other groups confirmed this relationship between the geometry of micropatterned

substrates, and the orientation of confined cells. James et al. used a fibroblast-like melanoma line with a tendency to form multiple lamellipodia and migrate randomly, confining individual cells to micropatterns that combined local and global geometric cues: local curvature, and aspect ratio. The cells tended to produce lamellipodia at corners and convex curves, and along the short edges of shapes with a high aspect ratio. In contrast, stress fibres tended to form along long edges and at concave curves, bridging across the nonadhesive regions in the latter case. The distinction between lamellipodia- and stress fibre-favouring regions was relatively weak for polygonal shapes, and became increasingly apparent when convex and concave curves were combined to form 'flower' and 'starfish' shapes (James et al., 2008). These findings were foreshadowed by earlier work by Théry et al., who previously demonstrated the tendency of stress fibres to span nonadhesive regions, and of the Golgi apparatus and microtubule cytoskeleton to polarise towards convex edges (Théry et al., 2006).

The polarisation observed in single micropatterned cells was found to translate to directed migration when the constraints were removed. An innovative micropatterning approach developed by the Whitesides group allowed them to release cells from the micropatterns, using a short pulse of electricity to change the adhesiveness of the surrounding substrate. They demonstrated that fibroblasts and endothelial cells polarise on asymmetric 'teardrop' shapes: positioning the Golgi apparatus towards and extending lamellipodia preferentially from the blunt end. When released, the cells migrated preferentially from the blunt end (Jiang et al., 2005). This outcome was supported by work done using similar teardrop-shaped micropatterns arranged in close proximity, so that the cells were able to migrate by extending across the adhesive region to reach adjacent islands (Kumar et al., 2015). This confirmed that the direction the fibroblasts migrated was due to the geometry of the micropattern, and was not influenced by the brief voltage pulse used in the previous experiment.

Using this 'island-hopping' system, sets of four teardrops were placed end to end with their long axes at a 90° angle to each other. Two different layouts were used: with either the sharp or blunt end in direct line with the next island in the chain, separated by a 3 μm nonadhesive gap. Fibroblasts preferentially migrated from the blunt end when presented with another island in line with the long axis of the teardrop. When the next island in the chain was placed side-on to the blunt end, the cells migrated from the sharp end in preference to deviating from the direction imposed by the long axis, although with a delay to repolarise (Kumar et al., 2015). Other work with constrained fibroblasts has shown that the initial

orientation of protrusions is reliably correlated with the direction of migration once released from confinement, while the initial orientation of the Golgi apparatus is a poor predictor (Chen et al., 2013).

In contrast to the findings with fibroblasts, epithelial cells were found to favour the opposite direction when the blunt ends were to the side of the sharp ends: migrating from the pointed end of the teardrop even though they were required to make a 90° turn to do so. In another contrast from the case with fibroblasts, when the next island was in line with the sharp end, epithelial cells showed no directional preference: they were equally likely to migrate from the sharp end parallel to the axis, as they were to take a 90° turn to migrate from the blunt end. Interestingly, in the latter case, reducing the levels of the small GTPase Rac using siRNA suppressed protrusions perpendicular to the teardrop long axis, and resulted in a fibroblast-like direction of migration: preferentially from the sharp end along the long axis (Kushiro et al., 2010). Collectively, these results suggest that fibroblasts are directed primarily by the global cue of aspect ratio, with local cues such as adhesion availability having less power. Epithelial cells on the other hand, appear to be more sensitive to local cues.

2.4 Effects of geometry on motility in multicellular collectives

While the previous work has focused on the behaviour of isolated cells, fibroblasts and epithelial cells can be expected to be far more dissimilar when the behaviour of collectives is considered. Fibroblasts are generally not included in discussions of the phenomenon of collective migration; unlike epithelial cells, fibroblasts spread and migrate as individual cells when free to disperse on homogeneous substrates. However, recent work on fibroblasts has shown a tendency to take on an elongated shape along a single axis and migrate rapidly and collectively when released along a micropatterned strip, with narrower strips and higher cell densities reinforcing the collective behaviour (Leong et al., 2013). While this study could be dismissed as showing the expected outcome of reduced freedom of movement, another study with fibroblasts has suggested that they are collectively responsive to their initial geometry on release from constraint.

Small groups of fibroblasts were micropatterned on simple geometric shapes (circles, ovals, squares and rectangles), and were released using adsorption of chitosan to the initially-nonadhesive surrounding substrate. The fibroblasts responded by migrating with a surprising degree of collectivity, and a pronounced tendency to migrate along the long axis of oval and rectangular shapes, and from one or two

adjacent corners of the square shapes. Treatment with the ROCK inhibitor Y–27632 resulted in a loss of collectivity and a loss of response to the geometrical cues: cells migrated away from the micropatterns in random directions. Conversely, constitutively active RhoA GTPase enhanced the response to aspect ratio and local curvature (Kumar et al., 2011).

Chitosan is a polysaccharide produced by fungi and arthropods and is commonly used to promote wound healing. Fibroblast adhesion to chitosan film is stronger than to conventional tissue culture plastic, and it is known to adsorb fibronectin (Hamilton et al., 2006). This suggests that the collective behaviour exhibited by the fibroblasts is not due to a relative increase in cell-cell adhesion strength, nor necessarily to a lack of integrin engagement. It appears clear that the cells were responsive to the initial confining geometry, and that contractility played an important role. However, the novel culture system makes it difficult to make comparisons with the far larger body of work conducted using epithelial cells.

A feature apparently unique to epithelial cells is the peripheral super-cellular actin-myosin cable that forms at the edge of wounded monolayers, and is known as the 'purse string' for the role it plays in closing small wounds (Danjo and Gipson, 1998). Epithelial cells growing around drops of solidified agarose form the relatively thick actin cable in a continuous ring around the obstruction, and gently removing the agarose with enzymatic digestion is sufficient to induce the monolayer to close over the gap. Monolayer closure, or 'wound healing', occurs through a combination of two collective processes: leader cell-directed crawling, characterised by the appearance of lamellipodia, and purse string closure, which is dependent on non-muscle myosin II to shorten the super-cellular cable (Klarlund, 2012).

Although the work with fibroblast collectives, which do not form a super-cellular purse string cable, suggests that the structure isn't necessary for collective responses to geometry, it is clear that it does play a significant role in epithelial cells in some circumstances. The purse string links adherens junctions in cells at the wound periphery, and its disruption with an E-cadherin function-blocking antibody has been shown to result in the formation of lamellipodia and a loss of collectively-coordinated movement (Danjo and Gipson, 1998). Perhaps more convincingly, targeted laser-ablation of the cable commonly causes the initiation of a new leader cell at the site of the cut, which has been put forward as evidence that the purse string serves to restrain and direct migration in epithelial collectives (Reffay et al., 2014).

Releasing epithelial cells to fill crescent-shaped gaps, which permit observation of

the relationship between motility at the linked concave and convex curvatures, has shown that there is a force balance between the two forms of wound closure: crawling and purse string closure. Tension transmitted from the advancing concave edge, through the cable at the wound edge, serves to restrain the forward progress of the crawling convex edge; severing the cable by laser ablation frees the collective at the convex edge to advance into the gap. This balance can be shifted, for example, by increasing the concentration of fibronectin adsorbed on the substrate (thus favouring the crawling convex edge) (Ravasio et al., 2015).

Other work with epithelial cells released from circular- and doughnut-shaped micropatterns confirms that convex curves favour lamellipodia and leader cell initiation, while concave curves favour purse string closure. Restricting comparisons to micropatterns with a mean cell area of 440-900 μm^2, Rolli et al. showed that the frequency of leader cell initiation from the outer edge (normalised by perimeter length) was inversely proportional to the radius of the circle; directly proportional to convex curvature (Rolli et al., 2012).

Rolli and colleagues also found that sensitivity to curvature was affected by the length of time the cells were cultured before being released: cells released from doughnut-shaped micropatterns 9 hours after seeding initiated leader cells at high frequencies from both the external (convex) and internal (concave) edges, while cells cultured for 25 hours initiated leader cells from the convex edge at a lower rate, and rarely from the concave edge. The authors showed a correlation with E-cadherin localisation (diffuse in the case of collectives incubated for shorter times), and argued that the coherent collective response to curvature required mature cell-cell adhesions, which were underdeveloped in the cells released 9 hours after seeding (Rolli et al., 2012).

The use of micropatterns with slightly more complex geometries has demonstrated the collective sensitivity of epithelial cells to local cues. Rausch et al. released cells of the epithelial MDCK II line from large circular micropatterns (350 μm diameter, containing approximately 350 cells), some of which were modified with relatively small features at the periphery: hemispheres of 35 μm radius, or triangles of base 60 μm and height 67 μm. While the average rate of leader cell initiation for each micropattern was approximately equivalent, the hemispherical features had a 2-fold increase in the probability of leader cell initiation over other regions of the micropattern periphery (the 'normal curve'), and the triangular features showed an additional 2-fold increase (Rausch et al., 2013).

Rausch and colleagues reported that, prior to release, cellular traction forces were

concentrated at the features, and inhibition of contractility, using the myosin inhibitor Blebbistatin or the ROCK inhibitor Y–27632, had the effect of reducing preferential leader initiation. The authors also observed that the peripheral actin cable appeared disrupted at the tips of the triangular features, and that while focal adhesions were oriented centripetally at the features, they were oriented tangential to the periphery elsewhere (Rausch et al., 2013).

The ability of single cells and multicellular collectives to sense and respond to physical cues has been the subject of recent reviews that have highlighted multiple potential contributing mechanisms and feedback loops, as well as the current lack of a complete model to explain the spatial and temporal control of protrusions and directional migration (Ladoux et al., 2016; Verkhovsky, 2015).

2.5 Proposed mechanisms for curve-sensing and response

Extension of the approach of micropatterning groups of cells to three dimensions (3D) confirmed that the relationship between initial shape and subsequent collective migration is not restricted to cells cultured on two-dimensional (2D) substrates, and led to one hypothesis of the underlying mechanism for the relationship. Nelson and colleagues used a microfabricated mould to create wells of defined geometry in collagen gel, allowing them to generate precisely-defined double-layered tubules consisting of mammary myoepithelial and luminal epithelial cells. When stimulated with appropriate cytokines, these tubules branched into the surrounding collagen, with cells at the tips of the micropatterned tubules taking on the invasive leader role. More complex micropatterns showed that branching was inhibited at concave regions, and promoted at convex regions (Nelson et al., 2006).

It was hypothesized that the position-dependence of the branch initiation was due to the relative concentration of an autocrine inhibitor secreted by the cells. While secretion rate may be constant, the greater space available at convex curves would be expected to result in a lower relative concentration, with converse being true at concave curves. Mathematical simulation supported the relationship of the latter with tubule geometry: tubule tips were predicted to experience the lowest concentrations of any diffusing autocrine signal (Nelson et al., 2006).

Further evidence for this ‘autocrine inhibitor accumulation’ hypothesis was the loss of branch position dependence when signaling via the morphogen TGFβ1 was blocked. However, while overexpression of constitutively-active TGFβ1 blocked all branching, overexpression of wild-type TGFβ1, which is secreted in an inactive

form, had no effect, implying additional mechanisms were at work at the level of post-translational modification of TGFβ1 (Nelson et al., 2006).

Nelson and colleagues made an observation that did not seem to support their hypothesis: they noted that increasing the length of the tubules increased the length of the branches that formed from their tips (Nelson et al., 2006). While they did not address this point further, it seems intuitive that a longer tubule, all other things being equal (with all cells secreting at equal rates), would have a gradient at the ends that is effectively the same as that of a shorter tubule. Alternatively, the increased number of cells secreting the inhibitory cytokine might be expected to result in a slightly higher concentration at the ends. As both short and long tubules initiated branches exclusively at the ends of the tubules, suggesting that no 'pruning' of branches was responsible for the difference, the latter scenario if anything should result in fewer or shorter branches.

While the difference in branch length between short and long tubules doesn't appear to be explicable when only considering the relative concentration of autocrine inhibitor, the difference in aspect ratio between the two conditions is suggestive of an important alternative or additional role for mechanotransduction. Single cells constrained to rectangular micropatterns of equal area but variable aspect ratio show a linear relationship between traction stress and the distance from the centre, with a strong correlation with focal adhesion size (Rape et al., 2011). Focal adhesions, as a mechanical link between the cell and its physical environment, are fundamentally associated with cellular mechanotransduction (Ladoux et al., 2016). Given the mechanical continuity of groups of epithelial cells, it is possible to extrapolate to cell clusters in 2D and 3D, and ascribe a role for mechanotransduction in sensing and responding to changes in aspect ratio.

Mechanotransduction via integrins and other components of focal adhesions is a strong candidate for an underlying mechanism for sensing curvature. Micropatterned cells have been shown to accumulate high levels of paxillin in large focal adhesions at corners, the same points from which protrusions preferentially form, while fibroblasts lacking paxillin extend lamellipodia without directional preference (Sero et al., 2012). Paxillin is a multifunctional scaffold protein that is phosphorylated in response to applied force (Pasapera et al., 2010), and has been shown to play roles involving Rac activation and microtubule stabilisation, both of which are important in directional cell migration (Deakin and Turner, 2014; Sero et al., 2012).

Paxillin is clearly necessary for the positioning of lamellipodia, and regulation of

paxillin localisation and scaffold function appears to be fundamental to the differential response to local geometry. It may be the case that increased force applied passively to integrins, as a function of increasing aspect ratio and distance from the centre of mass, is sufficient to explain the increase in paxillin occupancy at focal adhesions at corners. However, differential calcium channel activation may play a role, as calcium pulses in migrating cells have been shown to cause transient increases in paxillin at focal adhesions through increases in myosin activity (Tsai and Meyer, 2012), while inhibition of myosin has been shown to result in a homogeneous distribution of peripheral paxillin-containing focal adhesions (Pasapera et al., 2010).

Mechanosensitive ion channel activation has been the subject of much attention in recent years, and has been suggested to play a key role in cellular responses to force and substrate stiffness (Plotnikov and Waterman, 2013), and by extension could be expected to play a role in sensing aspect ratio and other geometrical cues. A number of channels have been found to function in contexts that are suggestive of a potential role in curvature sensing and response. Calcium 'flickers' in the vicinity of focal adhesions in the lamella region of migrating cells have been traced to brief activation of the TRPM7 calcium channel in response to mechanical stress, and are considered to play an important role in directing cell migration (Wei et al., 2012). Another ion channel, TRPV4, has been shown to associate with focal adhesions, and to mediate rapid calcium influx in response to force applied to integrins (Matthews et al., 2010).

Calcium influx has been shown to occur independently of integrin-mediated adhesions, in response to mechanical stimulation (prodding) of fibroblasts (Shao et al., 2015). This suggests that channel activation in response to stretch may occur at sites other than the convex regions where focal adhesion traction stress is dominant. The recent discovery that the TRPV2 calcium channel translocates to the plasma membrane at regions experiencing stress, and is involved in the remodeling of the cytoskeleton (Nagasawa and Kojima, 2015), makes it tempting to speculate on a potential alternative role for calcium influx in the response to curvature. It has been shown that actin cables at the periphery of cells bridging nonadhesive regions of micropatterns are under increased tension (Suffoletto et al., 2015). Some of the tension at these concave curves could be expected to be carried by the cortex, which could result in channel translocation and calcium influx in response to strain. This could result in increased myosin activation via MLCK, which could in turn increase the tension transmitted to the anchoring focal adhesions at the flanking convex sites.

While it seems that mechanical cues play a primary role in directing cell motility in response to geometry, it is likely that motile cell collectives will ultimately integrate many other cues to determine the shape of the resultant multicellular structure. These may include diffusing cytokine gradients as hypothesised by Nelson et al. (Nelson et al., 2006). There is support for the significance of chemical signals in the otherwise mechanical context: the recent demonstration that single cells will reverse their preferred direction of migration after release from a two-dimensional micropattern, when exposed to conflicting signals from an opposing cytokine gradient (Zheng et al., 2014).

Chapter 3

DEVELOPMENT OF EXPERIMENTAL PLATFORM

3.1 Aim and approach

The aim of this work was to explore alternative hypotheses as to the mechanism underlying the observed relationship between the curvature of the periphery of two-dimensional epithelial sheets, and presence of protrusions such as lamellipodia.

An epithelial cell line was cultured on two-dimensional (2D) micropatterns with regions of different curvature around the perimeter, allowing the relationship between the presence of protrusions and different curvatures to be assessed, and providing a platform for testing various treatments for their effect on the relationship.

This approach is a continuation of earlier work done by students in the Davies lab, and the initial stages involved repeating and confirming their earlier findings using similar methods (Davies, 2013; Stimac, 2013).

3.2 Madin-Darby Canine Kidney (MDCK) cells

Cell lines originating from a culture established by Madin and Darby in 1958, using cells isolated from a normal dog kidney, have been used as model epithelial lines for decades. While multiple lines with distinct characteristics have been derived from the heterogenous parental culture over time, the strain designated type II Madin-Darby Canine Kidney (MDCK II) has been widely adopted by researchers, and is

recommended for its stable epithelial phenotype (Dukes et al., 2011).

The MDCK II cells used in this study were obtained from the European Collection of Cell Cultures (ECACC; cat. 00062107; lot 10D039) at passage 28.

3.3 Genetic modification of MDCK II cells

MDCK II were modified to constitutively express the live actin-marker 'Lifeact-GFP' (Riedl et al., 2008). The expression vector pEGFP-N1-Lifeact was a kind gift from Dr Tim Czopka at the University of Edinburgh.

MDCK cells are recognised as being relatively difficult to transfect by standard (non-viral) methods (Schuck et al., 2004). Optimisation of the following transfection protocol using the lipid-based transfection reagent Metafectene PRO (Biontex; T040) gave up to 20% transfection efficiency with minimal cell death. The protocol involved forward transfection: the DNA and transfection reagent complex (prepared at a ratio of 2 µL Metafectene PRO to 1 µg DNA) added to subconfluent adherent cells, with a final concentration of 1.4 µL of transfection reagent per mL. As recommended by the manufacturer, the transfection reagent and DNA were first diluted separately in Opti-MEM (Invitrogen; 31985), mixed carefully and incubated at room temperature for 20 minutes to form complexes, before being added to cells growing in a reduced volume of antibiotic-free complete media.

Cells were passaged 24 hours after transfection and treated with 500 µg G–418 (PAA; P25–011) for 10 days to select for stable transformants, and subsequently maintained in the absence of G–418. Stable Lifeact-MDCK clones that maintained strong Lifeact-GFP expression in the absence of selective pressure were isolated using fluorescence-activated cell sorting (FACS) by Dr Claire Cryer at the MRC Centre for Regenerative Medicine. The use of FACS sorting without antibiotic selection has been recommended as giving superior results in the generation of stable clones with homogeneous and high levels of transgene expression (Kaufman et al., 2008).

3.4 Variable-curvature micropatterns

Micropatterned substrates were a kind gift from Dr Huabing Yin and Dr Xiaofei Yuan at the University of Glasgow, and were prepared using a photolithographic method as previously described (Yuan et al., 2015). Briefly, glass slides were first functionalized with (3-aminopropyl)trimethoxylsilane (APTMS; Sigma-Aldrich) to form an

amino-terminated self-assembled monolayer (SAM) - the adhesion-permissive surface. A positive photoresist (S1805 G2, Rohm and Hass Co.) was spin coated onto the APTMS, and a mask was used to protect micropatterned regions from brief exposure to UV light, which increased the susceptibility of the surrounding unprotected photoresist to a subsequent wash with the developer solution (Huda et al., 2014). Once the surrounding photoresist had been removed, the underlying APTMS was in turn removed with oxygen plasma etching, and replaced with 2-(methoxy(polyethyleneoxy)$_{6\text{-}9}$propyl)trichlorosilane (PEG-silane; Gelest) - the adhesion-resistant surface. Finally, the remaining photoresist was removed by sonication in DMSO to reveal the micropatterned APTMS. See Fig. 3.1 for a diagram of the process.

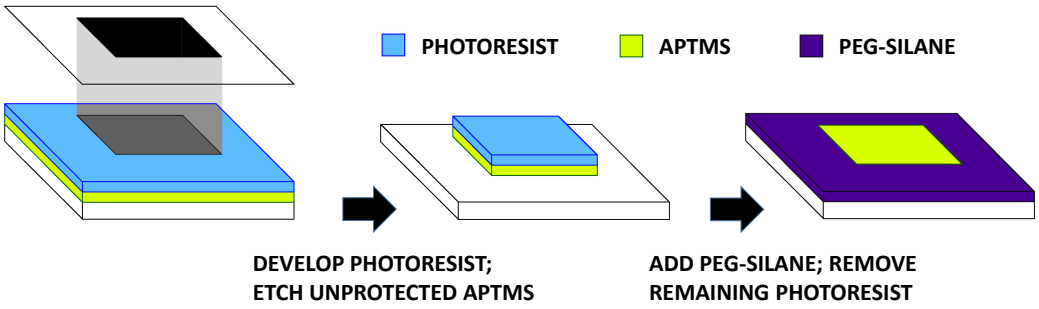

Figure 3.1: **Preparation of micropatterns by Huabing Yin and colleagues.** APTMS-treated glass slides were coated in a positive photoresist, and a mask was used to selectively protect regions from UV exposure. UV-exposed photoresist was removed along with the underlying APTMS, and the exposed glass was treated with PEG-silane before the remaining photoresist was removed to reveal the cell-adhesive micropattern. See text for more information.

Micropatterns were manufactured in an asymmetrical shape reminiscent of a simple branching structure (Fig. 3.2A), with the aim of allowing different curvatures to be compared within individual micropatterns. This is in contrast to previous works which have tended to use simpler geometrical shapes.

Micropatterns were protected from light and stored in a vacuum desiccator at 4 °C to minimise degradation of the patterns prior to use. Micropatterns were prepared in batches on single glass slides, which were then broken into pieces of approximately 1cm^2. All experiments utilised the same micropattern batch for controls and treatments, to ensure that any batch-to-batch variability in micropattern production or storage did not affect results. Micropatterns were sterilised by UV-irradiation for 15 minutes immediately prior to use, and all subsequent work was conducted in a Class II tissue culture hood using aseptic techniques and sterile reagents.

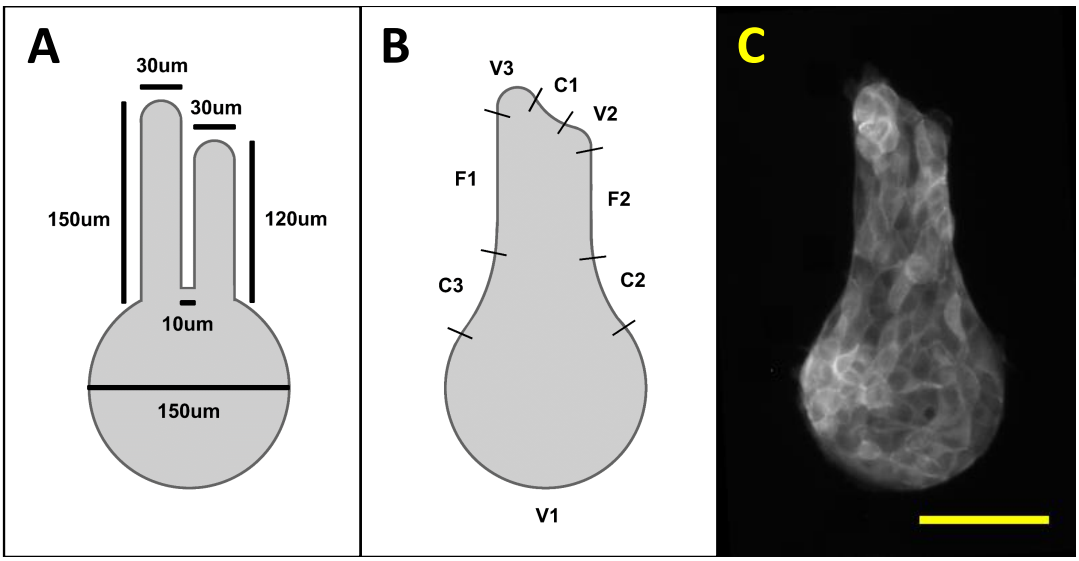

Figure 3.2: **Micropattern shape.** Diagram of micropattern shape, showing dimensions of underlying pattern (A) and segments defined once cells have adhered (B). Panel (C) shows a representative photomicrograph of Lifeact-MDCK cells growing on a micropattern, captured with a 10x objective. Individual cells can be identified by the stronger actin signal bordering each. Note that the adherent cells bridge over regions outside the adhesive pattern to form the concave segments. A 100 µm scale bar is shown in yellow at bottom right.

3.5 Seeding and culturing

MDCK II were cultured in Minimum Essential Medium Eagle (MEM; Sigma, M5650) supplemented with 2mM L-glutamine (Gibco, 25030–024), 100U penicillin /streptomycin (Gibco, 15140), and 5% fetal calf serum (Invitrogen, 10108165). All supplements were kept frozen until use, and complete media was stored at 4 °C and used within 30 days of preparation. Cells were expanded prior to experiments in standard tissue culture flasks in a humidified cell culture incubator at 37 °C and 5% CO_2.

To passage cells, and to prepare cell suspensions for experiments, cultured cells were washed briefly with warm phosphate-buffered saline (PBS), and incubated with Trypsin-EDTA (Sigma, T4174) until the cells started to lift and could be dislodged with firm raps to the flask. Trypsin digestion was then quenched with FCS-supplemented media, and the cells pelleted and resuspended in complete media. Cells were typically passaged at a 1:5 ratio every three days, between experiments.

MDCK II between passages 35–41 were passaged one day prior to use, to ensure they were subconfluent at the start of the experiment. To seed micropatterns, cells were trypsinized as described, then cells in suspension were counted using a hemo-

cytometer, and the concentration was adjusted to $2.25x10^5$ cells per ml (previously determined to give satisfactory cell coverage of micropatterns after 24 hours). Each approximately $1cm^2$ glass fragment containing micropatterns was placed in a well of a 6-well tissue culture plate, and the well was filled with 4ml of the prepared cell suspension. After incubation at 37 °C for two hours, micropatterns were washed twice with warm PBS, then refreshed with warm complete media. Micropatterned cells were cultured for 24 hours after seeding before being subjected to any treatments.

3.6 Live imaging chamber

Live imaging was conducted using an improvised chamber (as constructed by Dr Elise Cachat, with minor modifications) placed on an inverted microscope. A heating plate attached to the underside of a T175 flask (with a filter cap) kept the cells at 37 °C, and humidified air containing 5% CO_2 was warmed and continuously pumped into the chamber to maintain the pH. Cell culture plates containing cells for viewing were passed into the chamber through an opening in the side, which was then sealed with masking tape. As micropatterns were on pieces of microscope slide glass, which in turn sat inside cell culture plates, there were three layers between the optics and the cells (one of glass, two of tissue culture plastic). To improve the image quality, a section of the underside of the T175 flask was removed, and cell culture plates were fixed to the base of the flask with a ring of putty to provide a seal and minimise movement.

3.7 Quasi-Vivo flow culture

Flow experiments were conducted using a commercial modular perfusion bioreactor (Quasi-Vivo QV500 chamber system, Kirkstall) and a peristaltic pump (EP–1, Bio-Rad). Two flow chambers were set up in series, as per the QV500 user manual (Issue Number 3.0), and the volume flow rate through the entire system (perfusing both chambers) was measured by repeatedly weighing the quantity of distilled water that passed through ($3\,mL\,min^{-1}$, limited by the pump). Before and after each use, the system was sterilised with 70% ethanol, followed by a rinse with sterile distilled water.

Prior to placing micropatterned cells in the flow chambers, the system was washed with PBS, and then primed with warm complete media. Micropatterns were placed facing upwards, with 'fingers' pointing towards the inlet, and long axis aligned with

the direction of flow (i.e. media flowed from segment C1 to segment V1; see Fig. 3.2B and 3.3B). As the total volume of media in the flow system was 25ml, control micropatterns were transferred to 10cm dishes with 25ml media in order to avoid variable conditions due to total concentrations of released cytokines or metabolic byproducts, including changes in pH. Micropatterned cells were subjected to continuous flow of media for 1.5 hours. Control and flow-treated cells were kept in the same incubator for the duration of the treatment.

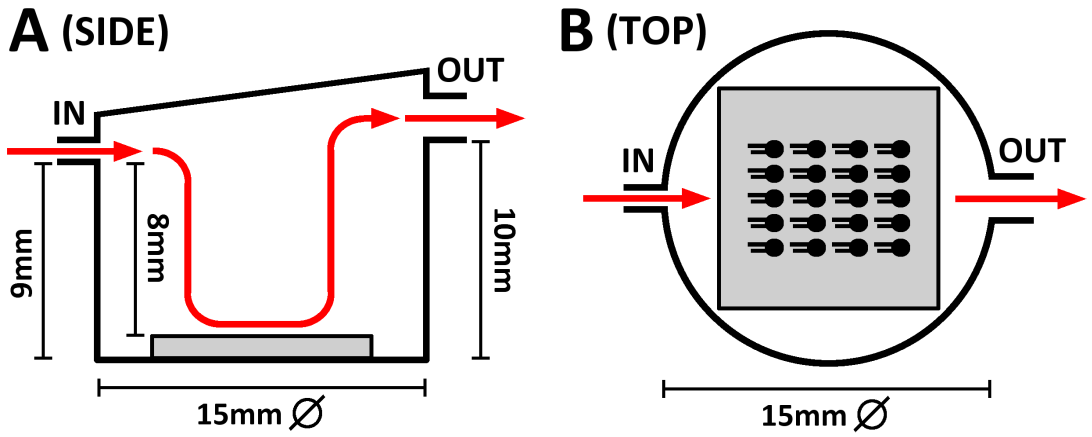

Figure 3.3: **Quasi-Vivo flow chamber setup.** (A) Side view of the QV500 chamber showing the direction of flow (red arrows) across the 1mm-thick glass fragment (grey) containing the micropatterns. (B) The top view shows the orientation of the micropatterns (not to scale) within the chamber. Chamber dimensions taken from Mazzei et al., 2010.

3.8 Drug treatments of cells on micropatterns

Intracellular calcium chelator BAPTA-AM and calcium ionophore Ionomycin were kind gifts from Prof Mike Cousin, prepared as 30 mM and 5 mM stocks in DMSO, and used at 10 µM and 2.5 µM, respectively. Actin polymerization was inhibited using 0.1 µg mL^{-1} Cytochalasin D (0.2 µM), prepared as a 1 µg mL^{-1} stock in DMSO, Myosin II activity was targeted using 25 µM (-)-Blebbistatin (Sigma; B0560; the active enantiomer, referred to as 'Blebbistatin' in this text), prepared as a 50 mM stock in DMSO. The stock was stored in the dark, as Blebbistatin is known to be inactivated by exposure to blue light (Sakamoto et al., 2005). Activity of the Rho Kinase ROCK was inhibited using 5 µM Glycyl-H 1152 dihydrochloride (Tocris; 2485; referred to as 'Glycyl-H–1152' in this text), a more selective glycyl analogue of H 1152 dihydrochloride, which itself was developed as a more potent and selective inhibitor of ROCK than the commonly-used Y–27632 (Tamura et al., 2005). All stocks were stored in aliquots at −20 °C for long durations, or at 4 °C for shorter durations, and

working solutions were made fresh for each experiment. Cells seeded on micropatterns prepared in the same batch were treated with either a drug or an appropriate vehicle control in complete media, and incubated at 37 °C for 1–2 hours before fixation and staining.

3.9 Fixing and staining

Seeded micropatterns were swiftly fixed following treatments in preparation for staining and analysis. Cells were washed briefly with FCS-free media (pre-warmed, to avoid temperature shocks; PBS was not used, to avoid loss of calcium-dependent adhesions), and then left to fix in 4% paraformaldehyde (PFA) at room temperature for a minimum of 30 minutes before being transferred to 4 °C for storage prior to staining. PFA was chosen as the fixative as it is compatible with phalloidin-staining (unlike methanol-based fixation). Fixed Lifeact-MDCK cells were imaged without further processing, whereas wild-type MDCK II were stained prior to imaging.

Fixed micropatterns were washed with PBS, then permeabilised in 0.1% Triton X–100/PBS for 20 minutes before washing twice more with PBS. The actin cytoskeleton was stained by a 1 hour incubation in 0.1 μg FITC-phalloidin (reconstituted to 100 μg in methanol, and diluted 1:1000 just prior to use with PBS; Sigma, P5282). Nuclei were stained by 5 minute incubation in 300nM DAPI/PBS, followed by two PBS washes. Finally, micropatterns were inverted onto a drop of VECTASHIELD mounting medium on a microscope slide for imaging. All reagents were warmed to room temperature prior to use. Stained micropatterns were protected from light and stored at 4 °C until imaged.

For immunofluorescence staining of Myosin Light Chain (MLC) phosphorylated on serine 19, the above protocol was modified slightly reduce the fixation time to 15 minutes, followed by a quenching step to reduce PFA background fluorescence (50mM NH_4Cl for 15 minutes). A blocking step to prevent non-specific staining was added after FITC-phalloidin staining (2% BSA/PBS for 1 hour), followed by 1 hour incubation with first a 1:200 dilution of the primary antibody (Phospho-Myosin Light Chain 2 [Ser19] Mouse mAb #3675, Cell Signaling Technology), and after several washes by a 1 hour incubation with a 1:400 dilution of the secondary antibody (TRITC anti-mouse). Images were captured immediately after staining, to avoid a loss of fluorescence signal.

3.10 Image capture and processing

Images of live and fixed Lifeact-MDCK were captured using a Zeiss AxioImager D1 (inverted) fluorescence microscope equipped with an AxioCam MRm camera and a GFP filter (excitation 470/40; emission 525/50). Images of fixed micropatterns with FITC-Phalloidin-labeled actin cytoskeletons and DAPI-labeled nuclei were captured using a Zeiss AxioImager A1 (upright) fluorescence microscope equipped with an AxioCam MRm camera and filters with the appropriate excitation and emission specifications (Fig. 3.4). The 10x objective allowed the maximum number of patterns to be captured in each image, while still giving sufficient resolution for counting protrusions. Exposures were set to maximise the Lifeact-GFP and FITC-Phalloidin signals in protrusions with minimal background. For rapid capturing of large numbers of images, the camera was set to take time-lapse images with an interval allowing the stage to be moved between sequential collections of patterns within a particular treatment group. Images of immunofluorescence-stained micropatterns were captured using a 20x objective (EC Plan-NEOF1), with exposures held constant between samples (40ms DAPI; 800ms FITC; 3000ms TRITC).

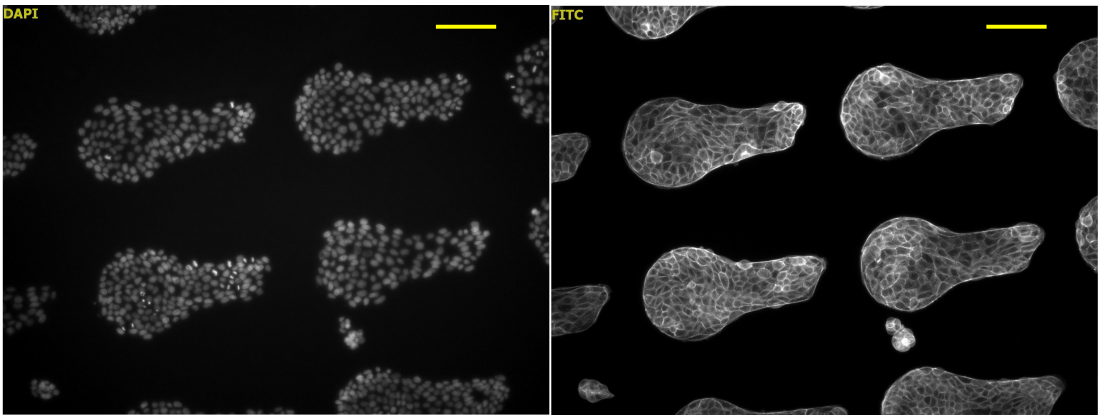

Figure 3.4: **Stained micropatterns.** The panel on the left shows nuclei visible in the DAPI channel, while the panel on the right shows the actin cytoskeleton stained with FITC-phalloidin. Image captured using a 10x objective. A 100 μm scale bar is shown in yellow at the top right of each panel.

All image manipulations were carried out using ImageJ v1.45s and a number of custom scripts written in the built-in macro language (Abràmoff et al., 2004); see Appendix A.1 to A.3 for example scripts. All images, and individual micropatterns within images, were assigned unique code names (anonymised to prevent bias between treatments and controls during analysis), and all manipulations and measurements were tracked to allow for checks, and for new analyses to be conducted and matched with existing data (Fig. 3.5).

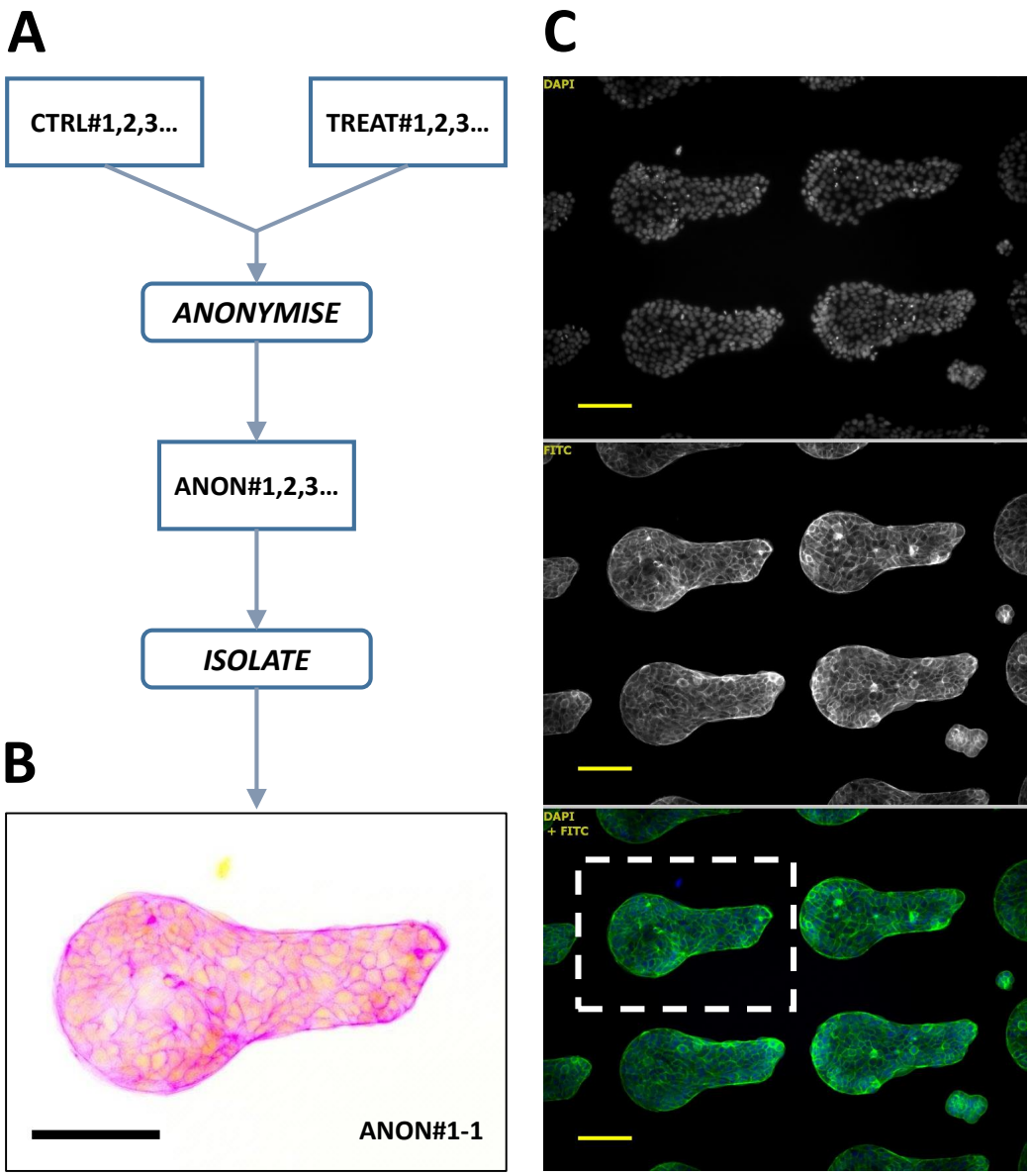

Figure 3.5: **Image processing pipeline.** Custom ImageJ scripts were used to process micropattern images for analysis. Images containing multiple micropatterns were first anonymised (to avoid experimenter bias), and then individual micropatterns were isolated (A). The latter script also inverted the colours of the DAPI-FITC image to make protrusions easier to see on an electronic screen (B), and output the coordinates of the isolated micropattern in the original image (as a ROI or 'region of interest' file) for future reference (C). A 100 µm scale bar is shown at the bottom left of each image panel. See Appendix A.1 and A.2 for scripts.

3.11 Measuring micropattern segments

As can be seen by comparing Figure 3.2A (a schematic of the micropatterned APTMS) with Figure 3.2B (a schematic of the area typically covered by cells, bridging regions of non-adhesive PEG-silane), along with Figure 3.2C (a photomicrograph of cells on a micropattern), the curvatures experienced by cells on the micropattern cannot be measured purely with reference to the micropattern itself; the concave segments in particular are defined by the cells themselves.

Micropattern segments were defined by points of inflection around the edge of the micropattern, and ImageJ was used to manually delineate each segment for length and curvature measurements, ignoring protrusions (see Fig. 3.6A). Length measurements were taken directly, and then ImageJ's 'Fit Circle' function was used to measure the radius of curvature for each segment - defined as the radius of the circle that fits the curve (Fig. 3.6B-C). Curvature was calculated as radius^{-1}, and assigned a negative value for concave curves, and a value of 0 for flat sections (equivalent to a circle with an infinite radius). Measurements were made in pixels and converted into μm based on measurement of a scale bar supplied by the microscope software.

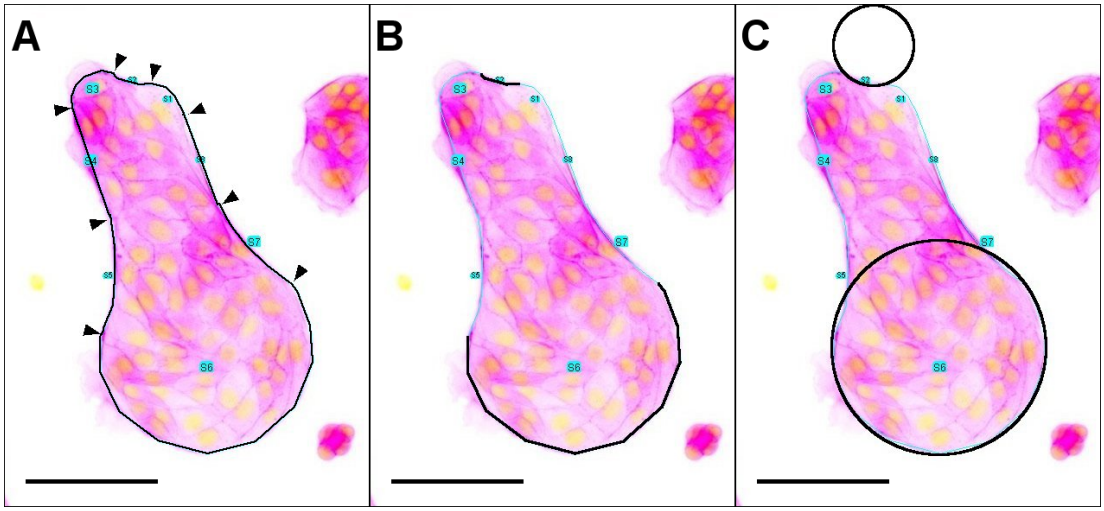

Figure 3.6: **Measuring micropatterns seeded with cells.** ImageJ was used to manually delineate individual segments (chosen to coincide with inflection points around micropattern, and ignoring protrusions), the length of which were then measured. Panel A shows segments recorded using ImageJ (black arrowheads added separately to show where marked segments meet). Circles were then fitted to each segment (B and C, showing example segments), and the radius was measured and used to calculate curvature. Concave segments (as marked at top in B and C) were distinguished by giving curvature a negative sign, and straight segments were assigned a value of 0. A 100 μm scale bar is shown at the bottom left of each panel.

3.12 Counting cells and protrusions

Segments were included in the analysis if the full length of the segment edge conformed to the expected shape of the micropattern and was visible for assessment for protrusions; for example, segments were ignored when debris or cells that were in the process of being extruded had adhered to cells at the segment edge, potentially concealing protrusions, or if cells had migrated outside the borders of the micropattern.

Actin-containing regions that extended outside the recognisable shape of the variable-curvature micropattern (beyond the smooth edges defined by the adherent cells) were counted as active protrusions, with the exception of 'bumps' which could be identified as cells being displaced from the micropattern. The former were typically feathery, irregularly-shaped structures characteristic of lamellipodia. The latter had smooth, rounded edges with a stronger actin signal than true protrusions, and could often be unambiguously identified by the observation of the nucleus partially displaced beyond the edge of the micropattern (see Fig. 3.7). This interpretation of cell displacement, without adhesion to the region surround the micropattern, is supported by observations made by Deforet and colleagues of 3D ridges of MDCK cells forming at the periphery of constraining micropatterns (due to proliferation and differential extrusion), which subsequently bulge slightly over the nonadhesive substrate (Deforet et al., 2014).

Counts were alway done in sequential segments going around in the same direction with reference to the relative length of the micropattern 'fingers': from the tip of the shortest finger (V2) towards the tip of the longest finger (V3). As different batches of micropatterns differed in their orientation, this direction was either clockwise or anti-clockwise depending on the 'handedness' of the micropattern batch.

In order to allow large numbers of segments to be analysed efficiently, while at the same time facilitating data capturing and minimising the risk of errors, an ImageJ script was written to automate data capture from the manual counts (see Appendix A.3). This script allowed protrusions to be counted by 'point-and-click', with key presses to cycle through segments and images, while time-stamped files for counts (with micropattern identifier codes) along with annotated reference images were created automatically. This facilitated the assessment of a total of 4,653 individual micropatterns in the course of this work, of which 27,802 individual segments were considered suitable for analysis, and which yielded a total of 19,256 protrusions counted. A variant of this script was also used separately to facilitate manual counting of individual cells along the edges of segments.

As cells naturally overlapped the borders of the curvature-defined segments, cells and protrusions from such cells had to be assigned to one or other segment for counting. This was done based on a judgement of which segment the cell occupied to a greater extent (i.e. which curvature it was predominantly exposed to). Similarly, broad protrusions originating from multiple adjacent cells were counted as multiple protrusions, based on the number of cells that could be identified as contributing.

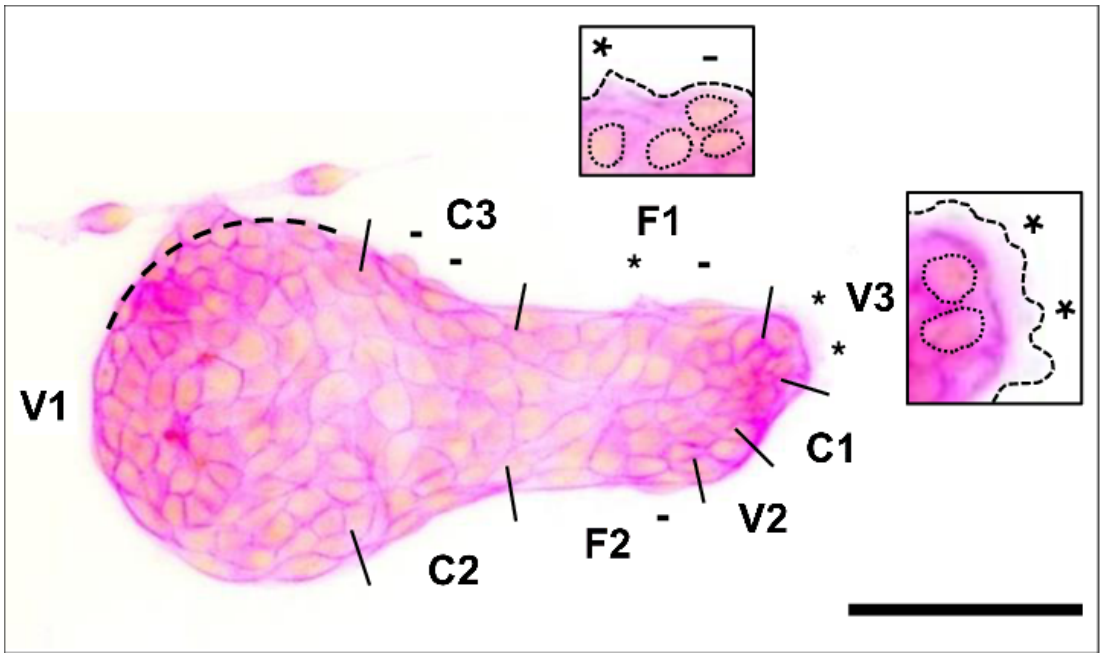

Figure 3.7: **Quantifying protrusions from cells at edges of micropatterns.** MDCK II cells fixed and stained to show actin cytoskeletons (FITC-phalloidin, in pink) and nuclei (DAPI, in yellow), following 24hr culture on a micropattern. Merged FITC and DAPI channels were inverted for easier viewing on an electronic screen. Asterisks (*) mark cells with protrusions in segments F1 and V3; visible as irregular spiky protrusions (F1; observed during live imaging as a transitional phase in lamellipodial dynamics), or as faint, feathery regions of stained actin (V3; typical lamellipodia), that extend beyond the edge of the micropattern. Minus signs (-) mark cells which protrude beyond the boundaries of the standard scaffold shape, but were not counted as true protrusions for the sake of this study (see Section 3.12). Inserts show outlines of protrusions and nuclei marked with thin dashed lines. Segment V1 was ignored, as this segment fails to conform to the standard shape; indicated by the thick dashed line. A 100 μm scale bar is shown at bottom right.

3.13 Statistical analysis

Data captured using ImageJ scripts was processed and analysed using a number of custom scripts written in the R statistical computing language (version 3.2.1; World-Famous Astronaut) within the integrated development environment RStudio (Windows Desktop version 0.99.473) (R Core Team, 2015; RStudio Team, 2015).

Tukey box plots were generated using the 'boxplot' function in R, with the standard whisker range of 1.5x interquartile range (IQR); see Appendix A.4. The distribution of protrusion counts per segment was visualised using histograms, and compared to an overlaid Poisson distribution generated using the 'dpois' function in R (with the mean protrusion count as the parameter for the predicted distribution); see Appendix A.5.

As the data was found to have a distribution that was close to Poisson, and far from Normal, the nonparametric Mann-Whitney-Wilcoxon test (implemented using the 'wilcox.test' function in R; see Appendix A.7) was used to calculate p-values for comparing the distribution of protrusion rates (protrusion counts normalised by segment length) between segments with different curvatures, or under different treatments (Crawley, 2007).

Confidence intervals for protrusion rates at each segment were calculated by bootstrapping (sampling with replacement 1000 times), using the R 'boot' package (Canty and Ripley, 2016); see Appendix A.7. This approach uses the distribution of the data itself to predict the likely range of values, rather than making an estimate based on an idealised distribution (Crawley, 2007).

An Exact Poisson rate ratio test, implemented using the 'rateratio.test' R package contributed by Michael Fay (Fay, 2014), was used as an additional test of the significance of relative differences between protrusion rates. Confidence intervals for protrusion rate ratios were obtained using the results of the 'rateratio.test' function mentioned above. See Appendix A.7 for a custom script that was used to carry out these analyses.

Chapter 4

CURVATURE-PROTRUSION RELATIONSHIP

4.1 Lamellipodial protrusion dynamics

A clonal MDCK II line expressing the actin cytoskeleton marker Lifeact-GFP was used to enable live imaging of the actin cytoskeleton in actively protruding cells constrained to the micropatterns, and to minimise the amount of processing required after fixation for static imaging. Lifeact-GFP is a protein formed from a 17 amino acid-long actin-binding peptide from *Dictyostelium discoideum* ('Lifeact'), fused to Green Fluorescent Protein (GFP) (Riedl et al., 2008). Lifeact-GFP has been shown to have no effect on F-actin dynamics and organisation, and to give an almost fully equivalent visualization of the actin cytoskeleton when compared to phalloidin-based staining, and has consequently been adopted by many researchers as a valuable tool for studying actin cytoskeleton dynamics (Fels et al., 2012; Riedl et al., 2008).

The Lifeact-MDCK cell line was seeded on the micropatterns, and placed in a live imaging chamber for viewing after the cells were established on the pattern. Images were captured every two minutes, and actin-rich protrusions from cells at the perimeter of the micropatterns were observed to extend dynamically over the surrounding nonadhesive substrate; see Figure 4.1. These protrusions typically had the irregular border and feathery appearance of lamellipodia, which have been shown to extend over nonadhesive surfaces, as well as in the presence of adhesion-blocking peptides (Bailly et al., 1998). Narrow spike-like and broader-based triangular protrusions were observed occasionally as transition phases during the establishment and retraction of broad lamellipodia. Live imaging of the micropatterned Lifeact-

MDCK also enabled limited observation of apical actin-based dynamics which appeared characteristic of ruffles; see Figure 4.2. Ruffles are folds in the surface of cells associated with compacted actin, which move centripetally from the cell periphery and indicate both active protrusion-contraction cycles, and frustrated adhesion (Borm et al., 2005; Giannone et al., 2007; Okeyo et al., 2011).

The nature of the micropattern substrate (a relatively thick piece of microscope slide glass) made it challenging to conduct extended imaging sessions of living micropatterned cells, in part due to the additional thickness of the culture plate, and to the fact that the approximately 1 mm-by–1 cm^2 substrate was not attached to the culture plate. The cells inevitably were moved out of the focal plane, despite attempts to buffer the imaging chamber from sources of vibration. Rather than observing the dynamics of cells on individual micropatterns over time, an endpoint approach was taken in experiments, with micropatterned cells being fixed for observation.

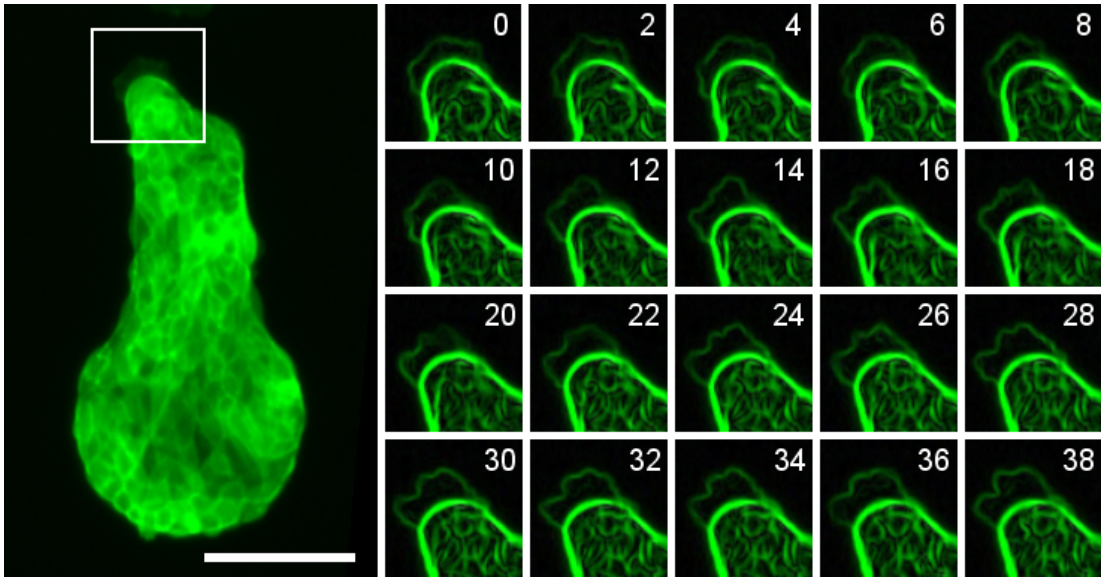

Figure 4.1: **Protrusion dynamics of Lifeact-MDCK on micropatterns.** Images of micropatterned cells were captured every 2 minutes using a 10x objective, and showed irregular, dynamic protrusions at different regions of the periphery. A time-series of a 75 µm-by-75 µm square (marked in the main panel), using ImageJ's built-in Edge Detection algorithm to highlight sharp changes in intensity, shows the fluctuations of a typical protrusion. Some protrusions were very stable over time, as in the example shown here, whereas others appeared and disappeared within a handful of frames. A 100 µm scale bar is shown in the main panel.

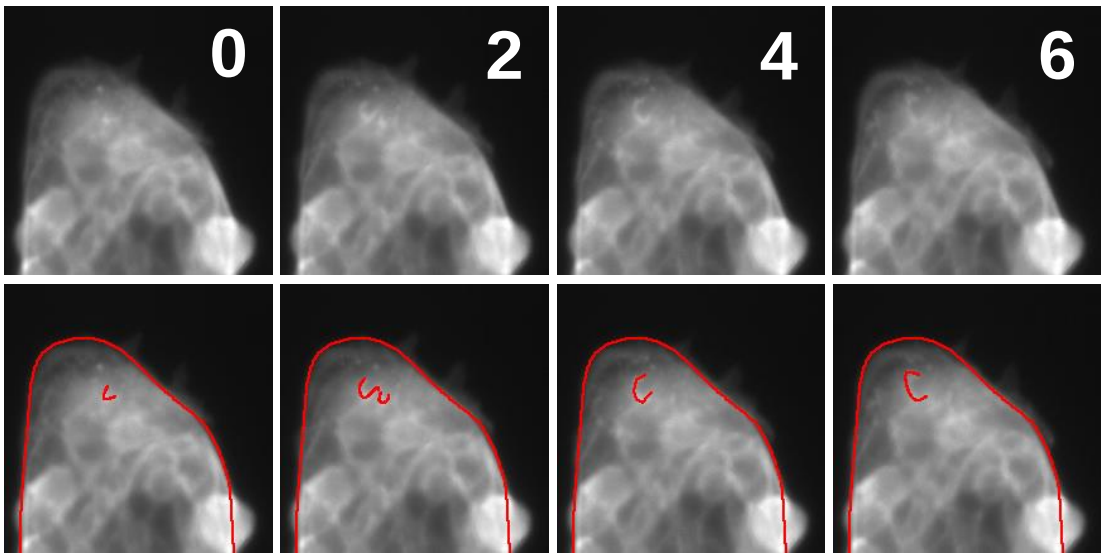

Figure 4.2: **Apical ruffles in live imaged micropatterned cells.** Images of micropatterned Lifeact-MDCK cells were captured every 2 minutes using a 20x objective, and showed evidence of apical surface ruffles driven by actin dynamics. A time-series of the edge of a micropattern (segments V2, C3, and V3 in a 100 μm-by-100 μm square region) shows a typical ruffle, manually traced in the lower panels.

4.2 Micropattern segment measurements

The perimeters of the variable-curvature micropatterns were divided at observed points of inflection, giving eight segments with distinct curvatures. To characterise the segments prior to measuring protrusion rates, ten micropatterns were measured as described (see Fig. 3.6; p.28). Figure 4.3A shows segment curvature measurements (defined as the inverse of the radius of the equivalent circle in units of μm^{-1}, or 0 μm^{-1} in the case of straight, 'flat' segments), and Figure 4.3B shows length measurements; see Table 4.1 and Table 4.2 for the respective statistics. Segments are shown ordered from concave (negative curvature) to convex (positive curvature), using a numbering system that allows for intuitive referencing (C = concave, F = flat, V = convex), as shown in Figure 3.2B (p.22).

Table 4.1: **Micropattern segment curvature measurements (μm^{-1}).** Segments from N representative micropatterns were measured using ImageJ. Curvature values are given, defined as the inverse of the radius of a fitted circle. Negative values denote concave curvature, and zero values were assigned to straight edges. See Fig. 4.3A.

Segment	C1	C2	C3	F1	F2	V1	V2	V3
N	10	10	10	10	10	10	10	10
Mean	-0.021	-0.008	-0.007	0	0	0.012	0.05	0.052
SD[a]	0.007	0.003	0.003	0	0	0.0004	0.01	0.006
Median	-0.022	-0.0073	-0.0070	0	0	0.012	0.048	0.051
IQR[b]	0.007	0.004	0.0037	0	0	0.001	0.014	0.011
Min	-0.030	-0.013	-0.013	0	0	0.012	0.032	0.042
LQ[c]	-0.026	-0.010	-0.0094	0	0	0.012	0.038	0.047
UQ[c]	-0.018	-0.0064	-0.0058	0	0	0.013	0.052	0.057
Max	-0.0054	-0.0035	-0.0028	0	0	0.013	0.063	0.060

[a] Standard deviation. [b] Interquartile range. [c] Lower / Upper quartile.

Table 4.2: **Micropattern segment length measurements (μm).** Segments from N representative micropatterns were measured using ImageJ. Segment edge length measurements were taken by fitting curved lines to segments, which were defined by points of inflection at the edge of the micropatterns. See Fig. 4.3B.

Segment	C1	C2	C3	F1	F2	V1	V2	V3
N	10	10	10	10	10	10	10	10
Mean	32	73	81	100	84	324	33	50
SD[a]	4	9	10	7	5	6	3	5
Median	32	75	82	100	82	324	35	50
IQR[b]	5	14	12	9	6	5	5	3
Min	25	60	60	89	79	315	28	41
LQ[c]	31	66	77	95	81	321	31	49
UQ[c]	36	80	89	104	87	326	36	52
Max	37	86	92	109	93	335	36	61

[a] Standard deviation. [b] Interquartile range. [c] Lower / Upper quartile.

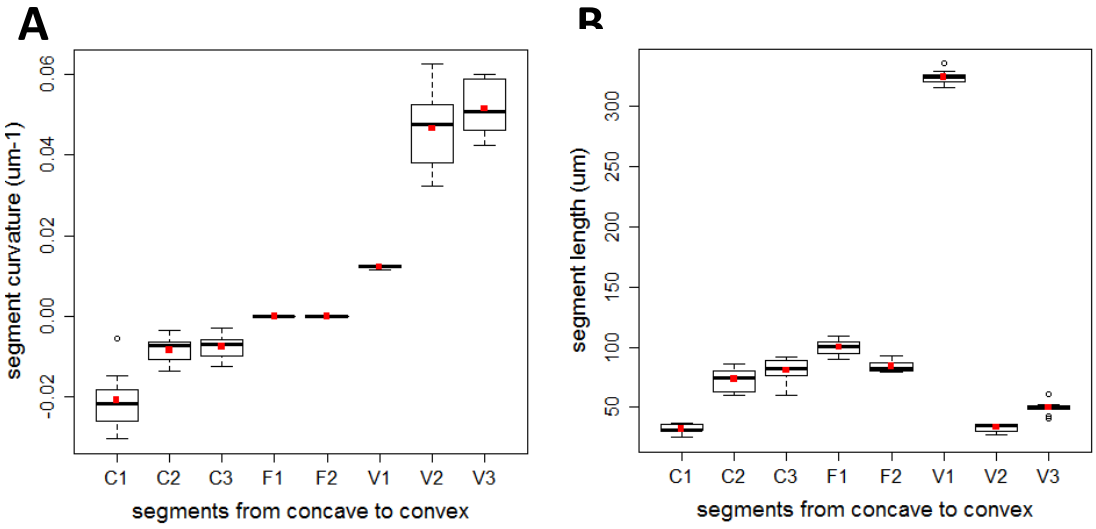

Figure 4.3: **Micropattern segment measurements.** Segments were measured using ImageJ by fitting curved lines to a representative series of images as described (n=10). Segments are coded as shown in Figure 3.2B (p.22). (A) Curvature is calculated as radius^{-1} (units of μm^{-1}); flat segments F1 and F2 were assigned a value of 0. (B) Length is measured in units of μm. Red points represent mean values, and standard Tukey box plot conventions are used (whiskers extend to 1.5x IQR, and outliers are marked as open circles); see Table 4.1 and Table 4.2.

Table 4.3: **Micropattern segment cell counts.** Cells along the edge of segments from N representative micropatterns were counted. FITC-phalloidin and DAPI staining were used to identify cells with the potential to contribute to protrusions (i.e. access to the free edge). See Fig. 4.5A.

Segment	C1	C2	C3	F1	F2	V1	V2	V3
N	45	45	45	45	45	45	45	45
Mean	1.8	2.0	2.4	5.1	4.3	11	1.8	2.2
SD[a]	0.6	0.6	0.6	1.2	1	2	0.6	0.8
Median	2	2	2	5	4	11	2	2
IQR[b]	1	0	1	2	1	2	1	1
Min	1	1	1	3	3	7	1	1
LQ[c]	1	2	2	4	4	10	1	2
UQ[c]	2	2	3	6	5	12	2	3
Max	3	3	3	8	7	14	3	3
Mode	2	2	2	4	4	11	2	3

[a] Standard deviation. [b] Interquartile range. [c] Lower / Upper quartile.

4.3 Micropattern segment cell counts

To compare the numbers of cells occupying each segment edge, images of a representative sample of micropatterns, stained with DAPI and FITC-phalloidin to visualise both nuclei and the actin cytoskeleton, were analysed (see Fig. 4.4). It was far simpler to identify which cells were actually contributing to a visible protrusion, than to identify all cells with sufficient access to the free edge to be potential contributers to potential protrusions; the latter was a slow and inaccurate process.

To compare the packing density of cells at each segment, mean segment lengths (Table 4.2; Fig. 4.3B) were divided by the mean number of cells counted (Table 4.3; Fig. 4.5A), to give an indication of the average space at the edge taken up by individual cells; see Figure 4.5B. For most segments, individual cells took up an average of approximately 20 μm of free edge, whereas in segments C2, C3 and V1, cells took up slightly more space (approximately 30-35 μm per cell on average). This difference may in part be a reflection of patterns of bulk cell movements within the micropattern: live imaged cells were observed to move in complicated flows and vortices within the confines of the micropattern; a phenomenon which has previously been reported in similar experimental systems (Doxzen et al., 2013; Vedula et al., 2012).

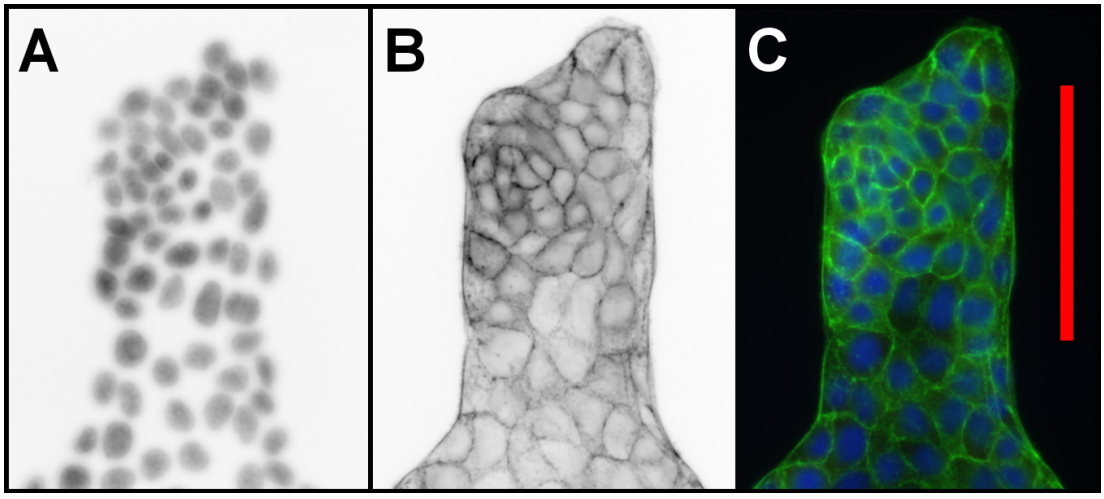

Figure 4.4: **Counting cells available to contribute to protrusions at each segment.** Images of representative micropatterns stained with DAPI (A) and FITC-phalloidin (B) were used to attempt to count cells along each segment edge. The merged DAPI-FITC channel images (C) were used for the actual counts, with the aim of accurately reflecting the number of cells with unrestricted access to the area beyond the micropattern. A 100 μm scale bar is shown in red in Panel C.

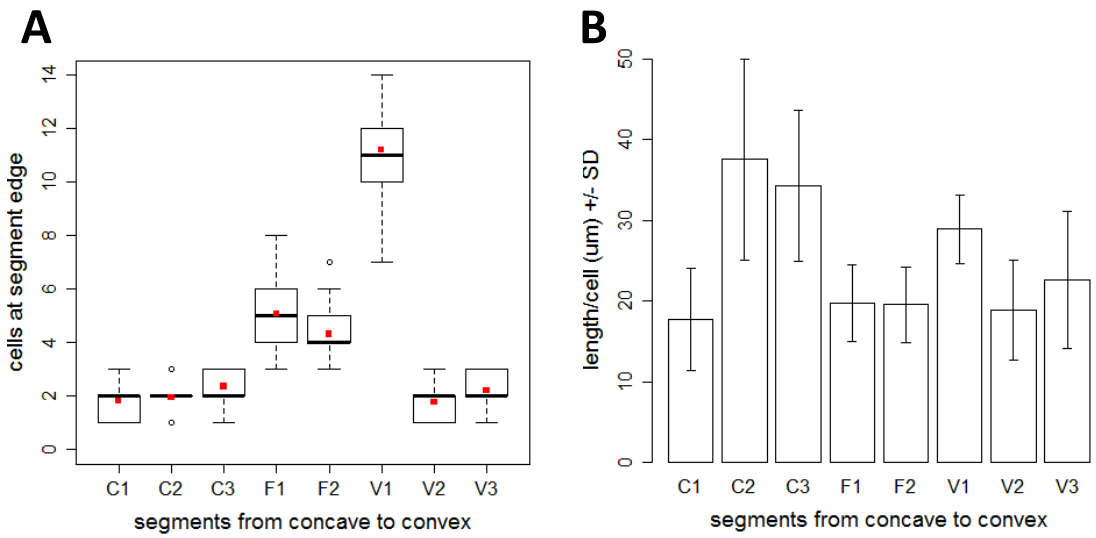

Figure 4.5: **Micropattern segment cell counts.** (A) Cells adjacent to the edge of micropatterns and available to contribute to protrusions within each segment were counted in a representative series of images as described (n=45). Red points represent mean cell counts, and standard Tukey box plot conventions are used (whiskers extend to 1.5x IQR, and outliers are marked as open circles); see Table 4.3. (B) Mean values for segment length measurements (see Table 4.2) are shown normalised by mean values for segment cell numbers, giving an indication of the length typically occupied by individual cells at the edge of the micropattern. Values for standard deviation of cell count-normalised length measurements were calculated using the formula: $\sigma = (a/b)\sqrt{(\sigma_a/a)^2 + (\sigma_b/b)^2)}$, where a and b are average values of segment length and cell count, and σ_a and σ_b are their respective standard deviations. See Appendix A.4.

4.4 Protrusions from cells at different curvatures

Lifeact-MDCK were seeded on micropatterns and cultured for 24 hours before being fixed, and protrusions from each segment were counted. For the most part, the protrusion count distributions for each segment were a good match for the expected Poisson distribution (see Fig. 4.6; p. 40). The red lines overlaid on the protrusion frequency barplots were generated using the 'dpois' function in R; setting the parameter equal to the mean protrusion rate for each segment. As well as showing a distribution that is a close fit to the simulated Poisson values, the data for the majority of the segments also have the typical characteristic of variance values being approximately equal to the mean (Crawley, 2007).

Of the four segments, F1 and V1 exhibit over-dispersion in the distribution of protrusion counts (defined as having a variance greater than the mean), while V2 and V3 have distributions that are under-dispersed. Over-dispersion can occur due to the influence of an additional confounding variable, which broadens the distribution of the count data (Crawley, 2007). Observing the relationship between the protrusion counts at each segment, and the segment edge cell counts (extrapolated from a smaller sample), suggests that segment cell density is the variable responsible: segments with over-dispersed protrusion counts also have edge cell counts with a greater range, likely due to their greater length. As control and treated micropatterns were seeded using the same cell suspension, and the cell suspension was prepared in the same way for each experiment, this variable was considered to be effectively randomised within and between experiments.

The under-dispersion of protrusion counts in segments V2 and V3 can also be explained with reference to the respective segment cell densities. The distribution of protrusion counts in these segments appear truncated to the right when compared to the more typical Poisson shapes of the other segments. This suggests that the protrusion counts are being constrained by a ceiling, and the overlap with the distribution of segment edge cell counts supports this interpretation of a maximum protrusion rate being approached at these two segments.

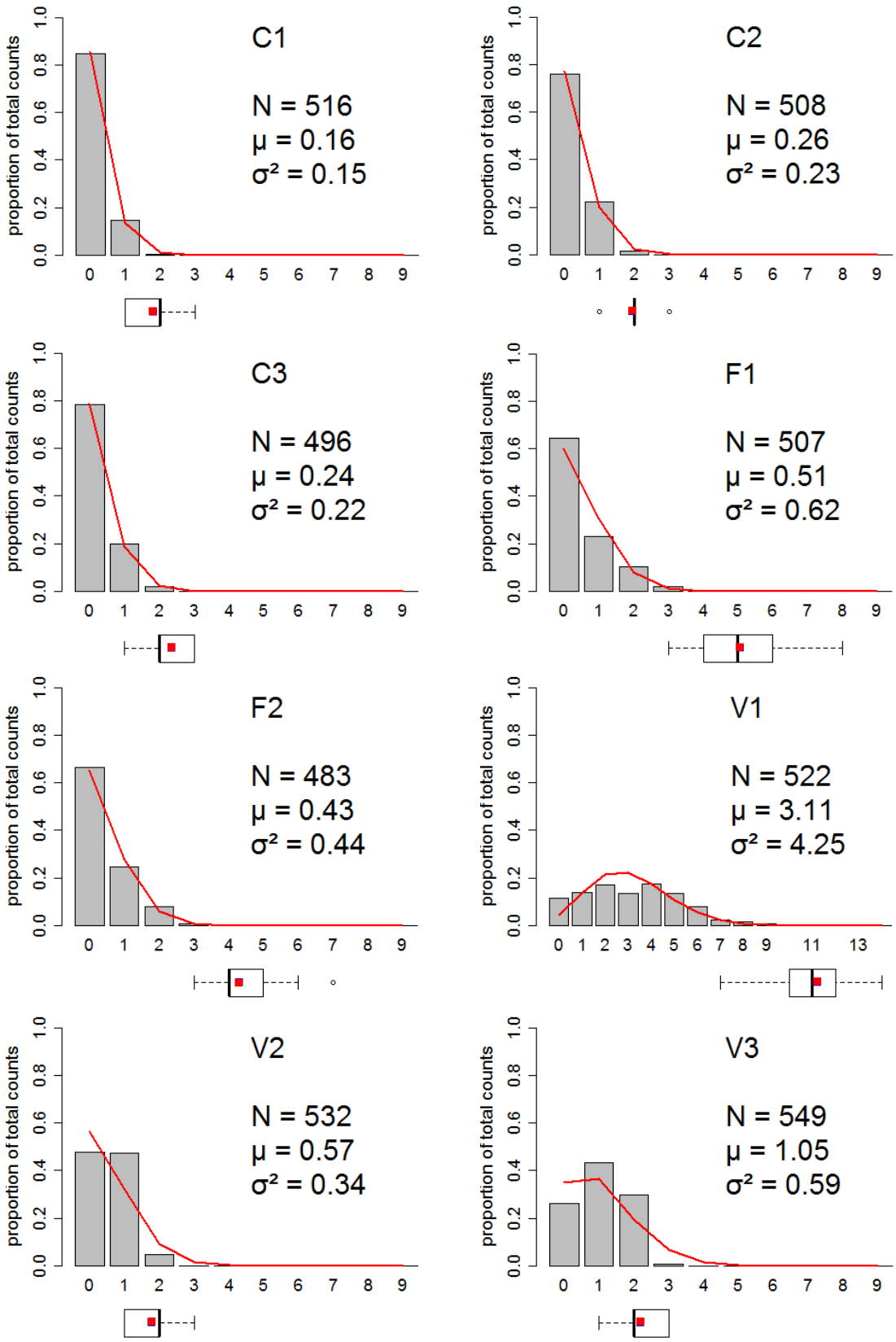

Figure 4.6: **Protrusion count frequency with cell counts by segment.** Protrusion count values are shown as a proportion of total counts, and plots show number of segments analysed (N; total from three independent experiments), mean value of counts (μ), and variance (σ^2). The predicted Poisson distribution is shown as a red line. Boxplots under histograms show segment edge cell counts from Table 4.3 (Fig. 4.5A). See Appendix A.5.

4.5 Normalising protrusion counts between segments

In order to compare protrusion rates between segments, it was necessary to normalise protrusion counts to take into account differences in segment length. Given the relatively large sample sizes needed for each segment, and the impracticality of identifying the total number of cells available to contribute to protrusions at each segment in each micropattern analysed, it was decided to normalise protrusion counts based on the simple measure of median segment edge length (Table 4.2), to give a value of protrusions per μm.

Use of perimeter length as a proxy for cell numbers in normalising lamellipodia counts is an approach that has been successfully used in previous studies of protrusive behaviour in cell collectives (Farooqui and Fenteany, 2005; Rolli et al., 2012; Yang et al., 2016). However, as Figure 4.6 indicates, it must be acknowledged that failing to take segment cell density into account introduces a potentially confounding variable, which could conceal or introduce variation in the data if not successfully randomised.

Given the length of each segment, and the range of edge cell counts, some systematic error can be predicted and thus taken into account when interpreting results. Normalising by segment length instead of by segment cell count introduces the risk of under- or overestimating differences in protrusion rates between segments, as segments may differ significantly in edge cell density (see Fig. 4.5B and Fig. 4.7A). Ideally, as a proxy, length-normalised protrusion rates would have a linear relationship to cell-normalised protrusion rates. However, plotting the relationship between the two for each segment (comparing the rates calculated for a single protrusion in each segment; Table 4.4), shows that protrusion rates for certain segments (C2, C3, V1 and V3) are likely to be underestimated relative to other segments when length-normalisation is used (see Fig. 4.7B).

Table 4.4: **Comparing cell- vs segment length-normalisation.** Given the median segment length measurements recorded in Table 4.2, and the median, minimum, and maximum segment cell counts recorded in Table 4.3, normalised protrusion rates were calculated assuming a single protrusion in each segment. See Fig. 4.7.

Seg.	A: Length	1/A[a]	B: Med[b]	1/B[c]	C: Max[b]	1/C[c]	D: Min[b]	1/D[c]
C1	32	0.032	2	0.50	3	0.33	1	1
C2	75	0.013	2	0.50	3	0.33	1	1
C3	82	0.012	2	0.50	3	0.33	1	1
F1	100	0.010	5	0.20	8	0.13	3	0.33
F2	82	0.012	4	0.25	7	0.14	3	0.33
V1	324	0.003	11	0.09	14	0.07	7	0.14
V2	35	0.028	2	0.50	3	0.33	1	1
V3	50	0.020	2	0.50	3	0.33	1	1

[a] Protrusion rate when normalising against segment length. [b] Median / Maximum / Minimum segment cell counts. [c] Protrusion rate when normalising against segment cell count.

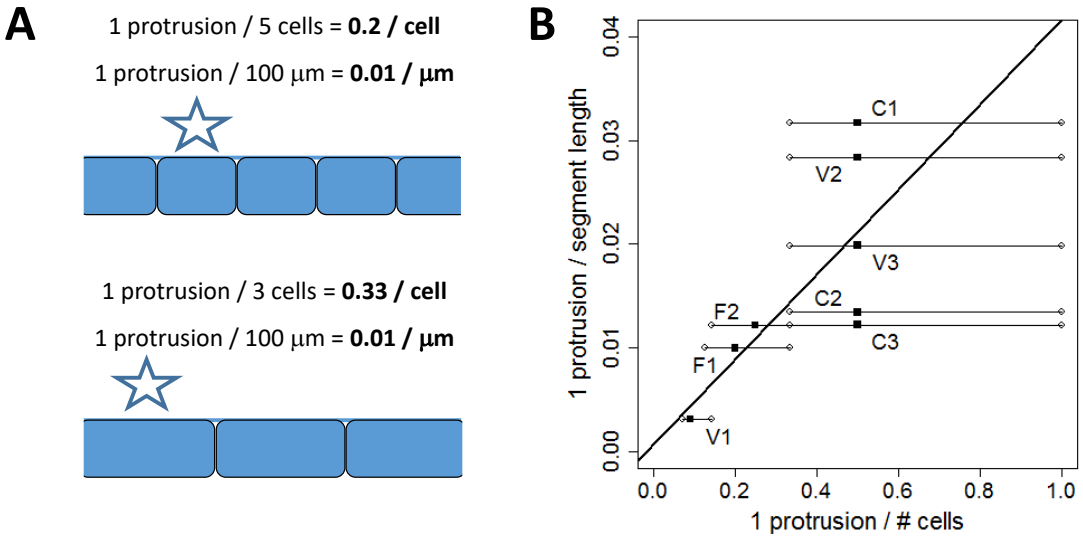

Figure 4.7: **Theoretical relationship between protrusion rates calculated using cell- vs length-normalisation.** Protrusion rates were calculated for a single protrusion in each segment, based on length, and on cell edge count (including median, maximum, and minimum counts); see Table 4.4, and diagram in Panel A (protruding cell marked with a star). Plotting the relationship between length- and cell-normalised values shows that protrusion rates for certain segments (C2, C3, V1 and V3) are likely to be underestimated relative to other segments when length-normalisation is used (B).

4.6 Protrusion rate relationship with curvature

Normalising the protrusion count values shown in Figure 4.6 by their respective segment lengths allows protrusion rates to be compared across all segment curvatures. Table 4.5 and Figure 4.8A show the distribution of protrusion rates within each segment, while Table 4.6 and Figure 4.8B show the pairwise comparisons between 'curvature-adjacent' segments. Taking into account the potential for underestimation of segments C2, C3, V1 and V3 discussed earlier, it is clear that there is a strong relationship between curvature and protrusion, with more convex segments having higher protrusion rates. These results confirmed the observations of other researchers, and validated the variable-curvature micropattern culture system as a platform for further investigation into the underlying mechanism of this relationship.

Table 4.5: **Protrusion rates for each segment.** Protrusions from N segments of untreated micropatterns were counted, and counts were normalised using median segment length to give protrusion rates in units of μm^{-1}. See Fig. 4.8A.

Segment	C1	C2	C3	F1	F2	V1	V2	V3
N	516	508	496	507	483	522	532	549
Mean	0.005	0.0035	0.0029	0.0051	0.0052	0.0096	0.016	0.021
SD[a]	0.012	0.0064	0.0057	0.0079	0.0081	0.0064	0.017	0.015
Median	0	0	0	0	0	0.0093	0.028	0.02
IQR[b]	0	0	0	0.01	0.012	0.012	0.028	0.04
Min	0	0	0	0	0	0	0	0
LQ[c]	0	0	0	0	0	0.0031	0	0
UQ[c]	0	0	0	0.01	0.012	0.015	0.028	0.04
Max	0.063	0.027	0.024	0.04	0.036	0.028	0.057	0.06
Mode	0	0	0	0	0	0.012	0	0.02

[a] Standard deviation. [b] Interquartile range. [c] Lower / Upper quartile.

Table 4.6: **Change in protrusion rate with curvature.** Segments were compared pair-wise in order of curvature. Differences and ratios of mean protrusion rates (from Table 4.5) between 'curvature adjacent' segments are given, along with the results of the Mann-Whitney-Wilcoxon and exact Poisson rate ratio tests. See Fig. 4.8B.

Segments	Diff.	MW p-value[a]	Ratio	95% CIL[b]	95% CIU[b]	RR p-value[c]
C1-C2	-0.0015	0.0380*	0.69	0.52	0.92	0.0121*
C2-C3	-0.0006	0.0112*	0.83	0.64	1.07	0.1645
C3-F1	0.0022	0.0001***	1.76	1.41	2.20	0.0000***
F1-F2	0.0001	0.3106	1.02	0.85	1.23	0.8583
F2-V1	0.0044	0.0000***	1.84	1.59	2.14	0.0000***
V1-V2	0.0064	0.0052**	1.68	1.48	1.90	0.0000***
V2-V3	0.0050	0.0003***	1.29	1.12	1.49	0.0003***

[a] Mann-Whitney-Wilcoxon test p-value. [b] Upper / Lower 95% confidence limits for the ratio of mean protrusion rates, calculated using an exact Poisson rate ratio test. [c] Exact Poisson rate ratio test p-value. Asterisks highlight significance (* < 0.05; ** < 0.01; *** < 0.001).

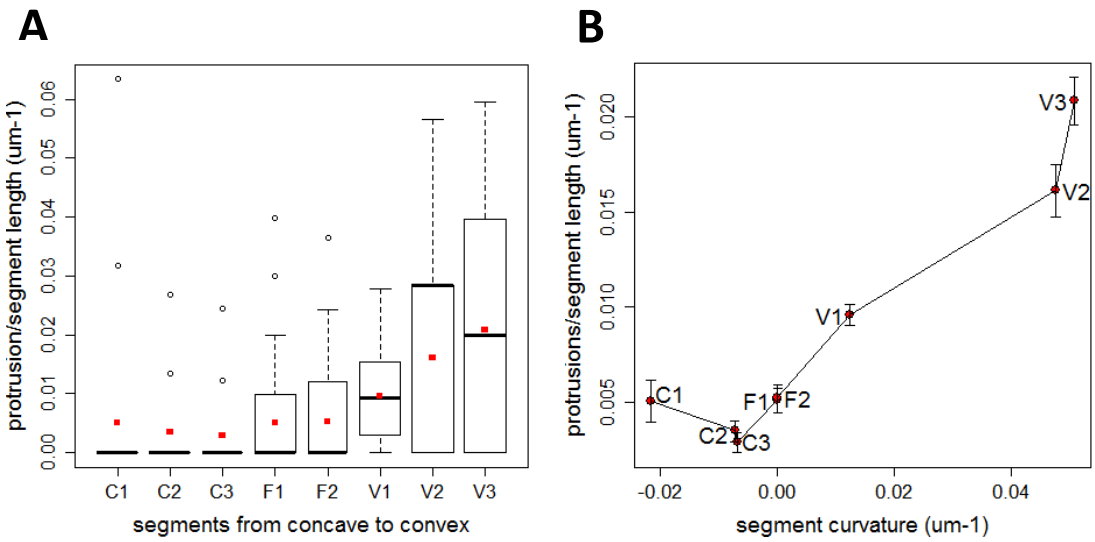

Figure 4.8: **Change in protrusion rate with curvature.** Protrusion rates were calculated by normalising counts of protrusions by segment length. (A) Distribution of protrusion rates by segment. Red points represent mean values, and standard Tukey box plot conventions are used (whiskers extend to 1.5x IQR, and outliers are marked as open circles); see Table 4.5. (B) Protrusion rates (mean ± bootstrapped 95% confidence interval) show a strong positive trend with curvature. See Table 4.6 for p-values comparing protrusion rate distributions between 'curvature adjacent' segments.

Chapter 5

PERFUSION CULTURE FOR GRADIENT DISRUPTION

5.1 Autocrine inhibitor accumulation hypothesis

As was described in Section 2.5, one potential explanation for the relationship between protrusion and curvature, at least in three-dimensional, matrix-embedded multicellular collectives, involves the secretion of a diffusible autocrine inhibitor of protrusion (Nelson et al., 2006). In this model, gradient formation depends only on the spatial organisation of the secreting cells, with no need for differential secretion rates: cells present at convex curves experience a lower concentration of diffusing inhibitor, while those at concave curves experience a higher concentration as the inhibitor accumulates in the 'well' they form. While the authors were able to provide some convincing support for their model, and subsequent work has suggested a general role for autocrine inhibitor secretion in patterning branching morphogenesis (Davies et al., 2014), it remained unclear whether this proposed mechanism could be part of the explanation for the analogous relationship between curvature and protrusion seen in a two-dimensional, matrix-free system.

Whereas Nelson et al. were able to support the likely role of an autocrine inhibitor by targeting a particular cytokine, TGFβ1, in their mammary cell system, TGFβ1 has been shown to have a positive rather than negative effect on motility in the MDCK II cell line (Peinado et al., 2003). As an alternative to taking a targeted approach that would involve identifying candidate inhibitors, a blanket approach was taken initially: using perfusion culture to interfere with any autocrine signaling that might be playing a role in the observed curvature-protrusion relationship.

5.2 Disruption of gradients by perfusion

Perfusion culture has previously been used to clearly demonstrate perturbation of autocrine signalling in cultured cells (Blagovic et al., 2011). The basic principle is to subject cells to a constant flow of media, washing away cell-secreted factors before they can generate a response. Blagovic and colleagues were able to use an elegant microfluidic device to interrogate the separate roles of various cell-secreted factors in the differentiation and growth of embryonic stem cells; supplementing the cells with exogenous cytokines while flushing away the autocrine signals.

Perfusion experiments are complicated by the need to balance multiple interdependent parameters, which if done incorrectly can lead to misleading results. How the volumetric flow rate through the system is experienced by the cells depends on the dimensions of the chamber, with smaller dimensions translating to higher flow velocities. In order to have a significant impact on autocrine signalling, the flow velocity must be significant when compared to the rate of diffusion of the molecular species involved (Squires et al., 2008). However, flow velocity and mass transport increase at the expense of increased shear stress (Mazzei et al., 2010).

5.3 Responses of cells to flow conditions

Shear stress due to tangential fluid flow can have profound effects on cellular phenotypes. Renal epithelial cells, including MDCK cells, are known to be sensitive to changes in fluid flow; a characteristic that has been partly ascribed to the specialised hair-like mechanosensor known as the primary cilium. While primary cilia are not present in MDCK cells within the <2 day window after passage used in these experiments, MDCK lacking cilia have also been shown to respond to shear stress with elevated intracellular calcium levels (Rodat-Despoix et al., 2013). Perfusion experiments can be designed to test whether an observed effect is due to confounding shear stress effects: if an effect is observed, repeating the experiment with conditioned media can determine whether the original effect was due to shear, or to the removal of an important diffusible signal (which is added back with the conditioned media) (Blagovic et al., 2011).

Although it is possible to test whether the results of a perfusion experiment are due to shear stress, ideally an experiment of this type will be designed to provide sufficient perfusion to perturb diffusing signal gradients, while at the same time ensuring shear stress is below the level where it becomes a confounding variable. Previous work on the effects of shear stress on MDCK cells have shown that, un-

like endothelial cells, they do not align in response to flow. However, they do exhibit threshold-dependent changes in cytoskeletal architecture in response to shear stress (Wang et al., 2010). Application of physiological shear stress of 0.074 Pa and above leads to significant restructuring within the first hours of exposure: disassembly of central focal adhesions and stress fibres, and increases in actin and adhesions at the periphery (Verma et al., 2015). However, shear stress of 0.054 Pa has limited effect on MDCK cells, even after extended exposure (Wang et al., 2010).

5.4 The Quasi-Vivo system

The Quasi-Vivo perfusion culture chamber was developed by Ahluwalia and colleagues with the express aim of minimising the shear stress experienced by cultured cells, while maximising mass transport. The placement of the inlet and outlet tubes (9 mm and 10 mm above the base of the chamber), along with the relatively large volume of the chamber, contribute to the improvements over simpler linear chambers. Its use has been successfully demonstrated with 'difficult' shear-sensitive, metabolically-demanding primary hepatocytes; maintaining viability and liver-specific function (Mazzei et al., 2010). The chambers are designed to hold 13 mm diameter coverslips, and substrates of up to 5 mm thick (Sbrana and Ahluwalia, 2012), and so were suitable for the 1 mm-thick micropattern substrates. See Figure 3.3 (p.24) for chamber dimensions and micropattern placement.

Prior to setting up the experiment with micropatterned cells, unpatterned MDCK II were cultured under flow conditions for 12 hours, with a flow rate of $3\,\mathrm{mL\,min^{-1}}$. Although the Quasi-Vivo QV500 manual recommends a maximum flow rate of $1\,\mathrm{mL\,min^{-1}}$, no difference in viability, proliferation rates, or morphology were seen when compared to control cells.

Unlike a linear flow chamber, the Quasi-Vivo chamber does not lend itself to a simple calculation of flow velocity and shear stress from flow rate (Sbrana and Ahluwalia, 2012). Using equations developed from a three-dimensional simulation of the fluid dynamics by Ahluwalia and colleagues, estimates of flow velocity and shear stress experienced by cells on a 160 µm-thick coverslip can be calculated as follows (Mazzei et al., 2010):

$$\text{Shear (Pa)} = \text{Flow } (\mu\mathrm{L\,min^{-1}}) \times 1.8 \times 10^{-8} + 1.1 \times 10^{-6} \tag{5.1}$$

$$\text{Flow Speed } (\mathrm{m\,s^{-1}}) = \text{Flow } (\mu\mathrm{L\,min^{-1}}) \times 2.6 \times 10^{-9} + 1.3 \times 10^{-7} \tag{5.2}$$

At a volumetric flow rate of $3\,\mathrm{mL\,min^{-1}}$, this solves to a flow velocity of $7.93\,\mu\mathrm{m\,s^{-1}}$,

and a shear stress of 5.51×10^{-5} Pa. These figures are underestimates of the true values experienced by cells on the 1 mm-thick micropattern substrate, as reducing the distance between the cell surface and the flow inlet increases both shear and flow velocity (Mazzei et al., 2010).

A very conservative estimate for effect of the 0.84 mm height increase with the use of the micropattern substrates instead of a coverslip can be made, based on the fact that raising the culture surface by 3 mm in an earlier iteration of the Quasi-Vivo chamber resulted in a 10-fold increase in shear stress (Mazzei et al., 2010). Taking this as a ceiling would have the calculated shear stress increase to a maximum of approximately 0.0005 Pa; far lower than the 0.054 Pa threshold for MDCK cytoskeletal effects previously mentioned.

The sufficiency of the chosen flow rate to disrupt the hypothesized autocrine signaling gradient is supported by calculations of the dimensionless Péclet and Damköhler numbers for this system, using parameters estimated by Blagovic et al. when solving a similar problem (Blagovic et al., 2011). The Péclet number (Pe) gives an indication of the relative importance of convective (fluid flow) versus diffusive transport, and a value >>1 indicates that convection dominates. The Damköhler number (Da) gives an indication of the relative importance of reaction (receptor binding) versus diffusion, and a value >1 indicates that diffusion time is limiting relative to reaction speed (Blagovic et al., 2011; Squires et al., 2008).

$$\mathrm{Pe} = v_{mean} h / D_L \tag{5.3}$$

$$\mathrm{Da} = k_{on} R_S h / D_L \tag{5.4}$$

where v_{mean} is the mean flow velocity, h is the internal height of the chamber, D_L is the diffusivity of the molecule(s) of interest, k_{on} is the receptor-ligand binding constant, and R_S is the receptor density.

Finally, the ratio of these two numbers (Pe/Da) gives an indication of the relative importance of convection versus reaction, and a value >>1 indicates that convection dominates the system; in other words, that the flow velocity is sufficient to remove the diffusing species before they are able to bind with the cell receptors in significant quantities (Blagovic et al., 2011).

Carrying out these calculations with conservative parameters for k_{on}, R_S and D_L suggested by Blagovic et al., gives an estimated value for (Pe/Da) of 150. See Appendix A.6 for details of calculations; note that the actual value of (Pe/Da) is likely to be even higher, given the underestimation of flow velocity (and thus Pe) based

on the position of the substrate in the chamber. This indicates that a flow rate of $3\,\mathrm{mL\,min^{-1}}$ is sufficient to disrupt the hypothesised autocrine inhibitor gradient.

Additional, empirical validation of this system has subsequently been conducted by collaborators, and the results have been included as supplemental data for submission of a jointly-authored publication (see Appendix A.8). Briefly, two fluorophore-labelled proteins with differing affinity for MDCK II cell surface glycoproteins (Wheat Germ Agglutinin, with high affinity, and an antibody with no significant affinity for the cell surface) were introduced into the Quasi-Vivo chamber, and flow was applied. The Wheat Germ Agglutinin was retained, bound to the micropatterned cells, proving that the introduced proteins had access to the cell surface. The antibody was rapidly cleared from the chamber, demonstrating that the flow rate used for these experiments was capable of clearing proteins from the media at the cell surface.

5.5 Culture of micropatterned cells under flow conditions

Micropatterned cells were cultured under flow conditions in parallel with the static cultures described in the previous chapter. Flow and control micropatterns were seeded using a single cell suspension in each experiment, and cultures were treated identically in the 24 hours prior to the transfer of the former to the Quasi-Vivo flow chamber. At the point of initiating flow treatment, control micropatterns were transferred to a dish with a volume of media equivalent to the total volume in the Quasi-Vivo system (25 mL).

After exposure to flow conditions for 1.5 hours, micropatterned cells were removed from the Quasi-Vivo flow chamber and fixed for observation along with the controls. As expected based on the calculation of shear stress in the system (Eqn. 5.1) as being below the threshold for cytoskeletal reorganisation in flow-exposed MDCK, no differences could be seen between control and flow treated cells in terms of their gross cytoskeletal organisation, or the general appearance of the micropatterned collectives (see Fig. 5.1).

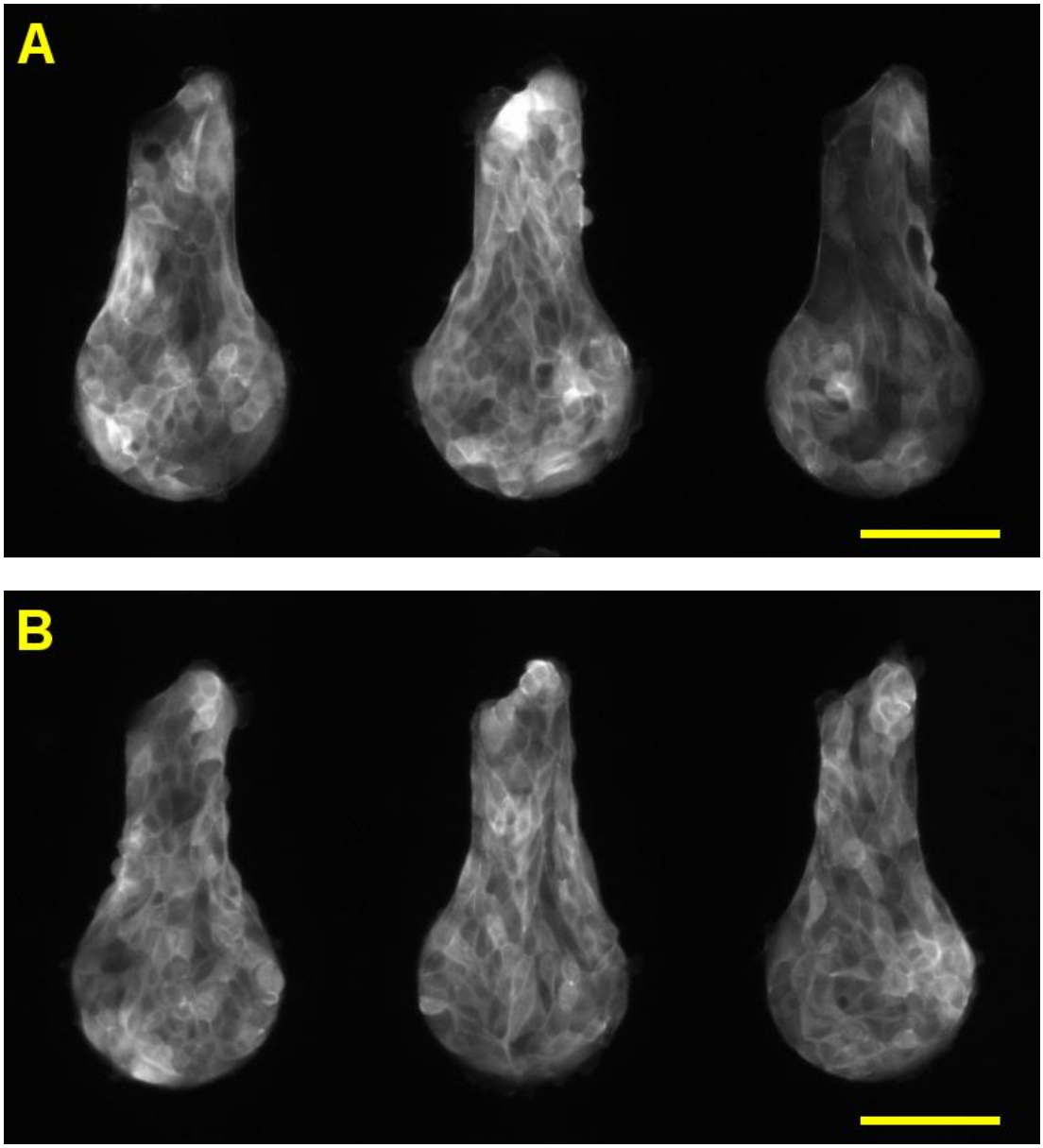

Figure 5.1: **Flow-treated vs control micropatterns.** Representative micropatterned cells treated with (A) and without (B) exposure to flow of media. The actin cytoskeleton is labelled by expression of the fluorescent Lifeact-GFP construct, and images were captured using a 10x objective. There is no appreciable difference in phenotype between cells under flow or control conditions, although some heterogeneity in Lifeact-GFP expression between cells in both conditions was noted. A 100 μm scale bar is shown in yellow at the bottom of each panel.

5.6 Curvature-protrusion relationship is insensitive to flow

As described in Section 3.7, micropatterns were placed in the Quasi-Vivo flow chamber with long axis parallel to the direction of flow, and with the 'fingers' (segments C1, V2 and V3) toward the inlet (see Fig. 3.2B on page 22). This was done to ensure consistency, and with the expectation that the three segments at the upstream end of the micropattern (C1, V2, V3), would show the effects of the maximum reduction in the hypothesised inhibitory cytokine, and consequently show an increase in protrusion rate.

More generally, it was expected that subjecting the micropattern to constant media flow would reduce the concentration of any inhibitory cytokine sensed by cells at all segments; resulting in a general increase in protrusion rates at all segments. Any 'downstream' effect of increased exposure to the inhibitory cytokine would be shown by a decrease in protrusion rate at segment V1. If an autocrine inhibitor of protrusion plays a significant role in shaping the relationship between curvature and protrusion, culture of the micropatterns under flow conditions should cause a loss of the clear distinction between protrusion rates at concave and convex segments.

Counting protrusions in flow-treated micropattern segments and normalising by median segment length as described in the previous chapter showed that the relationship between curvature and protrusion was unchanged by exposure to flow: concave (C) and flat (F) segments had low protrusion rates, and convex (V) segments showed a positive relationship between curvature and protrusion rate. In contrast to another prediction made above, assuming secretion of an autocrine inhibitor of protrusion, there was no general trend of increased protrusion rates at all segments.

Comparing protrusion rates in control and flow-treated micropatterns for each segment did show small differences at some segments. Flow-treated micropatterns showed a slight increase at both flat segments (F1 and F2) and at one of the concave segments (C3), as well as a slight decrease at the most convex segment (V3); see Table 5.1, Table 5.2 and Figure 5.2. While the increases at C3, F1, and F2 might suggest that the concentration of an autocrine inhibitor is being reduced, this conclusion is challenged by the lack of significant change at 'upstream' segment C1 in particular, as well as by the decrease in the protrusion rate at 'upstream' segment V3. It was concluded that, although statistically significant, the differences in protrusion rates were too small to indicate a meaningful effect of flow treatment, and could be explained by small variations in culture conditions between control and

flow-treated cells.

These results are in keeping with previous work in carried out by other students in this lab (Stimac, 2013), and are evidence against the hypothesis that geometry-dependent gradients of an autocrine inhibitor of protrusion are responsible for the curvature-protrusion relationship seen in cells constrained to two-dimensional micropatterns. These findings have been submitted to the Journal of Anatomy, and the manuscript has been accepted for publication; see Appendix A.8.

An alternative to a mechanism dependent on 'chemical' cues is one dependent on 'mechanical' cues, as discussed in Section 2.5. The results of an Atomic Force Microscopy (AFM) study of live micropatterned cells, carried out by collaborators and discussed in the next chapter, provided additional motivation to examine the role for cellular mechanotransduction in sensing differential substrate curvature.

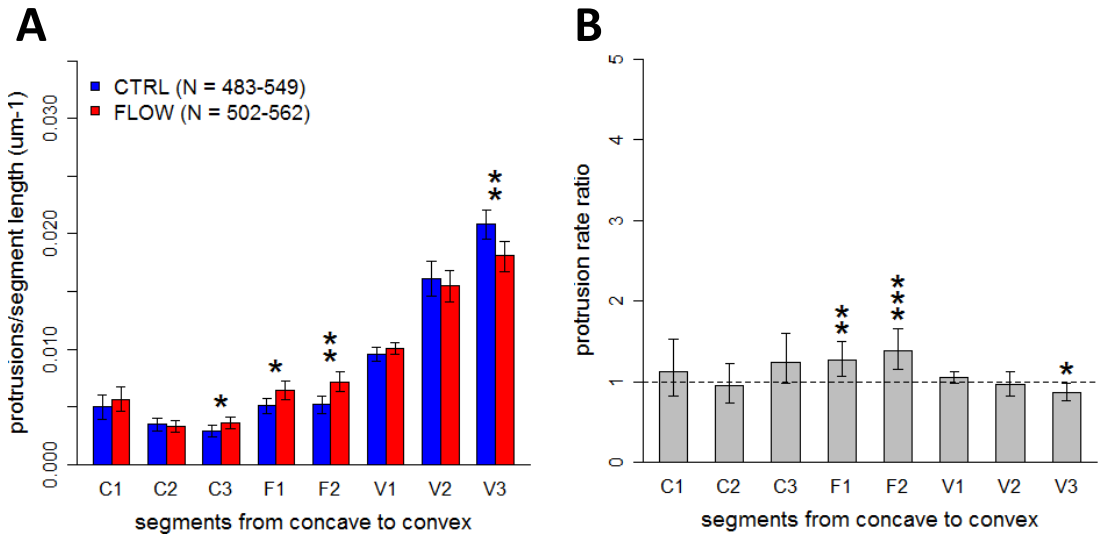

Figure 5.2: **Protrusion rates under flow conditions.** Protrusion rates were calculated by normalising counts of protrusions by segment length. (A) Protrusion rates (mean ± bootstrapped 95% CI) show a strong positive trend with curvature, with only minor variations between the control and flow conditions (stars highlight significant p-values from Mann-Whitney-Wilcoxon test; * < 0.05; ** < 0.01; *** < 0.001). (B) Protrusion rate ratios, 95% confidence intervals, and p-values (significance indicated by stars) were calculated using an exact Poisson rate ratio test. See Table 5.1 and Table 5.2.

Table 5.1: **Protrusion rates under flow conditions.** Protrusions from N segments of untreated (-) and treated (+) micropatterns were counted, and counts were normalised using median segment length to give protrusion rates in units of μm^{-1}. See Fig. 5.2A.

Segment	Flow	N	Mean	95% CIL[a]	95% CIU[a]	SEM[b]
C1	(-)	516	0.0050	0.0039	0.0060	0.0005
C1	(+)	518	0.0056	0.0046	0.0067	0.0006
C2	(-)	508	0.0035	0.0030	0.0041	0.0003
C2	(+)	517	0.0033	0.0028	0.0038	0.0003
C3	(-)	496	0.0029	0.0024	0.0034	0.0003
C3	(+)	534	0.0036	0.0031	0.0041	0.0003
F1	(-)	507	0.0051	0.0044	0.0058	0.0003
F1	(+)	506	0.0064	0.0057	0.0072	0.0004
F2	(-)	483	0.0052	0.0044	0.0059	0.0004
F2	(+)	502	0.0072	0.0064	0.0081	0.0004
V1	(-)	522	0.0096	0.0090	0.0102	0.0003
V1	(+)	562	0.0101	0.0095	0.0106	0.0003
V2	(-)	532	0.0161	0.0146	0.0176	0.0007
V2	(+)	540	0.0155	0.0141	0.0168	0.0007
V3	(-)	549	0.0209	0.0196	0.0221	0.0006
V3	(+)	562	0.0181	0.0167	0.0194	0.0007

[a] Upper / Lower 95% confidence limits for mean protrusion rates, calculated using bootstrapping. [b] Standard error of the mean.

Table 5.2: **Change in protrusion rates in response to flow conditions.** Untreated and treated segments were compared. Differences and ratios of mean protrusion rates (from Table 5.1) between conditions are given, along with the results of the Mann-Whitney-Wilcoxon and exact Poisson rate ratio tests. See Fig. 5.2B.

Segments	Diff.	MW p-value[a]	Ratio	95% CIL[b]	95% CIU[b]	RR p-value[c]
C1	0.0006	0.4588	1.12	0.82	1.52	0.5115
C2	-0.0002	0.7373	0.95	0.74	1.22	0.7431
C3	0.0007	0.0413*	1.24	0.97	1.59	0.0821
F1	0.0013	0.0178*	1.26	1.07	1.49	0.0059**
F2	0.0020	0.0011**	1.39	1.16	1.66	0.0003***
V1	0.0005	0.2423	1.05	0.98	1.12	0.1466
V2	-0.0007	0.5851	0.96	0.81	1.13	0.6392
V3	-0.0028	0.0033**	0.87	0.77	0.98	0.0200*

[a] Mann-Whitney-Wilcoxon test p-value. [b] Upper / Lower 95% confidence limits for the ratio of mean protrusion rates, calculated using an exact Poisson rate ratio test. [c] Exact Poisson rate ratio test p-value. Asterisks highlight significance (* < 0.05; ** < 0.01; *** < 0.001).

Chapter 6

DRUG TREATMENTS

6.1 Atomic Force Microscopy (AFM)

Atomic Force Microscopy (AFM) is a technique that is used to assess the mechanical properties of cells. It involves the indentation of the cell surface with a probe attached to a cantilever, the deflection of which is measured to calculate the force required to indent the surface. Elastic Modulus is defined as the ratio of stress (applied force) to strain (deformation); a higher Elastic Modulus indicates a material is more resistant to deformation, and is a property that is associated with stiffer objects (Janmey and Schliwa, 2008; Schillers et al., 2010).

AFM data comparing the Elastic Modulus of live cells at different curvatures was provided by collaborators at the University of Glasgow; acquired using indentation with silica microsphere probes, as previously described (McPhee et al., 2010). Measurements taken over the nucleus showed no significant difference in elasticity between cells at different segments, whereas measurements taken at the periphery (in regions of the cells with a height of between 500–900nm) suggested that peripheries of cells at the convex segments (V1, V2, V3) were significantly stiffer than at flat and concave regions, with an increase in Elastic Modulus on the order of between 2- and 8-fold. Interestingly, the values calculated with measurements taken at the concave segments (C1, C2) were also larger than that of the flat segment (F2), on the order of about 2-fold. In order of highest to lowest Elastic Modulus: convex $>$ concave $>$ flat.

Differences in Elastic Modulus between cells and parts of cells can be ascribed to differences in cellular structure and mechanical state. Generally, stiffness can be a reflection of the amount of prestress in a tensegrity structure (which cells can often be usefully modelled as), with increased tension resulting in increased stiffness (In-

gber et al., 2014). As predicted, inhibiting cellular contractility can be shown to reduce the tension in actin cables (measured using a genetically-encoded FRET sensor) (Suffoletto et al., 2015), and to reduce cellular stiffness (measured using AFM) (Schillers et al., 2010). Properties of the actin cytoskeleton that can impact on cellular stiffness, such as organisation and degree of cross-linking, as well as recruitment of active myosin, are controlled by actin-associated proteins with activity that may vary dramatically in response to temporal or spatial cues. For example, several tropomyosin isoforms have recently been shown to differentially affect the Elastic Modulus over the nucleus when overexpressed (Jalilian et al., 2015).

Cellular mechanotransduction requires mechanical integrity and prestress to effectively channel forces through the cell to activate mechanosensitive components (Ingber et al., 2014). Reduction in cellular stiffness is correlated with a loss of normal mechanotransduction-associated responses, such as inhibition of proliferation on pliable substrates, and durotaxis (migration up gradients of increasing substrate stiffness) (Lin et al., 2015). The different Elastic Modulus values seen at the periphery of MDCK II cells at different segments of the variable-curvature micropatterns suggested that mechanotransduction, or differential mechanosensitivity, plays a role in the observed curvature-protrusion relationship, and motivated the work described in this chapter, with an initial focus on the possible role of a mechanosensitive calcium channel.

6.2 Phalloidin-staining of the actin cytoskeleton

Although the Lifeact-GFP construct used to visualise the actin cytoskeleton was indispensable for live imaging of protrusions, an undesirable degree of heterogeneity in the fluorescence signal was present even within the clonal Lifeact-MDCK line used (see Fig. 5.1). The work reported in this chapter was conducted using cells stained with FITC-phalloidin.

Phalloidin is a small peptide sourced from the *Amanita phalloides* mushroom. It has a high affinity for filamentous actin (F-actin), and fluorescent derivatives have been in use for decades to visualise the actin cytoskeleton in fixed cells (Wulf et al., 1979). While phalloidin conjugates are generally considered directly equivalent to the genetic actin probe Lifeact-GFP for visualising fixed cells (Fels et al., 2012; Riedl et al., 2008), it has been reported that the latter fail to incoporate into filopodia, and give a higher background signal when compared to phalloidin staining (Belin et al., 2014).

6.3 Ionomycin and BAPTA-AM

The divalent calcium ion (Ca^{2+}) has many roles in cell signalling, including significant involvement in aspects of control of the actin cytoskeleton. Cyclic increases in Ca^{2+} at the leading edge of migrating cells cause lamellipodia retraction and strengthening of adhesions via the activation of non-muscle myosin II (Tsai and Meyer, 2012). Ca^{2+} may also play a role in the extension of lamellipodia via activation of the GTPase Rac (Price et al., 2003), and acts through mediators such as CaMKII to stimulate F-actin polymerisation (Hoffman et al., 2013). Intracellular calcium concentrations are commonly manipulated using drugs that artificially increase the cytoplasmic levels of Ca^{2+} by transporting the ions across membranes down concentration gradients (ionophores), and using drugs that sequester intracellular calcium from its targets (calcium chelators).

Ionomycin and BAPTA-AM were chosen as agents to perturb calcium signalling in micropatterned cells, to determine whether differential activation of calcium channels was responsible for the observed curvature-protrusion dependence. By raising the level of intracellular Ca^{2+} globally (in the case of Ionomycin), or sequestering intracellular Ca^{2+} globally to prevent activation of calcium-responsive effectors (in the case of BAPTA-AM), it was reasoned that the localisation and role of any such channel activation would be made clear.

For example, if calcium channel activation was a feature of the convex regions, and responsible for stimulating protrusions locally, then Ionomycin should increase the protrusion rate at the flat and concave regions, while BAPTA-AM should inhibit protrusions at the convex regions (see Fig. 6.1A). Conversely, if calcium channel activation was a feature of the concave regions, and responsible for inhibiting protrusions locally, then Ionomycin should reduce the protrusion rate at the convex regions, and BAPTA-AM should stimulate protrusions at the concave regions (see Fig. 6.1B).

In the latter model involving strain-activated calcium influx in the concave regions, a more global perspective as suggested in Section 2.5 leads to a slightly more nuanced additional prediction. Calcium-mediated myosin activation and increase in tension at the concave regions could be expected to translate to increased traction force applied to the focal adhesions at the flanking convex segments. If this is the case, in addition the the prediction shown in Figure 6.1B (increased protrusions at concave regions on BAPTA-AM treatment and relief of local inhibition), sequestration of intracellular calcium by BAPTA-AM would result in less force transmitted to focal adhesions, and a reduction in protrusions at the convex regions. In contrast,

the local inhibitory effect of Ionomycin in this model would be expected to counter any global protrusion-promoting effects, so Ionomycin treatment would still be expected to inhibit protrusions at convex regions.

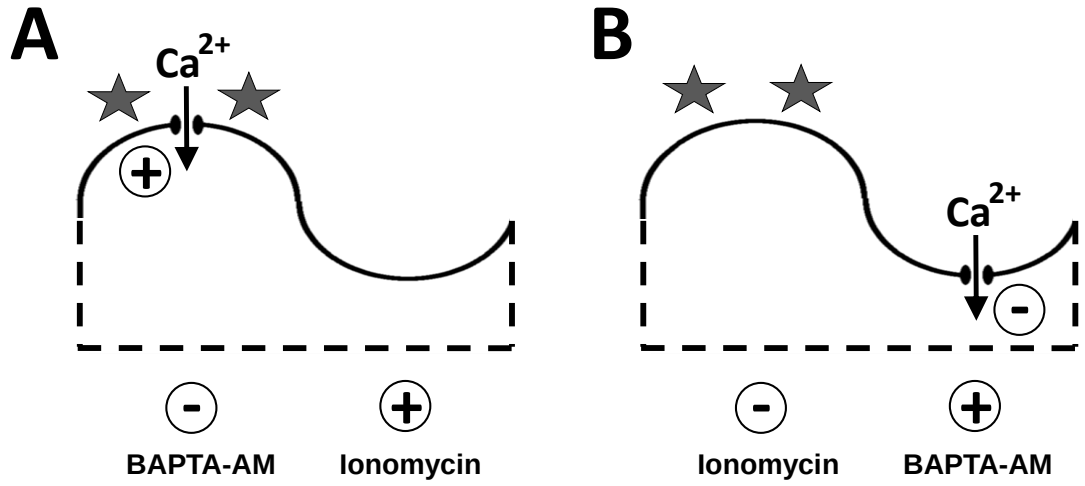

Figure 6.1: **Alternative calcium channel hypotheses.** (A) If calcium influx via activated channels at the convex regions is responsible for promoting protrusions, then BAPTA-AM and Ionomycin should have negative and positive effects on protrusion, respectively. The converse is true in the alternative hypothesis (B), where calcium influx at the concave regions is responsible for inhibiting protrusions locally. Stars represent protrusions at convex curves.

Ionomycin is an antibiotic produced by *Streptomyces conglobatus* that functions as an ionophore with a strong preference for calcium: each molecule forms a complex with one divalent calcium ion, and is able to diffuse across lipid membranes (Liu and Hermann, 1978). Although it was originally considered to mediate increases in intracellular Ca^{2+} simply by direct transport down gradients, it has been found to act primarily to redistribute the intracellular stores of calcium into the cytoplasm (seen as a initial spike in cytoplasmic $[Ca^{2+}]$), with the subsequent elevated plateau being due to cell-mediated extracellular calcium influx (Müller et al., 2013).

Ionomycin treatment has been shown to increase the amount of polymerised F-actin in T-lymphocytes (Dushek et al., 2008), and a similar ionophore has been shown to be sufficient for the assembly of a rim of F-actin in the perinuclear region in fibroblasts (Shao et al., 2015). Ionomycin has also been shown to modulate the contractility of treated cells: increased activation of myosin II in a MLCK-dependent manner has been shown for MDCK cells (Jin et al., 2001), and 2 μM is sufficient to elevate myosin II activation in myofibroblasts for an hour after treatment (Zhao et al., 2007). Treatment with Ionomycin results in an increase in cellular Elastic Modulus in epithelial cells, reflecting a role for calcium in modulating the stiffness of the actin cortex via activation of myosin II. Conversely, reducing intracellular

Ca^{2+} using BAPTA-AM has the opposite effect (Schillers et al., 2010).

BAPTA-AM is a cell-permeable molecule that is trapped in the cytosol on cleavage by cellular esterases, simultaneously taking on the ability to specifically chelate divalent calcium ions. These qualities led to it being considered useful as a buffer against changes in intracellular Ca^{2+} (Tymianski et al., 1994). BAPTA-AM has been used to demonstrate the requirement for intracellular Ca^{2+} in the assembly of tight junctions in MDCK cells. Treatment with 25 μM significantly attenuated the increase in transepithelial resistance seen when cells were permitted to form adhesions. The same authors also showed the lack of toxicity of BAPTA-AM: treatment of MDCK cells with intact tight junctions had no effect on transepithelial resistance, and cells which had been treated with BAPTA-AM for extended periods were able to recover normal function (Stuart et al., 1994).

BAPTA-AM at 10 μM has been used support a role for stretch-activated calcium channels in the remodelling of the actin cytoskeleton at cell-cell adhesions in fibroblasts subjected to pulling forces: untreated cells showed actin polymerisation at intercellular junctions, while the effect was abolished with intracellular Ca^{2+} chelation (Ko et al., 2001). Similarly, BAPTA-AM treatment has been shown to have a suppressive effect on lamellipodia in endothelia within an hour of treatment (Higashida et al., 2013), although monolayer wound-closure in an epithelial MDCK line appeared unaffected (Farooqui and Fenteany, 2005).

6.4 Disruption of calcium signaling

Micropatterned cells were treated in parallel with either 10 μM BAPTA-AM or 2.5 μM Ionomycin prior to being fixed and stained with FITC-phalloidin and the nuclear stain DAPI. Treatment duration was one hour, for direct comparison with the previous perfusion culture experiments, and to allow for processes that act over longer time periods, such as actin stress fibre re-alignment (Katsumi et al., 2002). This is a longer time frame than is commonly used for Ionomycin in particular, but Ionomycin at 2 μM has been shown to successfully sustain elevated Ca^{2+} in primary renal epithelial cells for up to an hour (Ishikawa and Saito, 1990).

Ionomycin-treated cells showed a pronounced increase in cytoplasmic F-actin, visualised as FITC-phalloidin staining (see Fig. 6.2). This is in keeping with the recent report of perinuclear actin polymerisation in response to Ca^{2+} influx in fibroblasts, and supports the effectiveness of Ionomycin in maintaining consistently high intracellular Ca^{2+} levels, as perinuclear F-actin has been observed to depolymerise

rapidly on the return of Ca^{2+} to normal levels (Shao et al., 2015). In addition, an increase in cells being displaced outside the bounds of the micropattern was observed, which might reflect the expected increase in MLCK-mediated contractility of the cells in the collective (Jin et al., 2001).

Micropatterned cells treated with Ionomycin showed a strong trend of significant reduction of protrusion rates at convex (V) segments. The apparent slight increase in protrusion rates seen for some of the concave (C) segments could be due to misidentifying some partially displaced cells as protrusions (see Table 6.1, Table 6.2 and Fig. 6.3). These results were supportive of a possible role for calcium channel activation at the concave regions, with an inhibitory role for Ca^{2+} influx in controlling protrusions locally (reproduced at the convex regions by Ionomycin; see Fig. 6.1B).

However, while the Ionomycin results supported a potential role for inhibitory Ca^{2+} signaling at the concave segments, the BAPTA-AM results failed to support this model. If a local influx in Ca^{2+} at concave regions plays a role in constraining protrusions locally, then BAPTA-AM treatment should relieve this inhibition, and increase the protrusion rate at the concave segments (see Fig. 6.1B). However, there was no visible effect of treatment on the micropatterned cells (see Fig. 6.4), and no trend of increased protrusion at the flat (F) or concave (C) segments (see Table 6.3, Table 6.4 and Fig. 6.5). In addition, there was no sign of a reduction in the protrusion rate at the convex (V) segments, indicating that calcium influx at concave regions was not responsible for promoting protrusions at convex regions via a transmission of tension to focal adhesions at the latter.

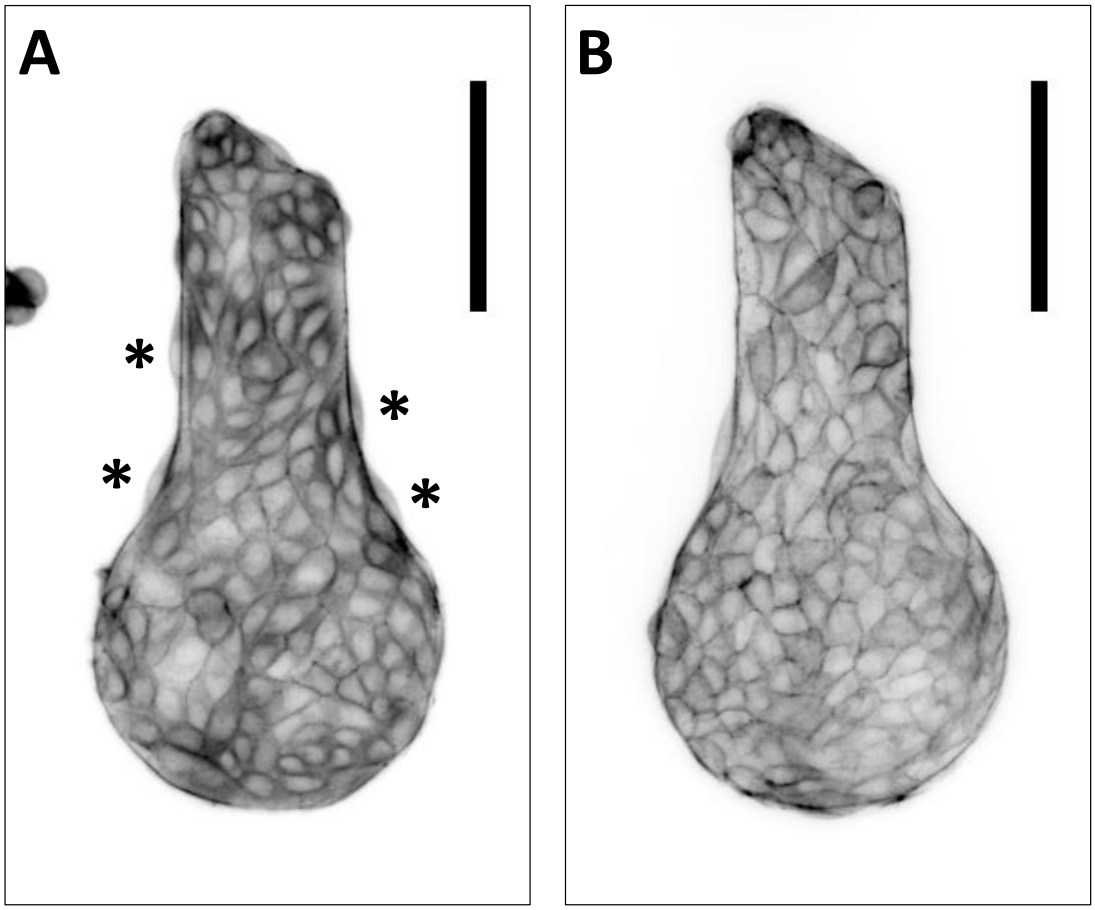

Figure 6.2: **Ionomycin-treated vs control micropatterns.** Representative micropatterned cells treated with (A) and without (B) 2.5 μM Ionomycin, and stained with FITC-phalloidin. The Ionomycin-treated cells (A) show an increase in F-actin within the cytoplasm, compared to the control. A peripheral actin cable is present in both, and there seemed to be a slight increase in the number of 'displaced' cells at the edge of the Ionomycin-treated micropatterns (marked with asterisks; each showing the nucleus displaced past the thick peripheral actin cable), suggesting an increase in tension in the collective. A 100 μm scale bar is shown at the top right of each panel.

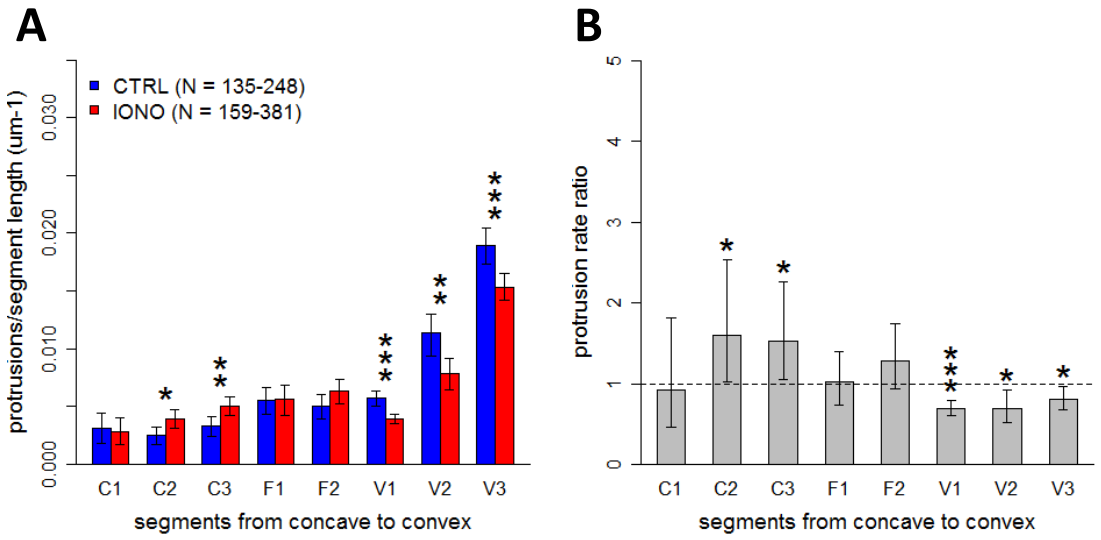

Figure 6.3: **Protrusion rates with Ionomycin treatment.** Protrusion rates were calculated by normalising counts of protrusions by segment length. (A) Protrusion rates (mean ± bootstrapped 95% CI) show a positive trend with curvature, which is reduced with Ionomycin treatment. The latter shows both an increase in protrusions at some concave segments, and an appreciable decrease in protrusions at all convex segments (stars indicate significant p-values from Mann-Whitney-Wilcoxon test; * < 0.05; ** < 0.01; *** < 0.001). (B) Protrusion rate ratios, 95% confidence intervals, and p-values (significance indicated by stars) were calculated using an exact Poisson rate ratio test. See Table 6.1 and Table 6.2.

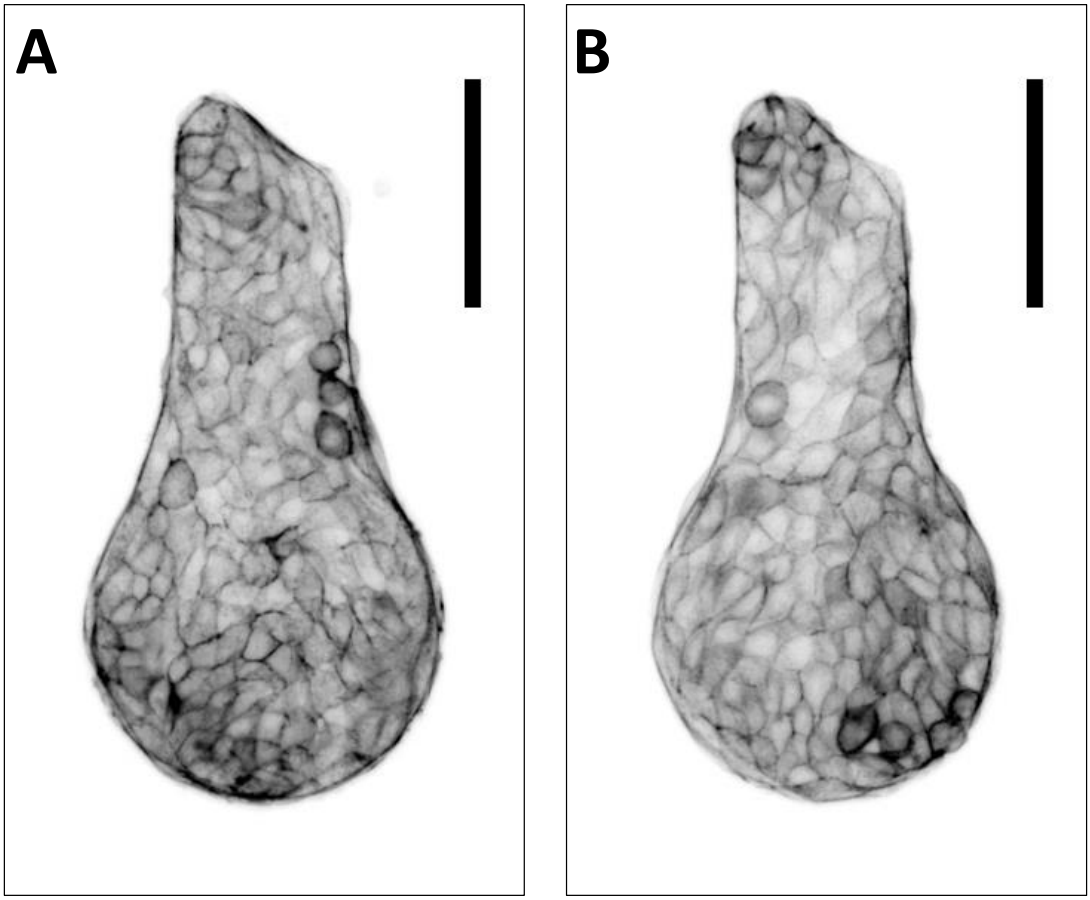

Figure 6.4: **BAPTA-AM-treated vs control micropatterns.** Representative micropatterned cells treated with (A) and without (B) 10 μM BAPTA-AM, and stained with FITC-phalloidin. There is no notable difference between the treatments. A peripheral actin cable is present in both. A 100 μm scale bar is shown at the top right of each panel.

Table 6.1: **Protrusion rates under Ionomycin treatment.** Protrusions from N segments of untreated (-) and treated (+) micropatterns were counted, and counts were normalised using median segment length to give protrusion rates in units of μm^{-1}. See Fig. 6.3A.

Segment	Ionomycin	N	Mean	95% CIL[a]	95% CIU[a]	SEM[b]
C1	(-)	193	0.0031	0.0018	0.0044	0.0007
C1	(+)	221	0.0029	0.0017	0.0040	0.0006
C2	(-)	167	0.0025	0.0017	0.0032	0.0004
C2	(+)	213	0.0040	0.0032	0.0048	0.0004
C3	(-)	159	0.0033	0.0024	0.0041	0.0005
C3	(+)	210	0.0051	0.0042	0.0059	0.0004
F1	(-)	135	0.0055	0.0043	0.0066	0.0006
F1	(+)	159	0.0056	0.0043	0.0069	0.0007
F2	(-)	165	0.0050	0.0039	0.0060	0.0006
F2	(+)	230	0.0064	0.0052	0.0074	0.0005
V1	(-)	213	0.0057	0.0051	0.0064	0.0003
V1	(+)	326	0.0040	0.0035	0.0044	0.0002
V2	(-)	241	0.0114	0.0094	0.0130	0.0009
V2	(+)	381	0.0079	0.0065	0.0091	0.0007
V3	(-)	248	0.0189	0.0174	0.0204	0.0008
V3	(+)	374	0.0153	0.0142	0.0166	0.0006

[a] Upper / Lower 95% confidence limits for mean protrusion rates, calculated using bootstrapping. [b] Standard error of the mean.

Table 6.2: **Change in protrusion rates with Ionomycin treatment.** Untreated and treated segments were compared. Differences and ratios of mean protrusion rates (from Table 6.1) between conditions are given, along with the results of the Mann-Whitney-Wilcoxon and exact Poisson rate ratio tests. See Fig. 6.3B.

Segments	Diff.	MW p-value[a]	Ratio	95% CIL[b]	95% CIU[b]	RR p-value[c]
C1	-0.0003	0.7833	0.92	0.47	1.82	0.9158
C2	0.0015	0.0209*	1.59	1.02	2.53	0.0395*
C3	0.0018	0.0022**	1.53	1.05	2.26	0.0251*
F1	0.0001	0.5111	1.02	0.74	1.40	0.9687
F2	0.0014	0.0805	1.28	0.94	1.74	0.1217
V1	-0.0018	0.0000***	0.69	0.60	0.79	0.0000***
V2	-0.0035	0.0017**	0.69	0.52	0.92	0.0109*
V3	-0.0036	0.0004***	0.81	0.68	0.97	0.0203*

[a] Mann-Whitney-Wilcoxon test p-value. [b] Upper / Lower 95% confidence limits for the ratio of mean protrusion rates, calculated using an exact Poisson rate ratio test. [c] Exact Poisson rate ratio test p-value. Asterisks highlight significance (* < 0.05; ** < 0.01; *** < 0.001).

Table 6.3: **Protrusion rates under BAPTA-AM treatment.** Protrusions from N segments of untreated (-) and treated (+) micropatterns were counted, and counts were normalised using median segment length to give protrusion rates in units of μm^{-1}. See Fig. 6.5A.

Segment	BAPTA-AM	N	Mean	95% CIL[a]	95% CIU[a]	SEM[b]
C1	(-)	193	0.0031	0.0016	0.0044	0.0007
C1	(+)	223	0.0037	0.0023	0.0050	0.0007
C2	(-)	167	0.0025	0.0017	0.0033	0.0004
C2	(+)	176	0.0043	0.0034	0.0053	0.0005
C3	(-)	159	0.0033	0.0023	0.0042	0.0005
C3	(+)	175	0.0035	0.0024	0.0045	0.0005
F1	(-)	135	0.0055	0.0043	0.0066	0.0006
F1	(+)	177	0.0055	0.0043	0.0066	0.0006
F2	(-)	165	0.0050	0.0039	0.0060	0.0006
F2	(+)	219	0.0050	0.0040	0.0059	0.0005
V1	(-)	213	0.0057	0.0051	0.0064	0.0003
V1	(+)	221	0.0053	0.0047	0.0060	0.0003
V2	(-)	241	0.0114	0.0095	0.0132	0.0009
V2	(+)	278	0.0131	0.0113	0.0149	0.0009
V3	(-)	248	0.0189	0.0174	0.0205	0.0008
V3	(+)	278	0.0184	0.0171	0.0197	0.0007

[a] Upper / Lower 95% confidence limits for mean protrusion rates, calculated using bootstrapping. [b] Standard error of the mean.

Table 6.4: **Change in protrusion rates with BAPTA-AM treatment.** Untreated and treated segments were compared. Differences and ratios of mean protrusion rates (from Table 6.3) between conditions are given, along with the results of the Mann-Whitney-Wilcoxon and exact Poisson rate ratio tests. See Fig. 6.5B.

Segments	Diff.	MW p-value[a]	Ratio	95% CIL[b]	95% CIU[b]	RR p-value[c]
C1	0.0006	0.6419	1.18	0.63	2.26	0.6832
C2	0.0019	0.0034**	1.74	1.11	2.80	0.0149*
C3	0.0002	0.8283	1.06	0.69	1.63	0.8740
F1	-0.0001	0.5908	0.99	0.72	1.35	0.9878
F2	0	0.8166	1.00	0.72	1.39	1.0000
V1	-0.0004	0.4481	0.93	0.80	1.07	0.3095
V2	0.0017	0.2071	1.15	0.88	1.52	0.3208
V3	-0.0005	0.6314	0.97	0.81	1.16	0.7820

[a] Mann-Whitney-Wilcoxon test p-value. [b] Upper / Lower 95% confidence limits for the ratio of mean protrusion rates, calculated using an exact Poisson rate ratio test. [c] Exact Poisson rate ratio test p-value. Asterisks highlight significance (* < 0.05; ** < 0.01; *** < 0.001).

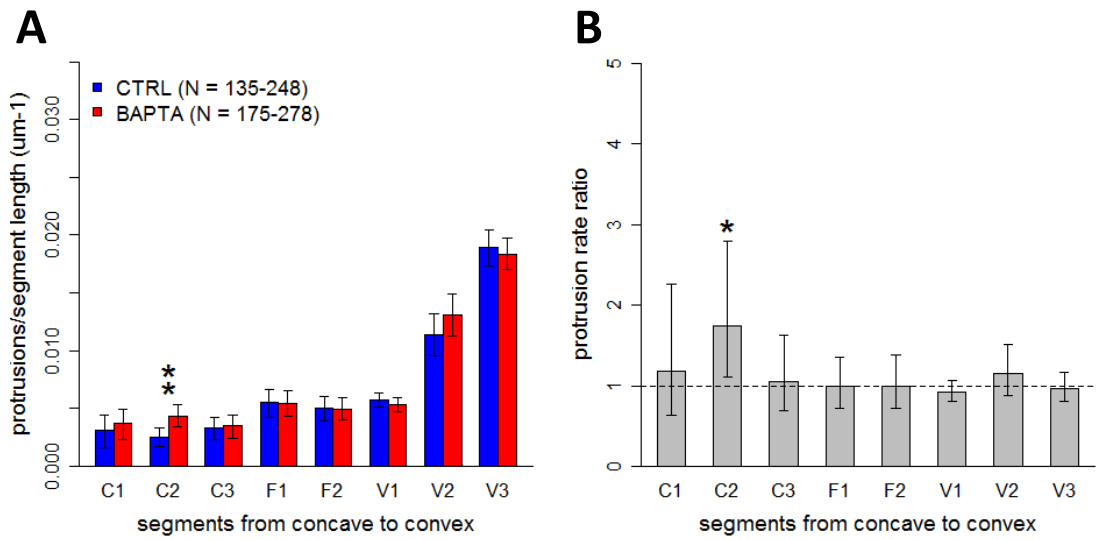

Figure 6.5: **Protrusion rates with BAPTA-AM treatment.** Protrusion rates were calculated by normalising counts of protrusions by segment length. (A) Protrusion rates (mean ± bootstrapped 95% CI) show a positive trend with curvature, with no trend of appreciable change in protrusion rate at concave or convex curvatures with BAPTA-AM treatment (stars indicate significant p-values from Mann-Whitney-Wilcoxon test; * < 0.05; ** < 0.01; *** < 0.001). (B) Protrusion rate ratios, 95% confidence intervals, and p-values (significance indicated by stars) were calculated using an exact Poisson rate ratio test. See Table 6.3 and Table 6.4.

6.5 Cytochalasin D

The Ionomycin experiment reported above seemed to suggest that protrusions at the three convex segments (V1, V2 and V3) were uniquely sensitive to inhibition via calcium influx. To confirm that the experimental system was sensitive to reductions in protrusion rate, especially at the concave (C) and flat (F) segments that have not shown any significant perturbation in the experiments reported above, Cytochalasin D was used to perturb the structural stability of the actin cytoskeleton. The expectation was that all protrusions would be severely inhibited or abolished, regardless of segment curvature.

Cytochalasin D is a fungal metabolite that has been in laboratory use for decades as a means to perturb actin dynamics. It was originally considered to act to depolymerise F-actin, but was subsequently found to inhibit both polymerisation and depolymerisation of actin, with unchanged levels of monomeric G-actin in treated cells. Cytochalasin D mainly acts by capping actin filaments at the fast-growing barbed ends, but has also been shown to inhibit the filament-severing action of cofilin, particularly at higher concentrations (Shoji et al., 2012).

Cells treated with Cytochalasin D typically develop drastically altered morphologies. Actin-myosin aggregates typically form due to the continued action of myosin, resulting in translocation of actin filaments with barbed ends that have been capped and blocked from extending (Verkhovsky et al., 1997). Confluent MDCK cells treated with lower concentrations of Cytochalasin D for an hour develop actin-myosin aggregates, and flatten out with the loss of the supportive actin belt (Stevenson and Begg, 1994), which reflects the requirement for continued actin polymerisation to maintain the actomyosin band at the epithelial zonula adherens (Leerberg et al., 2014).

Interestingly, disruption of transepithelial resistance (TER) in MDCK cells has been shown to be inversely proportional to Cytochalasin D concentration: TER dropped by almost 60% after treatment with $2\,\mu g\,mL^{-1}$ for one hour, whereas TER only dropped by 20% after treatment with $20\,\mu g\,mL^{-1}$, with the apical actin belt appearing intact in the latter condition (Stevenson and Begg, 1994). Given the more recent work on the mode of action of Cytochalasin D (Shoji et al., 2012), it could be argued that this dose-dependence is due to the increased inhibition of cofilin (and thus increased stability of F-actin at the zonula adherens) at higher concentrations of Cytochalasin D.

6.6 Inhibition of F-actin polymerisation

Micropatterned cells were treated with $0.1\,\mu g\,mL^{-1}$ Cytochalasin D ($0.2\,\mu M$), which has been shown to be sufficient to cause a reduction in stiffness along with cytoskeletal disorganisation in fibroblasts (Wakatsuki et al., 2001), including the appearance of actin-myosin aggregates as previously mentioned (Verkhovsky et al., 1997). As discussed above, this low concentration would be expected to act mainly through direct inhibition of F-actin polymerisation and depolymerisation by barbed end capping; cofilin inhibition is arguably unlikely to play a significant role in the results.

Cytochalasin D caused the expected drastic cytoskeletal alterations, with dense bead-like aggregates of F-actin accumulating at cell boundaries (see Fig. 6.6). The cell densities of scaffolds in both the control and treated micropatterns were noticeably lower than in the previous experiments, despite the seeding density being constant between experiments. This was attributed to the apparent degradation of the adhesion-resistant substrate: many micropatterns were overgrown by cells, and there were significant numbers of adherent cells on the substrate between micropatterns. As the reduced cell density was common to both conditions, they were con-

sidered comparable, and an analysis was conducted on segments that conformed to the micropatterns.

Unexpectedly, while Cytochalasin D treatment did severely inhibit protrusions at all flat (F) and concave (C) segments, it failed to alter the protrusion rates at the two convex segments with the highest curvature (V2 and V3; see Table 6.5, Table 6.6 and Fig. 6.7). These protrusions superficially resembled normal lamellipodia, with faint, homogeneous F-actin staining (see Fig. 6.8). Although the nonadhesive substrate had apparently undergone some degradation prior to use, resulting in some cells adhering outside the micropatterns (as can be seen in the example in Fig. 6.8B and F), this did not seem to explain the anomalous protrusions. Given that the Cytochalasin D treatment effectively abolished protrusions at all other segments, while the protrusion rates at V2 and V3 seem unchanged compared to the control, it appears possible that Cytochalasin D resistance is a characteristic of a subset of protrusions which are promoted by convex curvature.

Table 6.5: **Protrusion rates under Cytochalasin D treatment.** Protrusions from N segments of untreated (-) and treated (+) micropatterns were counted, and counts were normalised using median segment length to give protrusion rates in units of μm^{-1}. See Fig. 6.7A.

Segment	Cytochalasin D	N	Mean	95% CIL[a]	95% CIU[a]	SEM[b]
C1	(-)	87	0.0047	0.0015	0.0073	0.0014
C1	(+)	75	0.0013	-0.0004	0.0025	0.0007
C2	(-)	92	0.0029	0.0018	0.0039	0.0006
C2	(+)	83	0.0011	0.0003	0.0019	0.0004
C3	(-)	86	0.0048	0.0033	0.0061	0.0007
C3	(+)	82	0.0004	-0.0001	0.0009	0.0003
F1	(-)	80	0.0049	0.0034	0.0064	0.0008
F1	(+)	79	0.0006	-0.0001	0.0011	0.0003
F2	(-)	90	0.0065	0.0047	0.0082	0.0009
F2	(+)	75	0.0016	0.0005	0.0026	0.0005
V1	(-)	49	0.0101	0.0084	0.0115	0.0008
V1	(+)	37	0.0032	0.0020	0.0043	0.0006
V2	(-)	87	0.0173	0.0140	0.0205	0.0018
V2	(+)	78	0.0167	0.0134	0.0200	0.0017
V3	(-)	88	0.0203	0.0176	0.0232	0.0014
V3	(+)	72	0.0185	0.0154	0.0218	0.0016

[a] Upper / Lower 95% confidence limits for mean protrusion rates, calculated using bootstrapping. [b] Standard error of the mean.

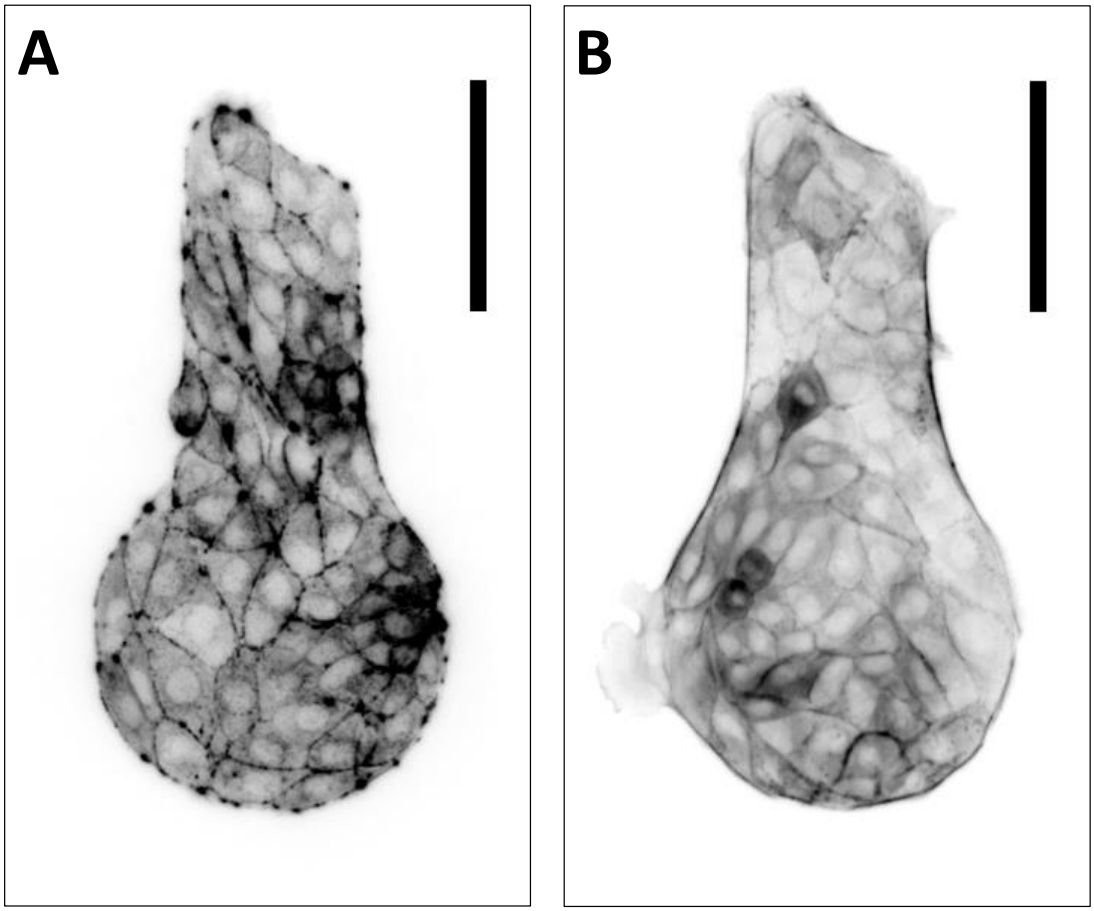

Figure 6.6: **Cytochalasin D-treated vs control micropatterns.** Representative micropatterned cells treated with (A) and without (B) 0.1 $\mu g\,mL^{-1}$ Cytochalasin D, and stained with FITC-phalloidin. The Cytochalasin D-treated cells (A) show the expected disruption in the actin cytoskeleton, with dense clumps of actin showing up as strongly-stained regions at the borders of cells. Unexpectedly, normal-looking lamellipodia at the most convex segments were common (see Fig. 6.8), suggesting that protrusions at these regions were somehow protected from the effects of Cytochalasin D. A 100 μm scale bar is shown at the top right of each panel.

Table 6.6: **Change in protrusion rates with Cytochalasin D treatment.** Untreated and treated segments were compared. Differences and ratios of mean protrusion rates (from Table 6.5) between conditions are given, along with the results of the Mann-Whitney-Wilcoxon and exact Poisson rate ratio tests. See Fig. 6.7B.

Segments	Diff.	MW p-value[a]	Ratio	95% CIL[b]	95% CIU[b]	RR p-value[c]
C1	-0.0035	0.0497*	0.27	0.05	0.97	0.0443*
C2	-0.0018	0.0228*	0.39	0.14	0.96	0.0377*
C3	-0.0044	0.0000***	0.09	0.02	0.29	0.0000***
F1	-0.0042	0.0000***	0.13	0.04	0.33	0.0000***
F2	-0.0049	0.0000***	0.25	0.11	0.50	0.0000***
V1	-0.0069	0.0000***	0.31	0.21	0.45	0.0000***
V2	-0.0006	0.8950	0.97	0.64	1.46	0.9533
V3	-0.0018	0.3928	0.91	0.65	1.26	0.6149

[a] Mann-Whitney-Wilcoxon test p-value. [b] Upper / Lower 95% confidence limits for the ratio of mean protrusion rates, calculated using an exact Poisson rate ratio test. [c] Exact Poisson rate ratio test p-value. Asterisks highlight significance (* < 0.05; ** < 0.01; *** < 0.001).

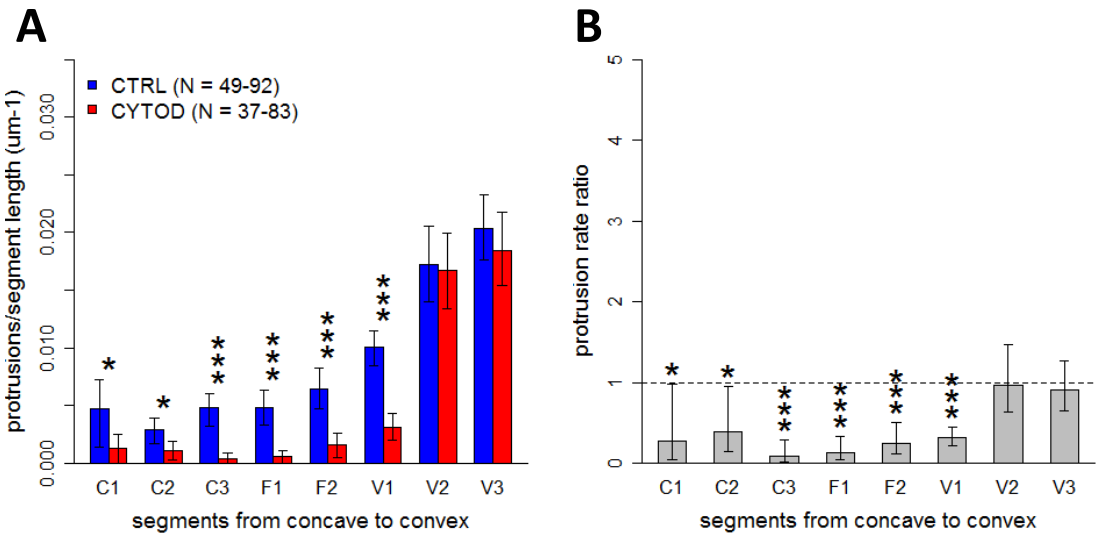

Figure 6.7: **Protrusion rates with Cytochalasin D treatment.** Protrusion rates were calculated by normalising counts of protrusions by segment length. (A) Protrusion rates (mean ± bootstrapped 95% CI) show a strong positive trend with curvature, with notable decreases in protrusion rate at all curvatures except the most convex with Cytochalasin D treatment (stars indicate significant p-values from Mann-Whitney-Wilcoxon test; * < 0.05; ** < 0.01; *** < 0.001). (B) Protrusion rate ratios, 95% confidence intervals, and p-values (significance indicated by stars) were calculated using an exact Poisson rate ratio test. See Table 6.5 and Table 6.6.

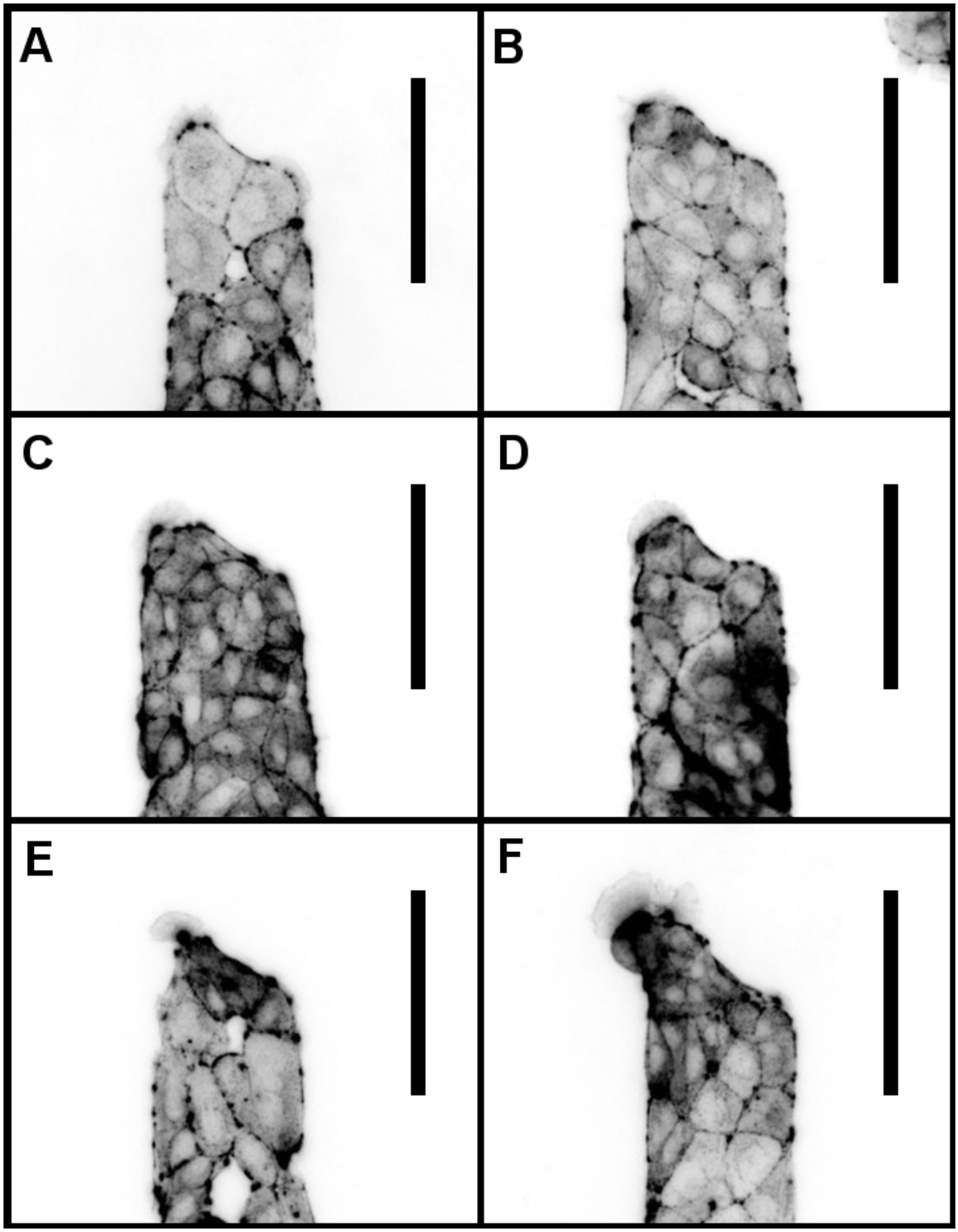

Figure 6.8: **Cytochalasin D-resistant protrusions at convex segments.** Representative micropatterned cells treated with 0.1 $\mu g\,mL^{-1}$ Cytochalasin D, and stained with FITC-phalloidin. Unexpectedly, normal-looking lamellipodia at the most convex segments were common, suggesting that protrusions at these regions were protected from the effects of Cytochalasin D. A 100 μm scale bar is shown at the top right of each panel.

6.7 Blebbistatin and Glycyl-H–1152

The results from treatment with Ionomycin could be reflective of relatively low myosin motor activity at the convex (V) segments, with calcium-mediated activation of myosin light chain kinase (MLCK) bringing the level of myosin activation more in line with the constitutively high levels characteristic of the other segments. The Cytochalasin D results could be interpreted as additional support for this hypothesis, as low levels of myosin activity locally might permit the protrusions to remain stable despite the inhibition of F-actin polymerisation, assuming low levels of filament depolymerisation and severing.

MLCK activation is associated with the protrusion-retraction cycles of lamellipodia, and is controlled by brief pulses of increased calcium concentration near the leading edge (Tsai and Meyer, 2012). The failure of BAPTA-AM treatment to increase protrusion rates at any segments suggested that a calcium-independent activator of myosin, possibly ROCK, could be responsible for the differential protrusion rates at different segments. By this logic, inhibition of myosin and ROCK activity should have similar outcomes: increasing protrusion rates at the flat and concave segments relative to the convex segments.

This speculation has some support in the literature: leader cells that arise during wound healing of epithelial sheets were originally characterised as having reduced RhoA GTPase activity, as expressing a constitutively-active RhoA mutant (presumably increasing the activity of the Rho effector ROCK) repressed leader cell formation, while inhibiting ROCK with Y–27632 induced all cells to take on leader characteristics (Omelchenko et al., 2003).

Early work by Parker et al. used 2,3-butanedione monoxime (BDM) to inhibit myosin, which abolished protrusions in single PDGF-stimulated fibroblasts constrained to square micropatterns. This was interpreted as evidence of a requirement for cellular traction forces to position focal adhesions and direct protrusions (Parker et al., 2002). However, BDM has subsequently been reported to have no effect on non-muscle myosins, and to instead act to inhibit protrusions by interfering with localisation of the branched actin nucleator Arp2/3 (Yarrow et al., 2003).

More recent work has used Blebbistatin to inhibit myosin activity, and has shown results that differ from Parker and colleagues' observation: increasing the size of lamellipodial protrusions while retaining the curvature-defined spatial organisation in micropatterned single cells (James et al., 2008); disrupting purse string cables at concave regions in favour of lamellipodia in wounded monolayers (Klarlund,

2012); and reducing the ability of collectives to migrate directionally in response to geometrical cues when released from micropatterns (Rausch et al., 2013).

Blebbistatin is a cell-permeable small molecule which was discovered in a screen for inhibitors of myosin IIA, and has been since found to also inhibit other class II myosins (including myosin IIB, with high potency), although not myosins from other classes (Limouze et al., 2004). It acts reversibly by stabilizing myosin in a transitional conformation prior to the power stroke (Allingham et al., 2005). Blebbistatin-bound myosin maintains a weak actin-binding capacity that is sufficient to tether actin filaments, but insufficient to either cross-link filaments into a rigid network, or to resist when filaments are tugged by uninhibited motor proteins (Sakamoto et al., 2005).

The Rho effector ROCK, which activates myosin by phosphorylating the regulatory myosin light chain (MLC), is commonly targeted using the inhibitor Y–27632, which generally has similar effects to Blebbistatin in reducing the collective sensitivity of migrating cells to geometrical cues (Kumar et al., 2011; Rausch et al., 2013). However, there are newer ROCK inhibitors available that have advantages over Y–27632. H–1152 and Glycyl-H–1152 have the same mechanism of action as the older drug (competition with ATP for a binding site on the target protein), but have significantly higher potency and specificity for ROCK. This is especially the case for the newest drug, Glycyl-H–1152 (Tamura et al., 2005).

6.8 Inhibition of acto-myosin contractility

Micropatterned cells treated with 25 μM Blebbistatin showed a tendency to lose the smooth border that typically characterises the periphery of untreated micropatterns (see Fig. 6.9), which can be interpreted as being due to a loss of tension in the peripheral actin cable with myosin inhibition. Stress fibres were rarely seen in either condition, presumably due to the limitation on area available per cell. As expected, treatment with Blebbistatin resulted in a trend of increases in protrusion rates at all segments, with convex (V) segments also showing increases (see Table 6.7, Table 6.8 and Fig. 6.10).

Treatment of micropatterned cells with 5 μM Glycyl-H–1152 was carried out in parallel with the Cytochalasin D experiment discussed in Section 18, using the micropatterns from the same batch, which subsequently were found to be significantly degraded. While the degraded micropatterns were frequently overgrown, and the average density of cells on each micropattern was noticeably reduced (presumably

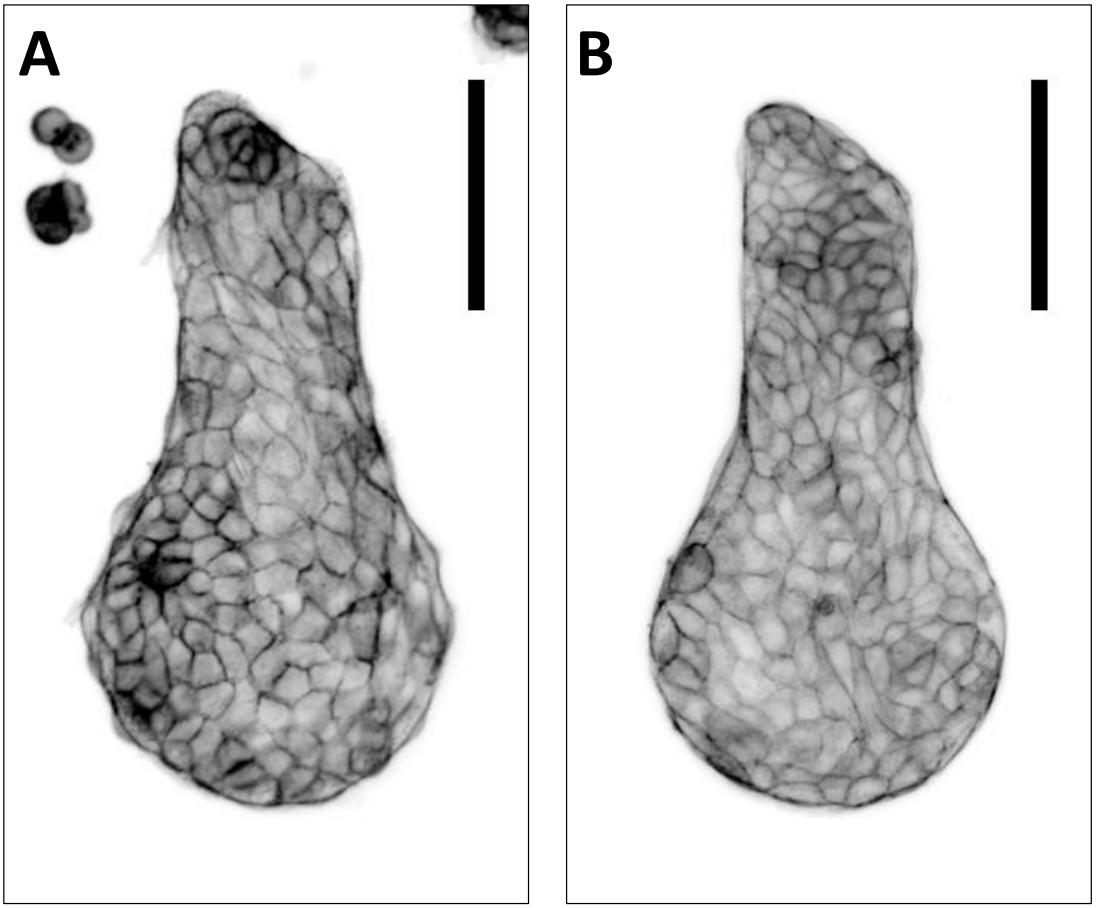

Figure 6.9: **Blebbistatin-treated vs control micropatterns.** Representative micropatterned cells treated with (A) and without (B) 25 μM (-)-Blebbistatin, and stained with FITC-phalloidin. The Blebbistatin-treated cells (A) show a typical loss of the smooth border seen in the untreated scaffold (B), along with an increase in protrusions. A 100 μm scale bar is shown at the top right of each panel.

Table 6.7: **Protrusion rates under Blebbistatin treatment.** Protrusions from N segments of untreated (-) and treated (+) micropatterns were counted, and counts were normalised using median segment length to give protrusion rates in units of μm^{-1}. See Fig. 6.10A.

Segment	Blebbistatin	N	Mean	95% CIL[a]	95% CIU[a]	SEM[b]
C1	(-)	193	0.0031	0.0018	0.0044	0.0007
C1	(+)	210	0.0033	0.0020	0.0045	0.0007
C2	(-)	167	0.0025	0.0017	0.0032	0.0004
C2	(+)	158	0.0042	0.0031	0.0053	0.0005
C3	(-)	159	0.0033	0.0024	0.0042	0.0005
C3	(+)	190	0.0035	0.0027	0.0044	0.0004
F1	(-)	135	0.0055	0.0044	0.0066	0.0006
F1	(+)	114	0.0072	0.0057	0.0087	0.0008
F2	(-)	165	0.0050	0.0039	0.0060	0.0006
F2	(+)	160	0.0068	0.0055	0.0080	0.0006
V1	(-)	213	0.0057	0.0051	0.0064	0.0003
V1	(+)	225	0.0071	0.0064	0.0077	0.0003
V2	(-)	241	0.0114	0.0098	0.0132	0.0009
V2	(+)	288	0.0178	0.0161	0.0195	0.0009
V3	(-)	248	0.0189	0.0173	0.0205	0.0008
V3	(+)	297	0.0224	0.0211	0.0237	0.0007

[a] Upper / Lower 95% confidence limits for mean protrusion rates, calculated using bootstrapping. [b] Standard error of the mean.

Table 6.8: **Change in protrusion rates with Blebbistatin treatment.** Untreated and treated segments were compared. Differences and ratios of mean protrusion rates (from Table 6.7) between conditions are given, along with the results of the Mann-Whitney-Wilcoxon and exact Poisson rate ratio tests. See Fig. 6.10B.

Segments	Diff.	MW p-value[a]	Ratio	95% CIL[b]	95% CIU[b]	RR p-value[c]
C1	0.0002	0.8349	1.06	0.55	2.08	0.9681
C2	0.0018	0.0153*	1.70	1.07	2.76	0.0241*
C3	0.0002	0.7052	1.07	0.71	1.63	0.8183
F1	0.0016	0.1726	1.29	0.94	1.80	0.1238
F2	0.0017	0.0517	1.35	0.97	1.88	0.0734
V1	0.0013	0.0028**	1.23	1.08	1.41	0.0018**
V2	0.0064	0.0000***	1.56	1.21	2.02	0.0004***
V3	0.0035	0.0012**	1.19	1.00	1.41	0.0494*

[a] Mann-Whitney-Wilcoxon test p-value. [b] Upper / Lower 95% confidence limits for the ratio of mean protrusion rates, calculated using an exact Poisson rate ratio test. [c] Exact Poisson rate ratio test p-value. Asterisks highlight significance (* < 0.05; ** < 0.01; *** < 0.001).

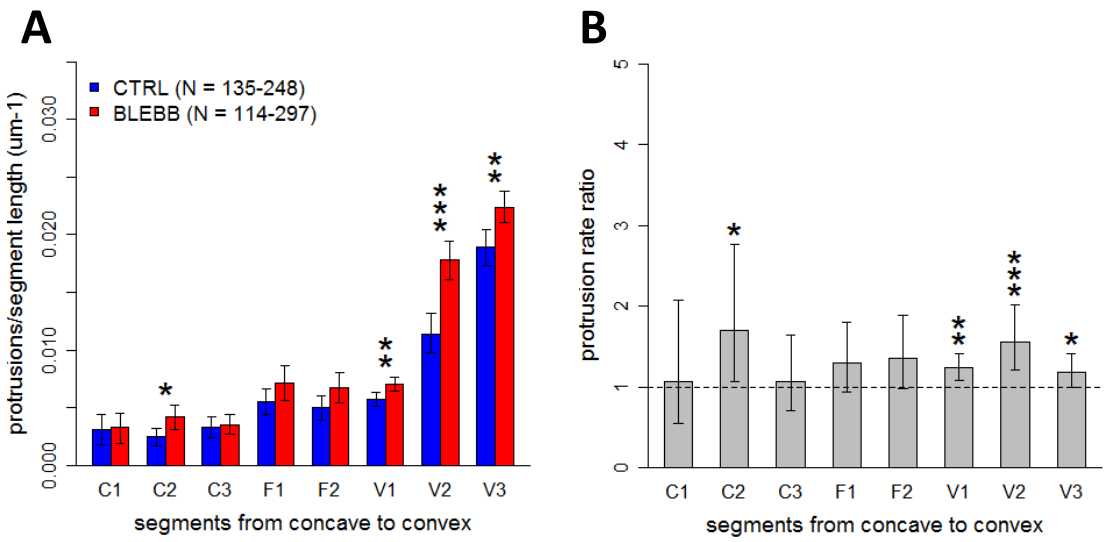

Figure 6.10: **Protrusion rates with Blebbistatin treatment.** Protrusion rates were calculated by normalising counts of protrusions by segment length. (A) Protrusion rates (mean ± bootstrapped 95% CI) show a strong positive trend with curvature, with a trend of increases in protrusion rate at the convex (V) segments with Blebbistatin treatment (stars indicate significant p-values from Mann-Whitney-Wilcoxon test; * < 0.05; ** < 0.01; *** < 0.001). (B) Protrusion rate ratios, 95% confidence intervals, and p-values (significance indicated by stars) were calculated using an exact Poisson rate ratio test. See Table 6.7 and Table 6.8.

due to cells being able to adhere elsewhere on the substrate), it was decided to analyse the segments that did conform to the micropattern.

While the peripheral actin cable was visibly reduced with Glycyl-H–1152 treatment, micropatterns did not tend to have the 'lumpy' appearance typical with Blebbistatin treatment (see Fig. 6.11). This may reflect both the presence of functional myosin in the cortex at the periphery, along with other myosin-activating kinases such as MLCK, as well as the far lower cell density than in micropatterns treated with Blebbistatin. Stress fibres were clearly abolished with Glycyl-H–1152 treatment, and immunofluorescence staining for active myosin II (using an antibody directed against MLC phosphorylated on serine 19, a target of ROCK kinase activity) showed a dramatic reduction in the level of phosphorylated myosin (see Fig. 6.12; note the use of a different micropatterned substrate batch).

The results of treatment with Glycyl-H–1152 were in line with the predictions: increases in protrusion rates at concave (C) and flat (F) segments, while the most convex segments (V2 and V3) were unaffected (see Table 6.9, Table 6.10 and Fig. 6.13). Despite the significant differences in cell density between the micropatterns used in this experiment, and those in the previous experiments, the control values look remarkably similar. While this would be expected to reflect an underestima-

tion of the 'true' per-cell protrusion rate on the part of the micropatterned cells treated with Glycyl-H–1152, it may reflect a mechanism for maintaining a constant leader initiation rate regardless of cell density. Further work will be necessary to test this, as will be discussed in the next chapter.

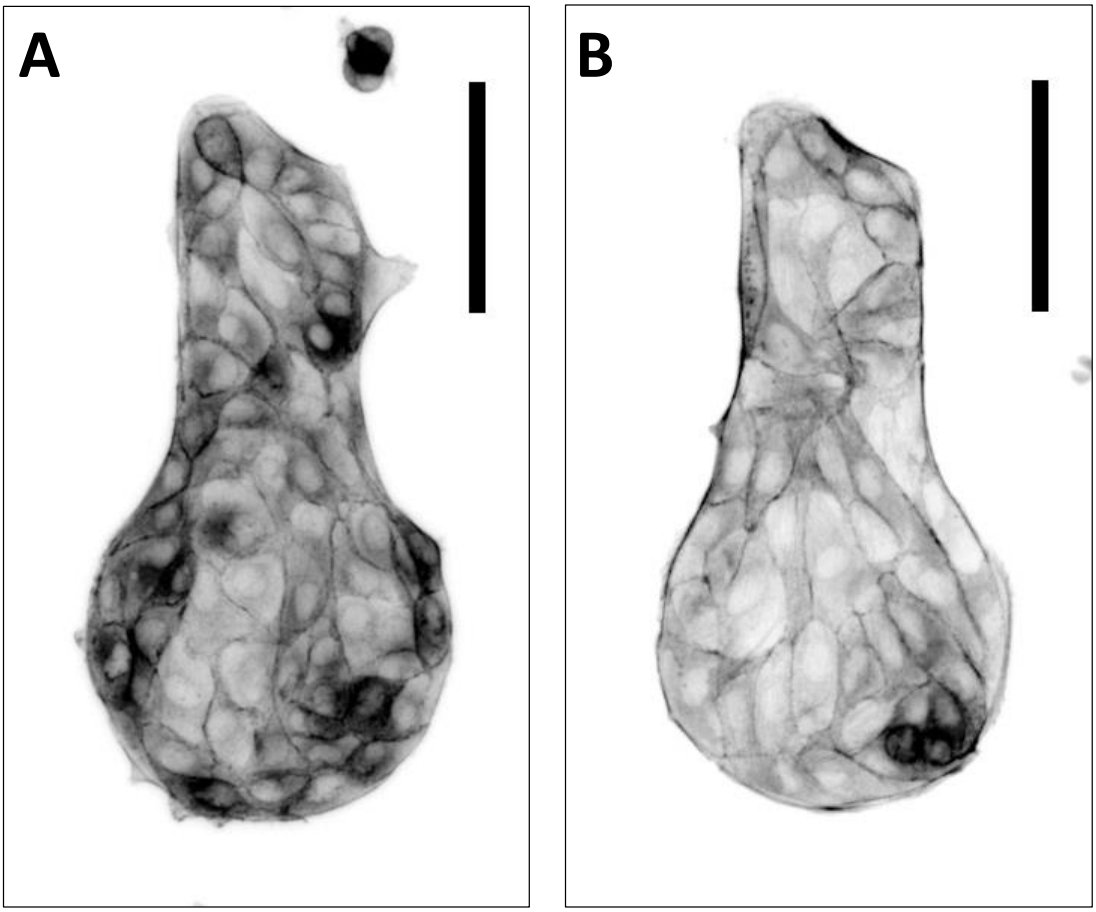

Figure 6.11: **Glycyl-H-1152-treated vs control micropatterns.** Representative micropatterned cells treated with (A) and without (B) 5 μM Glycyl-H-1152, and stained with FITC-phalloidin. Unlike Blebbistatin-treated micropatterns, there was no immediately obvious difference between treatments. However on closer inspection it can be seen that the peripheral actin cable has been reduced in the cell clusters treated with Glycyl-H-1152. A 100 μm scale bar is shown at the top right of each panel.

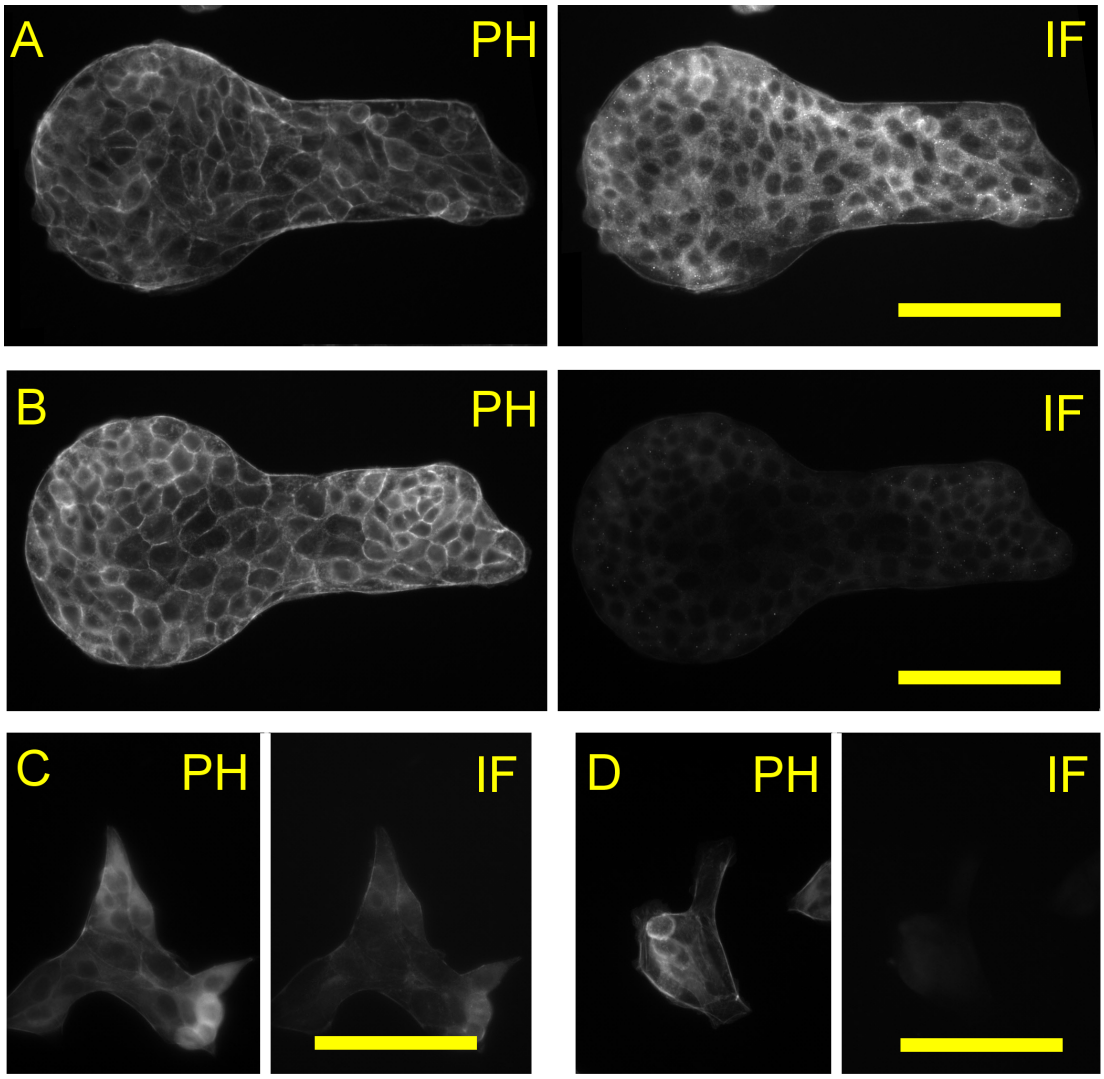

Figure 6.12: **Effect of Glycyl-H-1152 on MLC phosphorylation levels.** Immunofluorescence staining with an antibody against MLC(pSer19) was carried out on controls and micropatterns treated with Glycyl-H-1152. Panel A shows an untreated micropattern, with FITC-phalloidin staining (PH) shown on the left, and immunofluorescence (IF) on the right. Panel B shows a Glycyl-H-1152-treated micropattern, with a decrease in the intensity of the immunofluorescence signal indicating a reduction in phosphorylated MLC due to inhibition of ROCK by the drug. Stained unconstrained cells are shown for comparison, with (C) and without (D) the primary antibody. Note that these micropatterns were from a separate batch to those analysed for changes in protrusion rate. Scale bars show 100 µm.

Table 6.9: **Protrusion rates under Glycyl-H-1152 treatment.** Protrusions from N segments of untreated (-) and treated (+) micropatterns were counted, and counts were normalised using median segment length to give protrusion rates in units of μm^{-1}. See Fig. 6.13A.

Segment	G-H-1152	N	Mean	95% CIL[a]	95% CIU[a]	SEM[b]
C1	(-)	87	0.0047	0.0018	0.0073	0.0014
C1	(+)	222	0.0083	0.0064	0.0103	0.0010
C2	(-)	92	0.0029	0.0018	0.0041	0.0006
C2	(+)	243	0.0055	0.0046	0.0064	0.0004
C3	(-)	86	0.0048	0.0033	0.0062	0.0007
C3	(+)	268	0.0081	0.0070	0.0091	0.0005
F1	(-)	80	0.0049	0.0032	0.0062	0.0008
F1	(+)	229	0.0128	0.0113	0.0142	0.0007
F2	(-)	90	0.0065	0.0047	0.0082	0.0009
F2	(+)	231	0.0120	0.0107	0.0134	0.0007
V1	(-)	49	0.0101	0.0086	0.0115	0.0008
V1	(+)	215	0.0144	0.0134	0.0153	0.0005
V2	(-)	87	0.0173	0.0140	0.0208	0.0018
V2	(+)	229	0.0167	0.0150	0.0187	0.0010
V3	(-)	88	0.0203	0.0176	0.0232	0.0014
V3	(+)	243	0.0220	0.0201	0.0238	0.0009

[a] Upper / Lower 95% confidence limits for mean protrusion rates, calculated using bootstrapping. [b] Standard error of the mean.

Table 6.10: **Change in protrusion rates with Glycyl-H-1152 treatment.** Untreated and treated segments were compared. Differences and ratios of mean protrusion rates (from Table 6.9) between conditions are given, along with the results of the Mann-Whitney-Wilcoxon and exact Poisson rate ratio tests. See Fig. 6.13B.

Segments	Diff.	MW p-value[a]	Ratio	95% CIL[b]	95% CIU[b]	RR p-value[c]
C1	0.0035	0.0284*	1.75	0.95	3.48	0.0785
C2	0.0026	0.0011**	1.89	1.16	3.23	0.0079**
C3	0.0033	0.0005***	1.69	1.17	2.52	0.0042**
F1	0.0079	0.0000***	2.62	1.87	3.77	0.0000***
F2	0.0056	0.0000***	1.86	1.36	2.59	0.0000***
V1	0.0043	0.0001***	1.43	1.21	1.70	0.0000***
V2	-0.0006	0.9474	0.97	0.70	1.36	0.8943
V3	0.0017	0.3706	1.08	0.85	1.39	0.5589

[a] Mann-Whitney-Wilcoxon test p-value. [b] Upper / Lower 95% confidence limits for the ratio of mean protrusion rates, calculated using an exact Poisson rate ratio test. [c] Exact Poisson rate ratio test p-value. Asterisks highlight significance (* < 0.05; ** < 0.01; *** < 0.001).

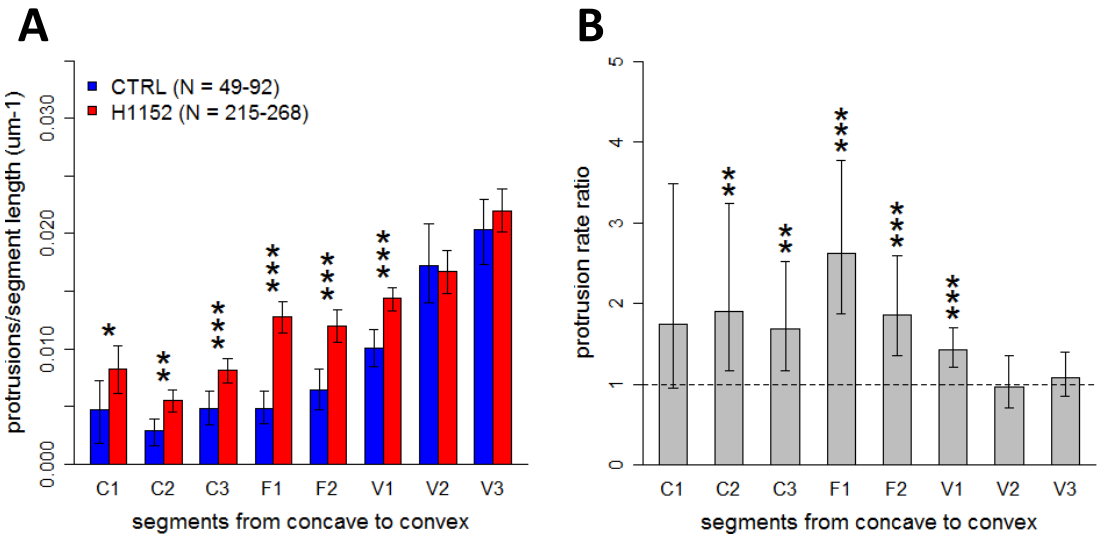

Figure 6.13: **Protrusion rates with Glycyl-H-1152 treatment.** Protrusion rates were calculated by normalising counts of protrusions by segment length. (A) Protrusion rates (mean ± bootstrapped 95% CI) show a positive trend with curvature, with significant increases in protrusion rate at all segments except the most convex (V2 and V3) with Glycyl-H-1152 treatment (stars indicate significant p-values from Mann-Whitney-Wilcoxon test; * < 0.05; ** < 0.01; *** < 0.001). (B) Protrusion rate ratios, 95% confidence intervals, and p-values (significance indicated by stars) were calculated using an exact Poisson rate ratio test. See Table 6.9 and Table 6.10.

Chapter 7

DISCUSSION OF RESULTS

7.1 Perturbation of protrusion rates

In the course of this work, the localisation of protrusions extending from the periphery of multicellular epithelial clusters of defined geometry has been characterised and perturbed. These protrusions were visualised using fluorescent conjugates of the F-actin-binding peptides phalloidin and Lifeact, the latter of which is a genetically encoded probe that permits live imaging of actin cytoskeleton dynamics.

Protrusions were observed to match the dynamic, feathery appearance typical of lamellipodia, and more condensed, narrow shapes that were observed in live imaging to be transitional phases during lamellipodial dynamics. Despite the observed dynamism, some protrusions were observed to remain relatively stable for extended periods (over thirty minutes during live imaging with images captured every two minutes). Analysis of large numbers of fixed samples confirmed the reports in the literature of a preferential localisation of protrusions at convex edges.

One interesting hypothesis for the control of protrusion localisation by multicellular geometry was suggested in a report by Nelson and colleagues, in which they gave theoretical and experimental evidence in support of gradients of autocrine inhibitory cytokines being shaped purely by the geometry of the secreting cell collective (Nelson et al., 2006). As that work involved three-dimensional collectives constrained by a matrix that could be expected to have significant effects on cytokine diffusion and gradient establishment, while the experimental system used in this work is effectively two-dimensional, and lacking a matrix overlay, it must be noted that there are considerable differences in context. Use of a low-shear perfusion culture system to disrupt the putative gradient did not support a role for this hypothesised mechanism playing a significant role in this system.

Atomic Force Microscopy (AFM) data from collaborators showed that a region with a height between 500–900nm at periphery of cells, corresponding to the lamella (Burnette et al., 2014; Davies, 2013), has a high Elastic Modulus (resistance to deformation) at convex curves, and a lower Elastic Modulus at concave and flat segments, with flat segments having the lowest Elastic Modulus. Given the known importance of cellular prestress in effective transduction of mechanical signals (Ingber et al., 2014), this information served as motivation to examine the role of known mechanotransduction-related components in determining the position of protrusions with respect to peripheral curvature.

As a number of mechanosensitive calcium channels are suggested to influence cytoskeletal organisation in response to mechanical signals, and calcium signalling is known to act in ways that could promote or inhibit protrusion formation (via actin polymerisation and myosin activation, respectively), two opposing hypotheses were initially considered for testing: "calcium influx at convex curves is responsible for promoting protrusions locally"; and alternatively, "calcium influx at concave curves is responsible for inhibiting protrusions locally". A slight modification to the latter model included a global effect of calcium influx at concave curves: a local increase in myosin activation would be expected to transmit increased force to the flanking focal adhesions, which would be expected to result in increased protrusion rates at those points.

Treatment of micropatterned cells with the ionophore Ionomycin to raise intracellular Ca^{2+} levels, and with the intracellular Ca^{2+} chelator BAPTA-AM, did not support any of the hypotheses advanced above. While Ionomycin inhibited protrusions at the convex segments, supporting a potential role for calcium influx at concave segments under normal conditions, BAPTA-AM did not cause the expected increase in protrusions at the concave segments. However, these results could support an alternative model involving a role for calcium oscillations at convex regions, as discussed in Section 7.2.

Cytochalasin D treatment was chosen as a positive control of protrusion perturbation, given its known action of inhibiting actin polymerisation, and in the expectation that unopposed cofilin and myosin activity would together act to abolish all actin-based protrusions. Unexpectedly, while the protrusions at the other segments were strongly inhibited, the protrusions at the most convex curves were found to be highly resistant to Cytochalasin D treatment. This suggests that these protrusions represent a unique subset, potentially characterised by differential regulation of myosin and cofilin activity. There is some support in the literature for this speculation, as is discussed in Section 7.3.

The specific myosin II inhibitor Blebbistatin, and the specific ROCK inhibitor Glycyl-H–1152 (which would be expected to have several effects including the reduction of myosin II activity), were used to test the hypothesis of a role for differential myosin activity at different curvatures. These results are discussed in Section 7.4.

7.2 Sensitivity to calcium influx

Several simple models involving a role for differential calcium influx in determining the placement of protrusions with respect to peripheral curvature were initially considered. As it has been reported that MDCK monolayer wound healing is unaffected by drugs that increase or decrease intracellular calcium levels (Farooqui and Fenteany, 2005), and similarly that lamellipodia-mediated gap closure in endothelial monolayers is inhibited by, but otherwise independent of, intracellular calcium fluctuations (Martinelli et al., 2013), it was considered unsurprising that the data from experiments using Ionomycin and BAPTA-AM did not support any of the proposed models.

However, the proposed models did not take into account the dynamic nature of calcium signalling; failing to consider a potential role for calcium oscillations. In recent years, prolonged mechanical stretch has been shown to induce calcium oscillations in mesenchymal stem cells, with the calcium influx starting proximal to the source of the tension and propagating throughout the cell body (Kim et al., 2014). Local pulses of calcium influx in the lamellipodia of migrating cells have been shown to play an integral role in the protrusion-retraction cycle, which includes adhesion reinforcement, through activation of myosin II (Tsai and Meyer, 2012).

It is tempting to speculate on a role for propagating calcium waves in cells at convex curves; perhaps resulting in differential myosin activation in the cortex, distal to the original site of influx. This site would likely be at the periphery of cells at convex regions (the most stretched, in terms of distortion from an ideal rounded shape, and reported to be the sites of highest traction), and would require a subsequent rapid reduction of local myosin activity to permit the protrusion phase of the cycle to continue, perhaps aided by pressure from the cortical contraction elsewhere.

The results of Ionomycin treatment partially support this model: inhibiting protrusions at the convex regions where cells might be expected to be experiencing stretch-induced calcium waves (blocking the cyclic reduction in local calcium levels, thus prolonging the retraction phase of the protrusion cycle). Ionomycin had

little effect on the concave and flat segments, which might suggest that cells at these segments have constitutively high myosin activity. This is supported by the reported role for MLCK activity in maintaining the peripheral actin cable that is typical of these segments (Russo et al., 2005).

While the lack of effect of BAPTA-AM could be interpreted as arguing against the validity of this model, any interpretations based on the use of this drug must be made with caution. While it is an efficient buffer of cytosolic calcium fluctuations, it has been shown to have little capacity to reduce calcium levels near the plasma membrane (in the cortex) (Basset et al., 2004). Perhaps more concerning: two seldom-cited studies have warned that the effect of BAPTA-AM on the cell is not limited to sequestration of intracellular Ca^{2+}, and that the molecule also has impacts on the cytoskeleton that are Ca^{2+}-independent (Furuta et al., 2009; Saoudi et al., 2004).

These unanticipated effects are cell-type and cell-state dependent. Saoudi et al. reported disassembly of the microtubule cytoskeleton in fibroblasts at doses as low as 10 μM, and also observed effects on the actin cytoskeleton (Saoudi et al., 2004). This provides an alternative explanation for the observation made by Parker and colleagues, who reported that lamellipodia from fibroblasts on square micropatterns were abolished on exposure to BAPTA-AM, and concluded that this was support for a role for contractility in positioning protrusions (Parker et al., 2002). Furuta et al. also showed that BAPTA-AM disassembled both the actin and microtubule cytoskeletons, but found that the actin cytoskeleton in differentiated adipocytes was resistant to BAPTA-AM, while microtubules in undifferentiated adipocytes appeared unaffected by BAPTA-AM (Furuta et al., 2009; Saoudi et al., 2004).

Given the potential for cell type-dependent effects on the stability of the microtubule cytoskeleton, the fact that treatment with BAPTA-AM had no apparent effect raises some additional speculation. Work on the mechanism of action of BAPTA-AM has determined that the drug does not actively depolymerise microtubules (Furuta et al., 2009), and that inhibiting microtubule dynamics in vivo prevents disassembly on BAPTA-AM exposure (Saoudi et al., 2004). This suggests that microtubules are stabilised in micropatterned MDCK II cells, which may play a role in explaining the Cytochalasin D resistance observed in protrusions at the most convex curvatures.

7.3 Protrusions at highly convex curvatures

Treatment of the micropatterned cells with the actin-capping drug Cytochalasin D unexpectedly revealed that the protrusions from the two most convex segments (V2 and V3) were resistant to treatment, unlike protrusions at the other segments. It was considered that these protrusions might represent artifacts such as retraction fibres, given that the cells at those points could be expected to experience significant forces directed towards the collective. However, given the increase in contractility with Ionomycin treatment, if these protrusions were retraction fibres left behind by the contracting collective, the protrusion rates should have increased with treatment. On the contrary, the protrusion rates of segments V2 and V3 decreased with Ionomycin treatment, along with that of V1.

It was observed by collaborators that the lamella region of cells at segments V2 and V3 had Elastic Modulus values that were significantly higher than at other segments, which suggests a possible role for a tropomyosin isoform in defining the characteristics of these protrusions. Some isoforms, such as Tpm3.1, have been observed to increase cellular stiffness through activation of myosin, and Tpm3.1 has also been shown to protect F-actin from disruption by Cytochalasin D (Jalilian et al., 2015). Similarly, tropomyosins have been shown to protect F-actin in the lamella from the severing activity of cofilin (Gupton et al., 2005), which is significant given that the concentration of Cytochalasin D used in this study was too low to inhibit the action of cofilin (Shoji et al., 2012).

The classical view of a lamellipodia includes a narrow rim of rapidly polymerising branched actin of only a few micrometers wide, which engages with the more ordered lamella behind it, which typically is up to about 15 μm wide. The former excludes tropomyosin, and is sensitive to Cytochalasin D. These two zones converge at a band characterised by growing adhesions (Gupton et al., 2005). While these dimensions correspond to protrusions observed extending from the periphery of the micropatterns (up to approximately 20 μm), in the context of the nonadhesive substrate the advance of lamellipodia would be expected to be unstable (Bailly et al., 1998).

One possibility for stable protrusion extension in the absence of sufficient adhesion involves hydrostatic pressure from the contractile cortex to drive the leading edge forward (Gupton et al., 2005). Another potentially complementary mechanism might involve the contraction of transverse arcs anchored to the edge of the micropattern at each end, and running up across the linear array of actin filaments that make up the lamella proper. It has been reported that this architecture is re-

sponsible for the typical flatness of the lamella compared to the rest of the cell body, and it was shown that expression of the myosin IIA isoform in COS–7 cells (a 'short lamella' cell type) was sufficient to increase the length of the lamella region from approximately 5 μm to 18 μm (Burnette et al., 2014). In support of these mechanisms, it has been demonstrated that increasing the contractility of keratinocytes migrating along a series of micropatterns increases the size of the nonadhesive gap they are able to cross (Okeyo et al., 2011).

The presumed stability of the microtubule network, given the lack of effect of BAPTA-AM treatment as discussed in Section 7.2, is suggestive of a role for microtubules in forming the V2 and V3 protrusions. One of the roles of paxillin, the scaffolding protein associated with focal adhesions under high tension at the corners of micropatterns (Sero et al., 2012), is to inhibit HDAC6, preventing it from deacetylating and destabilising microtubules (Deakin and Turner, 2014). Endothelial cells have been shown to switch to a dependence on microtubule-based protrusions when transferred from a rigid 2D substrate to a soft 3D collagen gel, and require microtubules to protrude significantly into the gel (Martins and Kolega, 2012), which could be considered somewhat analogous to protruding across the surface of the passivated substrate.

While it is interesting to speculate on the nature of the V2 and V3 protrusions, and their relationship to protrusions in other contexts, further study of the ultrastructure and dynamics of these protrusions, along with more carefully chosen drugs, are necessary to test the hypotheses suggested above.

7.4 Differential myosin activity hypothesis

Micropatterned cells were treated with the myosin inhibitor Blebbistatin, and the specific ROCK inhibitor Glycyl-H–1152, with the aim of testing the hypothesis that the differential protrusion rates in response to curvature were due to myosin activity being limited at convex (V) segments, and relatively elevated at the flat (F) and concave (C) segments, the latter potentially through the action of ROCK. This hypothesis was provoked by the observation that treatment with Ionomycin, which would be expected to increase contractility through the calcium-activated kinase MLCK, only had a significant inhibitory effects on protrusions at the convex (V) segments; suggesting that myosin was already activated at a high level elsewhere along the periphery.

Although purse string closure has been reported to depend on MLCK activity (Russo

et al., 2005), there is some support for ROCK-mediated control of myosin activity at the periphery of the micropatterns, where an analogous structure can be seen to form. The GTPase RhoA has been found to localise along the 'pluricellular actomyosin cable' that borders collectively migrating MDCK cells, and treatment with the ROCK inhibitor Y–27632 was shown to dramatically change the force profile of the collective (Reffay et al., 2014).

A role for differential myosin activity in the curvature-protrusion relationship has support in the literature, in studies of 3D single endothelial cell branching. One study determined that branching increased with Blebbistatin treatment or ROCK inhibition, indicating a role for ROCK in activating myosin to prevent additional branching, and additionally observed that myosin was displaced from the cortex prior to initiation of a new protrusion, suggesting an additional layer of regulation (Fischer et al., 2009). A similar study using 3D micropatterned cells observed that myosin cyclical cortical association was affected by curvature, preferentially associating with regions of low and negative curvature, away from the tips of protrusions. This led the authors to suggest a feedback loop whereby myosin acts to minimise curvature, and oppose branching (Elliott et al., 2015).

The results of ROCK inhibition with Glycyl-H–1152 supported a role for differential myosin activity, as protrusion rates at the concave and flat segments increased significantly with treatment, while the two most convex segments (V2 and V3) were unaffected. This supports a model where ROCK maintains high levels of myosin activity at the cortex where the periphery has a low or negative curvature, limiting protrusions by a combination of sequestration of actin monomers (Lomakin et al., 2015), and retraction of protrusions (Lou et al., 2015).

Similarly, the results of Blebbistatin treatment also supported this model; there was a trend, if somewhat attenuated, of increases in protrusion rates globally. The fact that the protrusion rates at segments V2 and V3 show significant increases suggests that myosin is not completely inhibited at the most convex curves. It seems likely that myosin acts in a cyclical way at these segments, perhaps mediated by calcium oscillations as discussed in Section 7.2, with myosin inhibition trapping the retraction-protrusion cycle in the 'protrude' stage (in comparison to Ionomycin treatment, which acts via MLCK to trap the cycle in 'retract'). The relatively weak effect of Blebbistatin treatment, compared to Glycyl-H–1152, may be due to the higher cell density of the micropatterns used in the former experiment, as discussed further in Section 7.5.

However, there may be another contributing factor to the relatively weak effect of

Blebbistatin treatment on the flat (F) and concave (C) segments. Treatment of single cells micropatterned in dumbbell shapes with Blebbistatin has been observed to broaden the distribution of lamellipodia at the periphery, but not to disrupt the preferential distribution entirely: lamellipodia were still restricted from the concave regions (James et al., 2008). Blebbistatin treatment reduces tension in the actin cytoskeleton by inhibiting myosin activity, but fails to abolish stress fibers to the same extent as ROCK inhibition, in part because the latter also results in an increase in active actin-severing cofilin (Watanabe et al., 2007). As it has been hypothesised that sequestering actin monomers is one of the primary ways that stress fibres are antagonistic to actin-based protrusions (Lomakin et al., 2015), this may partly explain the stronger effect of Glycyl-H–1152 on concave and flat segments, and may be an interesting line for further study.

While the results discussed above are suggestive of a role for differential myosin activity in generating the curvature-protrusion relationship seen in micropatterned cells in 2D, and along with some recent support in the literature (Elliott et al., 2015; Fischer et al., 2009), further work must be done to confirm this conclusion. Determination of the potential involvement of other mediators of actin cytoskeleton dynamics, such as cofilin and other actin-severing proteins, would also be of interest. However, the pathways involved in translating curvature cues to effectors such as these have yet to be determined, although it seems clear that mechanotransduction is involved. One speculative model is discussed in Section 7.5.

7.5 Spreading and contact angle

As was discussed in Section 4.5, normalising segment protrusion counts by segment length instead of by cell number was a practical but problematic choice. However, even normalising by cell numbers instead of by length would not be appropriate in this case, as the significant differences in cell density between the experiments might be expected to have an effect on the responsiveness of the cells to the drug treatments. One relatively simple solution would be to count the total number of cells (as DAPI-stained nuclei) in each micropattern analysed, and group the data to compare like with like.

Clear separation and comparison of micropatterned cells by cell density may be of value in of itself, as it may shed more light on the relationship between curvature and protrusion rate, including the suggestion (based on similar control protrusion rates for low and high density micropattern experiments) that leader cell initiation rate may be constant regardless of cell density. In considering how micropattern

cell density might affect the protrusion rate of micropatterned cells, the recent work describing cell spreading as a function of cell-substrate contact angle (Fouchard et al., 2014), as described in Section 2.1, is suggestive of a model that might explain the protrusion-curvature relationship.

When constrained on a small micropattern with a significant aspect ratio, the extent to which an isolated cell is permitted to spread will determine the contact angle between the cortex and the adhesive substrate. In an extreme case such as a narrow linear micropattern, the centre of the cell will 'overflow' on either side (Bailly et al., 1998), with a contact angle less than 90°, in a way that is analogous to a cell that is in the very early stages of spreading. In contrast, along the axis of the linear micropattern the cortex would be stretched and flattened close to the substrate, with a contact angle of far more than 90°.

Viewing mechanically coherent multicellular clusters as analogous to a single cell in terms of their intrinsic tendency to round up when released from the substrate, much like a droplet acting under the influence of surface tension, allows this view to be extended. The aspect ratio of a micropattern could be expected to have a differential effect on the cell-substrate contact angle at different positions around the periphery, with cells at the periphery at either end of the long axis being under more tension, with a large contact angle with the substrate, and cells along the periphery at either end of the short axis being more inclined to overflow from the micropattern (especially at higher cell densities), and thus having a contact angle less than 90° (see Fig. 7.1).

This is significant when viewed in terms of the effect of contact angle on the onset of cellular traction generation and focal adhesion maturation, with contact angles above 90° suggested to be necessary for the the cell cortex to efficiently exert force against the nascent adhesions at the periphery (Fouchard et al., 2014). This provides an appealingly mechanical model to explain the reported clustering of large focal adhesions at micropattern corners, and leads to a potential explanation for the placement of protrusions.

This model can be further extended from aspect ratio to curvature, and to unconstrained monolayers. The key is the degree to which force is efficiently exerted against adhesions in an inwards direction, normal to the periphery and parallel to the substrate. While it is less intuitive to view a large monolayer as having an intrinsic tendency to round up (the 'surface tension' view), the presence of a mechanically coherent contractile actin cable at the wounded edge (the purse string) suggests another approach.

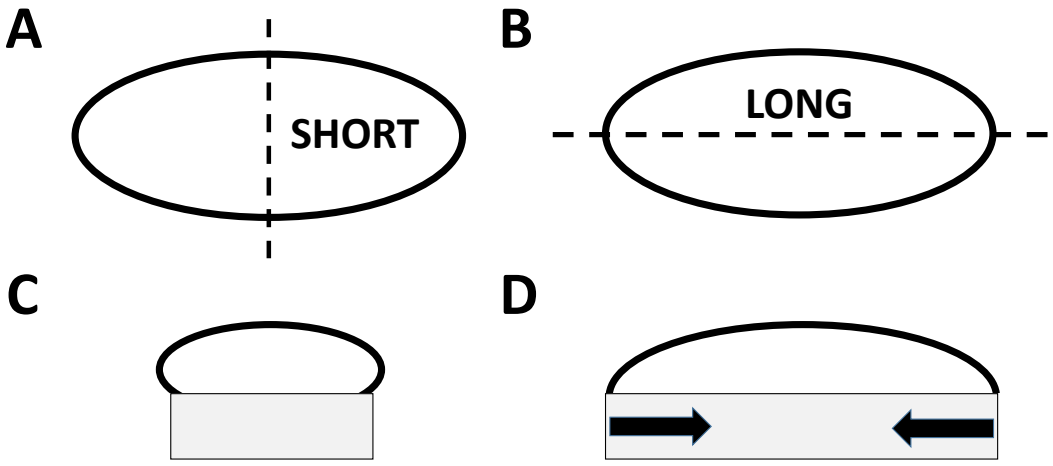

Figure 7.1: **Micropattern cell density effect on contact angle and traction forces.** When viewed in cross section along the short axis (A), cells constrained to the adhesive micropattern (C) (represented by the grey box) could be expected to 'overflow' the pattern slightly, which would be increasingly the case at higher cell densities. In contrast, when viewed in cross section along the long axis (B), cells would be expected to be more stretched, exerting higher forces against the substrate (D).

As surfaces under tension can be described by the relationship Pressure = Tension /Radius (Davies, 2013), it is clear that cells at the tips of convex curves (with a small Radius) will experience the largest force (Pressure) directed back to the monolayer. Conversely, cells at the base of a concave curve will experience a large force directed the other way, away from the monolayer, as they are pulled forward by the contracting purse string (see Fig. 7.2).

In the former case, the large inward force will have an effect on adhesions that is equivalent to that seen when a spreading cell's contact angle exceeds 90°: the adhesions will mature. In the latter case, the large outward-directed force can be expected to oppose the maturation of adhesions. This mimics the situation within a complete endothelial monolayer, where it is hypothesised that substrate adhesions in adjacent cells are under isometric tension due to the balanced forces applied by the cells on each other, with the loss of the cell-cell adhesions placing unbalanced force on the substrate adhesions, and thus triggering the formation of lamellipodia to seal the breach (Martinelli et al., 2013).

A link between force applied to adhesions, and protrusions, is suggested in part by the observation that the multifunctional scaffolding protein paxillin is required to position lamellipodia to the corners of micropatterns (Sero et al., 2012). Paxillin is recruited to focal adhesions in response to applied force (Pasapera et al., 2010), and is essential for durotaxis (Plotnikov and Waterman, 2013), suggesting

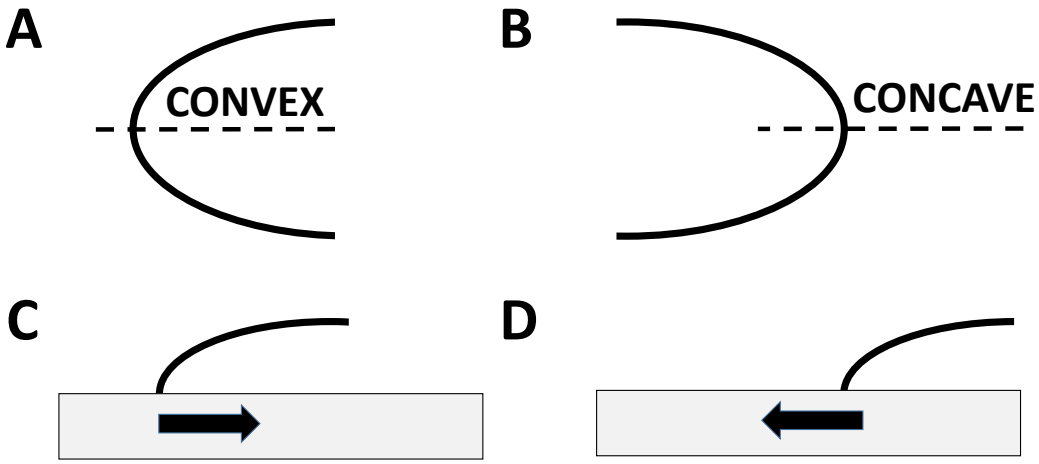

Figure 7.2: **Curvature effect on traction forces.** Micropatterned or unconstrained epithelial cells at the tip of a convex curve (A), would be expected to experience large forces against adhesions directed back into the monolayer (C), in part due to the contraction of the purse string that forms at the edge of monolayers. In contrast, cells at the base of a concave curve (B), would experience forces against adhesions directed the other way (D), also due to contraction of the purse string.

it may promote directed migration in response to the force asymmetries inherent in curvature and aspect ratio. In addition, as tension results in fibronectin fibrillogenesis, providing more substrate for integrin binding (Ingber et al., 2014), and fibronectin has been shown to be preferentially assembled in fibrils at the corners of micropatterns (Parker et al., 2002), it is possible that at least one feedback loop of this nature is operating.

In the context of multicellular collectives, this asymmetry could bias the competition for the 'leader' role, with cells elsewhere along the periphery subsequently falling into follower roles, with protrusions reorienting away from the periphery and extending (cryptically, under their neighbours) in the direction of the leader. This view has some support from simple observations of live imaged Lifeact-MDCK on micropatterns, and in the literature, where micropatterned cells have been observed to move in continuous flows, including in directions away from the micropattern periphery (Doxzen et al., 2013; Vedula et al., 2012).

This model suggests an additional reason for the surprisingly weak positive effect of Blebbistatin on the concave (C) and flat (F) segments, compared to the larger positive effect seen with Glycyl-H–1152. Cells at a lower density (as in the Glycyl-H–1152 experiment) would tend to be flattened against the substrate by virtue of the relatively large area available to each cell. In this case, a relaxation of the peripheral actin belt linking adherens junctions between cells within the cluster

would be expected to have relatively little effect on the contact angle with the substrate at the edge of the cluster.

In contrast, cells at higher densities (as in the Blebbistatin experiment) tend to have a more columnar appearance, in part due to the tension at the adherens junctions (Harris et al., 2014). In this case, relaxing the peripheral actin cable of cells within the cluster would be expected to result in an increased tendency to bulge over the boundary of the micropattern, which is reflected as a smaller contact angle, and a reduced tendency to protrude. In both cases, the contact angle at the convex curves would remain relatively large compared to the other segments, and even with myosin inhibited, adhesions at these segments would be expected to experience relatively more force (through residual myosin activity, and the 'surface tension' effect) as a consequence.

This negative effect on protrusion by Blebbistatin treatment of high density micropatterned cells would be in opposition to the positive effect of inhibition of myosin at the periphery, resulting in a relatively attenuated positive effect of treatment. In contrast, the low density micropatterns treated with Glycyl-H–1152 would be less affected by the relaxation of the peripheral actin belt, in addition to having an additional positive effect on protrusions through an increase in cofilin activity, as mentioned previously. This suggested reason for the attenuation of Blebbistatin's predicted effect is dependent on the artificial constraint of a micropattern, as the 'bulging' effect depends on the presence of a sharp boundary between adhesive and non-adhesive substrates.

This speculation will require experimental support, which could in part be gained by comparing the protrusion rates of treated and untreated micropatterns that have been segmented into groups based on cell density. In addition, the proposed involvements of paxillin and fibronectin in defining the response to curvature will require support, and it would be of interest to explore the potential role of paxillin in controlling the activation and localisation of myosin at convex curves, along with the known role of paxillin in stabilising microtubules (Deakin and Turner, 2014). Finally, the potential role of stretch-activated calcium oscillations (Kim et al., 2014) in the differential response to curvature has not been satisfactorily addressed, and deserves more attention given the many important roles calcium signalling is known to play in directed migration, including in the regulation of myosin localisation (Wei et al., 2012).

Chapter 8

CONCLUSIONS AND FUTURE DIRECTIONS

8.1 Curvature-protrusion relationship

The fundamental roles served by epithelia in barrier formation, along with efficient secretion and absorption, naturally require a responsiveness to geometry. Injured barriers must heal gaps efficiently, which may be best done through purse string closure, or else through the migration of streams of cells like fingers to interdigitate across the wound bed. Branching tissues must form coherently, maximising the surface area available for import and export of substances, while maintaining structural stability and adequate tube dimensions.

Much work has been done in recent years using single cells and multicellular clusters constrained to specific geometries using adhesion-permissive micropatterns. This system led to the initial observation that protrusions preferentially form at corners and convex curves (Parker et al., 2002). The correlation with the direction of migration when cells are released from the micropatterns, along with the tendency of some cells to form long, finger-like structures when migrating collectively, supported the hypothesis that a positive feedback loop was operating between curvature and protrusion (Davies, 2013; Mark et al., 2010).

Given the relationship between epithelial tissue geometry and function, especially in the branching organs, there is significant motivation to determine how epithelial cells collectively shape the structures they form. However, while the curvature-protrusion feedback model is intuitively appealing, and is sufficient in simulations to reproduce some of the shapes seen in collectively migrating epithelial sheets, it is agnostic as to the underlying mechanism. The mechanism by which epithelial

cells sense and respond to geometry remains an open question.

8.2 Control, context and consequences

A functional role for differential myosin motor localised activity in driving the response to differential curvature, as supported by this work and the recent literature (Elliott et al., 2015; Fischer et al., 2009), reinforces the picture of cells and multicellular structures as highly-structured mechanical entities, in addition to their biochemical complexity. Myosin activity acts to oppose lamellipodial protrusions, in part by associating with the constituent actin filaments and physically reeling the protrusion back towards the cell body, and the rate at which myosin accumulates behind the leading edge translates into how permissive the cortex is of large, stable protrusions (Lou et al., 2015).

While myosin localisation and activity may play a central role in the direction of protrusions, the question of control has yet to be answered. A recent report found that myosin is limited at regions of convex cortex in single endothelial cells, and suggested that the mechanism was due to the failure of myosin complexes to associate efficiently with actin at non-planar cortical regions (Elliott et al., 2015). However, a number of calcium effectors are known to regulate myosin activity and localisation, including S1004A, which inhibits the stable association of myosin with actin in protrusions (Wei et al., 2012). This suggests that calcium signalling should be considered as a potential part of the upstream pathway linking curvature to myosin.

Determining if there is a role for calcium signalling will require careful experimental design, and an appreciation of the dynamic nature of the signal. It is clear that in dissecting the involvement of particular pathways and components, it is necessary to use a wide range of targeting strategies: chemical and genetic; complete ablation, over-activation, and graded modulation (Davies, 2009). Drug results can be easily misinterpreted or even intrinsically misleading, depending on the level of knowledge of the mechanism of action. In the case of BAPTA-AM, for example, despite the publications warning about its calcium-independent effects on the actin and microtubule cytoskeletons (Furuta et al., 2009; Saoudi et al., 2004), its use is still being reported in the recent literature as unambiguously reflecting the effect of cytosolic calcium sequestration (Higashida et al., 2013).

The dynamics of the system at the cellular level should also be taken into account in future work, as it seems likely that the movements of cells collectively

and individually within the borders of the micropatterns impacts on the direction of visible protrusions. The report on the stochastic formation of leaders from a straight edge, which was the inspiration for the 'curvature-protrusion feedback' model (Mark et al., 2010), also included observations of the movements of individual cells within the monolayer. It was found that coordinated flows of cells moved through the monolayer in a way that gave an impression of turbulence, and that these flows occasionally delivered cells to the edge which then assumed the leader identity (Poujade et al., 2007). Constrained on a micropattern, it seems reasonable to consider whether the change in angle a cell is forced to take when moving around the inner edge may cause the flow to 'clog' at convex curves, with arrested cells taking up residence as leaders.

Speculation on how leader cells emerge from micropatterned clusters of cells may also be directed by the recent report linking the contact angle between the substrate and a spreading cell, with the onset of traction (Fouchard et al., 2014). In this view, micropatterns are seen as constraining cells (single cells and collectives) to a 'differentially spread' shape, with a consequential emergence of force asymmetry around the periphery. While this model can be extended to unconstrained monolayers with curved peripheries, it also raises some concerns about the use of micropatterns, as there seems to be potential for artifactual findings that do not translate to more natural systems, especially when using higher cell densities.

A potential case in point is the observation of highly stiff, stable, Cytochalasin D-resistant protrusions that were present at the most convex curvatures of the micropatterns. With that caution, it would be interesting to characterise these protrusions further, including the mechanics of their stable extension over the nonadhesive substrate, and to attempt to draw parallels with protrusions characteristic of other contexts, such as 3D invasion.

Ultimately, the focus of this work is the self-directed shaping of epithelial tissues, and the mechanisms involved in this process.

8.3 Toward synthetic morphogenesis

While micropatterned scaffolds have been invaluable in this and other works, the ultimate test of the architecture of a biological control system, and of our understanding of it, will involve re-creation. The term 'synthetic morphology' was coined to describe this approach (Davies, 2008), where the tools and philosophy of engineering are brought to bear on genetics ('synthetic biology'), and where the ulti-

mate aim is to generate tissues the same way living things do: through the unfolding of genetic programs within initially homogeneous cell populations.

While current approaches to tissue engineering tend to rely on external manipulations such as artificial scaffolds or techniques such as cell printing to position cells, synthetic morphology aims to control the cellular parameters that determine the ultimate outcome of morphogenesis. An attempt to simulate the curvature-protrusion feedback loop in a living system, by engineering a 'boring' cell line to express the necessary components, would make a great future challenge.

Bibliography

Abràmoff, M. D., Magalhães, P. J., and Ram, S. J. (2004). Image Processing with ImageJ. *Biophotonics International*, 11(7):36–42.

Allingham, J. S., Smith, R., and Rayment, I. (2005). The structural basis of blebbistatin inhibition and specificity for myosin II. *Nature Structural and Molecular Biology*, 12(4):378–9.

Bailly, M., Yan, L., Whitesides, G. M., Condeelis, J. S., and Segall, J. E. (1998). Regulation of protrusion shape and adhesion to the substratum during chemotactic responses of mammalian carcinoma cells. *Experimental Cell Research*, 241(2):285–99.

Basset, O., Boittin, F.-X., Dorchies, O. M., Chatton, J.-Y., van Breemen, C., and Ruegg, U. T. (2004). Involvement of inositol 1,4,5-trisphosphate in nicotinic calcium responses in dystrophic myotubes assessed by near-plasma membrane calcium measurement. *The Journal of Biological Chemistry*, 279(45):47092–100.

Belin, B. J., Goins, L. M., and Mullins, R. D. (2014). Comparative analysis of tools for live cell imaging of actin network architecture. *Bioarchitecture*, 4(6):189–202.

Bhadriraju, K., Yang, M., Alom Ruiz, S., Pirone, D., Tan, J., and Chen, C. S. (2007). Activation of ROCK by RhoA is regulated by cell adhesion, shape, and cytoskeletal tension. *Experimental Cell Research*, 313(16):3616–23.

Blagovic, K., Kim, L. Y., and Voldman, J. (2011). Microfluidic perfusion for regulating diffusible signaling in stem cells. *PloS ONE*, 6(8):e22892.

Borm, B., Requardt, R. P., Herzog, V., and Kirfel, G. (2005). Membrane ruffles in cell migration: Indicators of inefficient lamellipodia adhesion and compartments of actin filament reorganization. *Experimental Cell Research*, 302(1):83–95.

Brock, A., Chang, E., Ho, C.-C., LeDuc, P., Jiang, X., Whitesides, G. M., and Ingber, D. E. (2003). Geometric determinants of directional cell motility revealed using microcontact printing. *Langmuir*, 19(5):1611–7.

Burnette, D. T., Shao, L., Ott, C., Pasapera, A. M., Fischer, R. S., Baird, M. A., Der Loughian, C., Delanoe-Ayari, H., Paszek, M. J., Davidson, M. W., Betzig, E., and Lippincott-Schwartz, J. (2014). A contractile and counterbalancing adhesion system controls the 3D shape of crawling cells. *The Journal of Cell Biology*, 205(1):83–96.

Canty, A. and Ripley, B. (2016). *boot: Bootstrap R (S-Plus) Functions*. (R package version 1.3-18) [Computer software]. URL http://CRAN.R-project.org/package=boot.

Carter, S. B. (1965). Principles of cell motility: the direction of cell movement and cancer invasion. *Nature*, 208(5016):1183–7.

Chen, B., Kumar, G., Co, C. C., and Ho, C.-C. (2013). Geometric control of cell migration. *Scientific Reports*, 3:2827.

Chen, C. S., Mrksich, M., Huang, S., Whitesides, G. M., and Ingber, D. E. (1997). Geometric control of cell life and death. *Science (New York, N.Y.)*, 276(5317):1425–1428.

Crawley, M. J. (2007). *The R Book*. Wiley, Chichester, England.

Danjo, Y. and Gipson, I. K. (1998). Actin 'purse string' filaments are anchored by E-cadherin-mediated adherens junctions at the leading edge of the epithelial wound, providing coordinated cell movement. *Journal of Cell Science*, 111(Pt 2):3323–32.

Davies, J. (2009). Regulation, necessity, and the misinterpretation of knockouts. *BioEssays*, 31(8):826–30.

Davies, J. A. (2008). Synthetic morphology: prospects for engineered, self-constructing anatomies. *Journal of Anatomy*, 212(6):707–19.

Davies, J. A. (2013). *Mechanisms of Morphogenesis*. Academic Press, San Diego, CA, 2nd edition.

Davies, J. A., Hohenstein, P., Chang, C.-H., and Berry, R. (2014). A self-avoidance mechanism in patterning of the urinary collecting duct tree. *BMC Developmental Biology*, 14(1):1–12.

Deakin, N. O. and Turner, C. E. (2014). Paxillin inhibits HDAC6 to regulate microtubule acetylation, Golgi structure, and polarized migration. *The Journal of Cell Biology*, 206(3):395–413.

Deforet, M., Hakim, V., Yevick, H. G., Duclos, G., and Silberzan, P. (2014). Emergence of collective modes and tri-dimensional structures from epithelial confinement. *Nature Communications*, 5:3747.

Doxzen, K., Vedula, S. R. K., Leong, M. C., Hirata, H., Gov, N. S., Kabla, A. J., Ladoux, B., and Lim, C. T. (2013). Guidance of collective cell migration by substrate geometry. *Integrative Biology*, 5(8):1026–35.

Dukes, J. D., Whitley, P., and Chalmers, A. D. (2011). The MDCK variety pack: choosing the right strain. *BMC Cell Biology*, 12(1):43.

Dushek, O., Mueller, S., Soubies, S., Depoil, D., Caramalho, I., Coombs, D., and Valitutti, S. (2008). Effects of intracellular calcium and actin cytoskeleton on TCR mobility measured by fluorescence recovery. *PLoS ONE*, 3(12):e3913.

Elliott, H., Fischer, R. S., Myers, K. a., Desai, R. a., Gao, L., Chen, C. S., Adelstein, R. S., Waterman, C. M., and Danuser, G. (2015). Myosin II controls cellular branching morphogenesis and migration in three dimensions by minimizing cell-surface curvature. *Nature Cell Biology*, 17(2):137–47.

Farooqui, R. and Fenteany, G. (2005). Multiple rows of cells behind an epithelial wound edge extend cryptic lamellipodia to collectively drive cell-sheet movement. *Journal of Cell Science*, 118(Pt 1):51–63.

Fay, M. (2014). *rateratio.test: Exact Rate Ratio Test*. (R package version 1.0-2) [Computer software]. URL http://CRAN.R-project.org/package=rateratio.test.

Fels, J., Jeggle, P., Kusche-Vihrog, K., and Oberleithner, H. (2012). Cortical actin nanodynamics determines nitric oxide release in vascular endothelium. *PLoS ONE*, 7(7).

Fischer, R. S., Gardel, M., Ma, X., Adelstein, R. S., and Waterman, C. M. (2009). Local cortical tension by myosin II guides 3D endothelial cell branching. *Current Biology*, 19(3):260–5.

Folch, A. and Toner, M. (2000). Microengineering of cellular interactions. *Annual Review of Biomedical Engineering*, 2:227–56.

Folkman, J. and Moscona, A. (1978). Role of cell shape in growth control. *Nature*, 273:345–349.

Fouchard, J., Bimbard, C., Bufi, N., Durand-Smet, P., Proag, A., Richert, A., Cardoso, O., and Asnacios, A. (2014). Three-dimensional cell body shape dictates the onset

of traction force generation and growth of focal adhesions. *Proceedings of the National Academy of Sciences of the United States of America*, 111(36):13075–80.

Furuta, A., Tanaka, M., Omata, W., Nagasawa, M., Kojima, I., and Shibata, H. (2009). Microtubule disruption with BAPTA and dimethyl BAPTA by a calcium chelation-independent mechanism in 3T3-L1 adipocytes. *Endocrine Journal*, 56(2):235–43.

Giannone, G., Dubin-Thaler, B. J., Rossier, O., Cai, Y., Chaga, O., Jiang, G., Beaver, W., Döbereiner, H.-G., Freund, Y., Borisy, G., and Sheetz, M. P. (2007). Lamellipodial actin mechanically links myosin activity with adhesion-site formation. *Cell*, 128(3):561–75.

Gupton, S. L., Anderson, K. L., Kole, T. P., Fischer, R. S., Ponti, A., Hitchcock-DeGregori, S. E., Danuser, G., Fowler, V. M., Wirtz, D., Hanein, D., and Waterman-Storer, C. M. (2005). Cell migration without a lamellipodium: translation of actin dynamics into cell movement mediated by tropomyosin. *The Journal of Cell Biology*, 168(4):619–31.

Hamilton, V., Yuan, Y., Rigney, D. A., Puckett, A. D., Ong, J. L., Yang, Y., Elder, S. H., and Bumgardner, J. D. (2006). Characterization of chitosan films and effects on fibroblast cell attachment and proliferation. *Journal of Materials Science: Materials in Medicine*, 17(12):1373–81.

Harris, A. (1973). Behavior of cultured cells on substrata of variable adhesiveness. *Experimental Cell Research*, 77(1):285–97.

Harris, A. R., Daeden, A., and Charras, G. T. (2014). Formation of adherens junctions leads to the emergence of a tissue-level tension in epithelial monolayers. *Journal of Cell Science*, 127(Pt 11):2507–17.

Higashida, C., Kiuchi, T., Akiba, Y., Mizuno, H., Maruoka, M., Narumiya, S., Mizuno, K., and Watanabe, N. (2013). F- and G-actin homeostasis regulates mechanosensitive actin nucleation by formins. *Nature Cell Biology*, 15(4):395–405.

Hoffman, L., Farley, M. M., and Waxham, M. N. (2013). Calcium-calmodulin-dependent protein kinase II isoforms differentially impact the dynamics and structure of the actin cytoskeleton. *Biochemistry*, 52(7):1198–207.

Huda, S., Pilans, D., Makurath, M., Hermans, T., Kandere-Grzybowska, K., and Grzybowski, B. A. (2014). Microfabricated systems and assays for studying the cytoskeletal organization, micromechanics, and motility patterns of cancerous cells. *Advanced Materials Interfaces*, 1(7):1400158.

Ingber, D. E., Wang, N., and Stamenovic, D. (2014). Tensegrity, cellular biophysics, and the mechanics of living systems. *Reports on Progress in Physics*, 77(4):046603.

Ireland, G. W., Dopping-Hepenstal, P., Jordan, P., and O'Neill, C. (1987). Effect of patterned surfaces of adhesive islands on the shape, cytoskeleton, adhesion and behaviour of Swiss mouse 3T3 fibroblasts. *Journal of Cell Science. Supplement*, 8:19–33.

Ishikawa, S.-E. and Saito, T. (1990). Optimal concentration of cellular free calcium for AVP-induced cAMP in collecting tubules. *Kidney International*, 37(4):1060–6.

Jalilian, I., Heu, C., Cheng, H., Freittag, H., Desouza, M., Stehn, J. R., Bryce, N. S., Whan, R. M., Hardeman, E. C., Fath, T., Schevzov, G., and Gunning, P. W. (2015). Cell elasticity is regulated by the tropomyosin isoform composition of the actin cytoskeleton. *PloS ONE*, 10(5):e0126214.

James, J., Goluch, E. D., Hu, H., Liu, C., and Mrksich, M. (2008). Subcellular curvature at the perimeter of micropatterned cells influences lamellipodial distribution and cell polarity. *Cell Motility and the Cytoskeleton*, 65(11):841–52.

Janmey, P. A. and Schliwa, M. (2008). Rheology. *Current Biology*, 18(15):R639–R641.

Jiang, X., Bruzewicz, D. A., Wong, A. P., Piel, M., and Whitesides, G. M. (2005). Directing cell migration with asymmetric micropatterns. *Proceedings of the National Academy of Sciences of the United States of America*, 102(4):975–8.

Jin, Y., Atkinson, S. J., Marrs, J. A., and Gallagher, P. J. (2001). Myosin ii light chain phosphorylation regulates membrane localization and apoptotic signaling of tumor necrosis factor receptor-1. *The Journal of Biological Chemistry*, 276(32):30342–9.

Katoh, K., Kano, Y., and Noda, Y. (2011). Rho-associated kinase-dependent contraction of stress fibres and the organization of focal adhesions. *Journal of the Royal Society, Interface*, 8(56):305–11.

Katsumi, A., Milanini, J., Kiosses, W. B., del Pozo, M. A., Kaunas, R., Chien, S., Hahn, K. M., and Schwartz, M. A. (2002). Effects of cell tension on the small GTPase Rac. *The Journal of Cell Biology*, 158(1):153–64.

Kaufman, W. L., Kocman, I., Agrawal, V., Rahn, H.-P., Besser, D., and Gossen, M. (2008). Homogeneity and persistence of transgene expression by omitting antibiotic selection in cell line isolation. *Nucleic Acids Research*, 36(17):e111.

Khalil, A. A. and Friedl, P. (2010). Determinants of leader cells in collective cell migration. *Integrative Biology*, 2(11-12):568–74.

Kim, T.-J., Sun, J., Lu, S., Qi, Y.-X., and Wang, Y. (2014). Prolonged mechanical stretch initiates intracellular calcium oscillations in human mesenchymal stem cells. *PloS ONE*, 9(10):e109378.

Klarlund, J. K. (2012). Dual modes of motility at the leading edge of migrating epithelial cell sheets. *Proceedings of the National Academy of Sciences of the United States of America*, 109(39):15799–804.

Ko, K. S., Arora, P. D., and McCulloch, C. A. (2001). Cadherins mediate intercellular mechanical signaling in fibroblasts by activation of stretch-sensitive calcium-permeable channels. *The Journal of Biological Chemistry*, 276(38):35967–77.

Kumar, G., Chen, B., Co, C. C., and Ho, C.-C. (2011). Differential migration and proliferation of geometrical ensembles of cell clusters. *Experimental Cell Research*, 317(10):1340–52.

Kumar, G., Ho, C.-C., and Co, C. C. (2015). Cell-substrate interactions feedback to direct cell migration along or against morphological polarization. *PloS ONE*, 10(7):e0133117.

Kushiro, K., Chang, S., and Asthagiri, A. R. (2010). Reprogramming directional cell motility by tuning micropattern features and cellular signals. *Advanced Materials*, 22(40):4516–9.

Ladoux, B., Mège, R.-M., and Trepat, X. (2016). Front-rear polarization by mechanical cues: from single cells to tissues. *Trends in Cell Biology*, 26(6):420–33.

Leerberg, J. M., Gomez, G. A., Verma, S., Moussa, E. J., Wu, S. K., Priya, R., Hoffman, B. D., Grashoff, C., Schwartz, M. A., and Yap, A. S. (2014). Tension-sensitive actin assembly supports contractility at the epithelial zonula adherens. *Current Biology*, 24(15):1689–99.

Leong, M. C., Vedula, S. R. K., Lim, C. T., and Ladoux, B. (2013). Geometrical constraints and physical crowding direct collective migration of fibroblasts. *Communicative and Integrative Biology*, 6(2):e23197.

Limouze, J., Straight, A. F., Mitchison, T., and Sellers, J. R. (2004). Specificity of blebbistatin, an inhibitor of myosin II. *Journal of Muscle Research and Cell Motility*, 25(4-5):337–341.

Lin, H.-H., Lin, H.-K., Lin, I.-H., Chiou, Y.-W., Chen, H.-W., Liu, C.-Y., Harn, H. I.-C., Chiu, W.-T., Wang, Y.-K., Shen, M.-R., and Tang, M.-J. (2015). Mechanical phenotype of cancer cells: cell softening and loss of stiffness sensing. *Oncotarget*, 6(25):20946–58.

Liu, C. and Hermann, T. E. (1978). Characterization of ionomycin as a calcium ionophore. *The Journal of Biological Chemistry*, 253(17):5892–4.

Lomakin, A. J., Lee, K.-C., Han, S. J., Bui, D. A., Davidson, M., Mogilner, A., and Danuser, G. (2015). Competition for actin between two distinct F-actin networks defines a bistable switch for cell polarization. *Nature Cell Biology*, 17(11):1435–45.

Lou, S. S., Diz-Muñoz, A., Weiner, O. D., Fletcher, D. a., and Theriot, J. a. (2015). Myosin light chain kinase regulates cell polarization independently of membrane tension or Rho kinase. *The Journal of Cell Biology*, 209(2):275–88.

Marek, L. F., Kelley, R. O., and Perdue, B. D. (1982). Organization of the cytoskeleton in square fibroblasts. *Cell Motility*, 2(2):115–30.

Mark, S., Shlomovitz, R., Gov, N. S., Poujade, M., Grasland-Mongrain, E., and Silberzan, P. (2010). Physical model of the dynamic instability in an expanding cell culture. *Biophysical Journal*, 98(3):361–70.

Martinelli, R., Kamei, M., Sage, P. T., Massol, R., Varghese, L., Sciuto, T., Toporsian, M., Dvorak, A. M., Kirchhausen, T., Springer, T. A., and Carman, C. V. (2013). Release of cellular tension signals self-restorative ventral lamellipodia to heal barrier micro-wounds. *The Journal of Cell Biology*, 201(3):449–65.

Martins, G. G. and Kolega, J. (2012). A role for microtubules in endothelial cell protrusion in three-dimensional matrices. *Biology of the Cell*, 104(5):271–86.

Matthews, B. D., Thodeti, C. K., Tytell, J. D., Mammoto, A., Overby, D. R., and Ingber, D. E. (2010). Ultra-rapid activation of TRPV4 ion channels by mechanical forces applied to cell surface beta1 integrins. *Integrative Biology*, 2(9):435–42.

Mazzei, D., Guzzardi, M. A., Giusti, S., and Ahluwalia, A. (2010). A low shear stress modular bioreactor for connected cell culture under high flow rates. *Biotechnology and Bioengineering*, 106(1):127–137.

McPhee, G., Dalby, M. J., Riehle, M., and Yin, H. (2010). Can common adhesion molecules and microtopography affect cellular elasticity? A combined atomic

force microscopy and optical study. *Medical and Biological Engineering and Computing*, 48(10):1043–1053.

Müller, M. S., Obel, L. F., Waagepetersen, H. S., Schousboe, A., and Bak, L. K. (2013). Complex actions of ionomycin in cultured cerebellar astrocytes affecting both calcium-induced calcium release and store-operated calcium entry. *Neurochemical Research*, 38(6):1260–5.

Nagasawa, M. and Kojima, I. (2015). Translocation of TRPV2 channel induced by focal administration of mechanical stress. *Physiological Reports*, 3(2):e12296–e12296.

Nelson, C. M., Vanduijn, M. M., Inman, J. L., Fletcher, D. A., and Bissell, M. J. (2006). Tissue geometry determines sites of mammary branching morphogenesis in organotypic cultures. *Science (New York, N.Y.)*, 314(5797):298–300.

Nicholson-Dykstra, S. M. and Higgs, H. N. (2008). Arp2 depletion inhibits sheet-like protrusions but not linear protrusions of fibroblasts and lymphocytes. *Cell Motility and the Cytoskeleton*, 65(11):904–22.

Norman, L. L., Brugués, J., Brugés, J., Sengupta, K., Sens, P., and Aranda-Espinoza, H. (2010). Cell blebbing and membrane area homeostasis in spreading and retracting cells. *Biophysical Journal*, 99(6):1726–33.

Okeyo, K. O., Nagasaki, M., Sunaga, J., Hojo, M., Kotera, H., and Adachi, T. (2011). Effect of actomyosin contractility on lamellipodial protrusion dynamics on a micropatterned substrate. *Cellular and Molecular Bioengineering*, 4(3):389–398.

Omelchenko, T., Vasiliev, J. M., Gelfand, I. M., Feder, H. H., and Bonder, E. M. (2003). Rho-dependent formation of epithelial "leader" cells during wound healing. *Proceedings of the National Academy of Sciences of the United States of America*, 100(19):10788–93.

O'Neill, C., Jordan, P., and Ireland, G. (1986). Evidence for two distinct mechanisms of anchorage stimulation in freshly explanted and 3T3 Swiss mouse fibroblasts. *Cell*, 44(3):489–96.

O'Neill, C., Jordan, P., Riddle, P., and Ireland, G. (1990). Narrow linear strips of adhesive substratum are powerful inducers of both growth and total focal contact area. *Journal of Cell Science*, 95 (Pt 4):577–86.

Parker, K. K., Brock, A. L., Brangwynne, C., Mannix, R. J., Wang, N., Ostuni, E., Geisse, N. A., Adams, J. C., Whitesides, G. M., and Ingber, D. E. (2002). Directional control of lamellipodia extension by constraining cell shape and orienting cell tractional forces. *FASEB Journal*, 16(10):1195–204.

Pasapera, A. M., Schneider, I. C., Rericha, E., Schlaepfer, D. D., and Waterman, C. M. (2010). Myosin II activity regulates vinculin recruitment to focal adhesions through FAK-mediated paxillin phosphorylation. *The Journal of Cell Biology*, 188(6):877–90.

Peinado, H., Quintanilla, M., and Cano, A. (2003). Transforming growth factor beta-1 induces snail transcription factor in epithelial cell lines: mechanisms for epithelial mesenchymal transitions. *The Journal of Biological Chemistry*, 278(23):21113–23.

Pietuch, A. and Janshoff, A. (2013). Mechanics of spreading cells probed by atomic force microscopy. *Open Biology*, 3(7):130084.

Plotnikov, S. V. and Waterman, C. M. (2013). Guiding cell migration by tugging. *Current Opinion in Cell Biology*, 25(5):619–26.

Poujade, M., Grasland-Mongrain, E., Hertzog, A., Jouanneau, J., Chavrier, P., Ladoux, B., Buguin, A., and Silberzan, P. (2007). Collective migration of an epithelial monolayer in response to a model wound. *Proceedings of the National Academy of Sciences of the United States of America*, 104(41):15988–93.

Price, L. S., Langeslag, M., ten Klooster, J. P., Hordijk, P. L., Jalink, K., and Collard, J. G. (2003). Calcium signaling regulates translocation and activation of Rac. *The Journal of Biological Chemistry*, 278(41):39413–21.

R Core Team (2015). *R: A Language and Environment for Statistical Computing*. (Version 3.2.1) [Computer software]. R Foundation for Statistical Computing, Vienna, Austria. URL http://www.R-project.org/.

Rape, A. D., Guo, W.-H., and Wang, Y.-L. (2011). The regulation of traction force in relation to cell shape and focal adhesions. *Biomaterials*, 32(8):2043–51.

Rausch, S., Das, T., Soiné, J. R., Hofmann, T. W., Boehm, C. H., Schwarz, U. S., Boehm, H., and Spatz, J. P. (2013). Polarizing cytoskeletal tension to induce leader cell formation during collective cell migration. *Biointerphases*, 8(1):36.

Ravasio, A., Cheddadi, I., Chen, T., Pereira, T., Ong, H. T., Bertocchi, C., Brugues, A., Jacinto, A., Kabla, A. J., Toyama, Y., Trepat, X., Gov, N., Neves de Almeida,

L., and Ladoux, B. (2015). Gap geometry dictates epithelial closure efficiency. *Nature Communications*, 6:7683.

Reffay, M., Parrini, M. C., Cochet-Escartin, O., Ladoux, B., Buguin, A., Coscoy, S., Amblard, F., Camonis, J., and Silberzan, P. (2014). Interplay of RhoA and mechanical forces in collective cell migration driven by leader cells. *Nature Cell Biology*, 16(3):217–23.

Riedl, J., Crevenna, A. H., Kessenbrock, K., Yu, J. H., Bista, M., Bradke, F., Jenne, D., Holak, T. A., Werb, Z., Sixt, M., Wedlich-Soldner, R., Klopferspitz, A., Avenue, P., Francisco, S., Neukirchen, D., Bista, M., Bradke, F., Jenne, D., Holak, T. A., Werb, Z., Sixt, M., Wedlich-Soldner, R., Klopferspitz, A., Avenue, P., and Francisco, S. (2008). Lifeact: a versatile marker to visualize F-actin. *Nature Methods*, 5(7):605–7.

Rodat-Despoix, L., Hao, J., Dandonneau, M., and Delmas, P. (2013). Shear stress-induced Ca2+ mobilization in MDCK cells is ATP dependent, no matter the primary cilium. *Cell Calcium*, 53(5-6):327–337.

Rolli, C. G., Nakayama, H., Yamaguchi, K., Spatz, J. P., Kemkemer, R., and Nakanishi, J. (2012). Switchable adhesive substrates: revealing geometry dependence in collective cell behavior. *Biomaterials*, 33(8):2409–18.

RStudio Team (2015). *RStudio: Integrated Development Environment for R*. (Version 0.99.473) [Computer software]. RStudio, Inc, Boston, MA. URL http://www.rstudio.com/.

Russo, J. M., Florian, P., Shen, L., Graham, W. V., Tretiakova, M. S., Gitter, A. H., Mrsny, R. J., and Turner, J. R. (2005). Distinct temporal-spatial roles for rho kinase and myosin light chain kinase in epithelial purse-string wound closure. *Gastroenterology*, 128(4):987–1001.

Sakamoto, T., Limouze, J., Combs, C. A., Straight, A. F., and Sellers, J. R. (2005). Blebbistatin, a myosin II inhibitor, is photoinactivated by blue light. *Biochemistry*, 44(2):584–588.

Saoudi, Y., Rousseau, B., Doussière, J., Charrasse, S., Gauthier-Rouvière, C., Morin, N., Sautet-Laugier, C., Denarier, E., Scaïfe, R., Mioskowski, C., and Job, D. (2004). Calcium-independent cytoskeleton disassembly induced by BAPTA. *European Journal of Biochemistry*, 271(15):3255–64.

Sbrana, T. and Ahluwalia, A. (2012). Engineering Quasi-Vivo in vitro organ models. In Balls, M., Combes, R. D., and Bhogal, N., editors, *New Technologies for Toxicity Testing*, volume 745 of the series, pages 138–53. Springer US.

Schillers, H., Wälte, M., Urbanova, K., and Oberleithner, H. (2010). Real-time monitoring of cell elasticity reveals oscillating myosin activity. *Biophysical Journal*, 99(11):3639–46.

Schuck, S., Manninen, A., Honsho, M., Füllekrug, J., and Simons, K. (2004). Generation of single and double knockdowns in polarized epithelial cells by retrovirus-mediated RNA interference. *Proceedings of the National Academy of Sciences of the United States of America*, 101(14):4912–7.

Sero, J. E., German, A. E., Mammoto, A., and Ingber, D. E. (2012). Paxillin controls directional cell motility in response to physical cues. *Cell Adhesion and Migration*, 6(6):502–8.

Shao, X., Li, Q., Mogilner, A., Bershadsky, A. D., and Shivashankar, G. V. (2015). Mechanical stimulation induces formin-dependent assembly of a perinuclear actin rim. *Proceedings of the National Academy of Sciences of the United States of America*, 112(20):E2595–601.

Shoji, K., Ohashi, K., Sampei, K., Oikawa, M., and Mizuno, K. (2012). Cytochalasin D acts as an inhibitor of the actin-cofilin interaction. *Biochemical and Biophysical Research Communications*, 424(1):52–7.

Singhvi, R., Kumar, A., Lopez, G. P., Stephanopoulos, G. N., Wang, D. I., Whitesides, G. M., and Ingber, D. E. (1994). Engineering cell shape and function. *Science (New York, N.Y.)*, 264(5159):696–698.

Squires, T. M., Messinger, R. J., and Manalis, S. R. (2008). Making it stick: convection, reaction and diffusion in surface-based biosensors. *Nature Biotechnology*, 26(4):417–26.

Stevenson, B. R. and Begg, D. A. (1994). Concentration-dependent effects of cytochalasin D on tight junctions and actin filaments in MDCK epithelial cells. *Journal of Cell Science*, 107(Pt 3):367–75.

Stimac, G. (2013). *Geometry is sufficient to induce motility in Madin-Darby canine kidney type II (MDCKII) cells in tubulogenesis and branching morphogenesis, and motility is not due to concentration gradients of inhibitors affected by geometry*. Masters thesis, The University of Edinburgh.

Stuart, R. O., Sun, A., Panichas, M., Hebert, S. C., Brenner, B. M., and Nigam, S. K. (1994). Critical role for intracellular calcium in tight junction biogenesis. *Journal of Cellular Physiology*, 159(3):423–33.

Suffoletto, K., Ye, N., Meng, F., Verma, D., and Hua, S. Z. (2015). Intracellular forces during guided cell growth on micropatterns using FRET measurement. *Journal of Biomechanics*, 48(4):627–35.

Tamada, M., Perez, T. D., Nelson, W. J., and Sheetz, M. P. (2007). Two distinct modes of myosin assembly and dynamics during epithelial wound closure. *The Journal of Cell Biology*, 176(1):27–33.

Tamura, M., Nakao, H., Yoshizaki, H., Shiratsuchi, M., Shigyo, H., Yamada, H., Ozawa, T., Totsuka, J., and Hidaka, H. (2005). Development of specific Rho-kinase inhibitors and their clinical application. *Biochimica et Biophysica Acta*, 1754(1-2):245–52.

Théry, M., Racine, V., Piel, M., Pépin, A., Dimitrov, A., Chen, Y., Sibarita, J.-B., and Bornens, M. (2006). Anisotropy of cell adhesive microenvironment governs cell internal organization and orientation of polarity. *Proceedings of the National Academy of Sciences of the United States of America*, 103(52):19771–6.

Tsai, F.-C. and Meyer, T. (2012). Ca2+ pulses control local cycles of lamellipodia retraction and adhesion along the front of migrating cells. *Current Biology*, 22(9):837–42.

Turner, N., Armitage, M., Butler, R., and Ireland, G. (2004). An in vitro model to evaluate cell adhesion to metals used in implantation shows significant differences between palladium and gold or platinum. *Cell Biology International*, 28(7):541–547.

Tymianski, M., Spigelman, I., Zhang, L., Carlen, P. L., Tator, C. H., Charlton, M. P., and Wallace, M. C. (1994). Mechanism of action and persistence of neuroprotection by cell-permeant Ca2+ chelators. *Journal of Cerebral Blood Flow and Metabolism*, 14(6):911–23.

Vedula, S. R. K., Leong, M. C., Lai, T. L., Hersen, P., Kabla, A. J., Lim, C. T., and Ladoux, B. (2012). Emerging modes of collective cell migration induced by geometrical constraints. *Proceedings of the National Academy of Sciences of the United States of America*, 109(32):12974–9.

Verkhovsky, A. B. (2015). The mechanisms of spatial and temporal patterning of cell-edge dynamics. *Current Opinion in Cell Biology*, 36:113–21.

Verkhovsky, A. B., Svitkina, T. M., and Borisy, G. G. (1997). Polarity sorting of actin filaments in cytochalasin-treated fibroblasts. *Journal of Cell Science*, 110(Pt 1):1693–704.

Verma, D., Meng, F., Sachs, F., and Hua, S. Z. (2015). Flow-induced focal adhesion remodeling mediated by local cytoskeletal stresses and reorganization. *Cell Adhesion and Migration*, 9(6):432–40.

Wakatsuki, T., Schwab, B., Thompson, N. C., and Elson, E. L. (2001). Effects of cytochalasin D and latrunculin B on mechanical properties of cells. *Journal of Cell Science*, 114(Pt 5):1025–36.

Wang, J., Heo, J., and Hua, S. Z. (2010). Spatially resolved shear distribution in microfluidic chip for studying force transduction mechanisms in cells. *Lab on a Chip*, 10(2):235–9.

Watanabe, T., Hosoya, H., and Yonemura, S. (2007). Regulation of myosin II dynamics by phosphorylation and dephosphorylation of its light chain in epithelial cells. *Molecular Biology of the Cell*, 18(2):605–16.

Watt, F. M., Jordan, P. W., and O'Neill, C. H. (1988). Cell shape controls terminal differentiation of human epidermal keratinocytes. *Proceedings of the National Academy of Sciences of the United States of America*, 85(15):5576–80.

Wei, C., Wang, X., Zheng, M., and Cheng, H. (2012). Calcium gradients underlying cell migration. *Current Opinion in Cell Biology*, 24(2):254–61.

Westermark, B. (1978). Growth control in miniclones of human glial cells. *Experimental Cell Research*, 111(2):295–9.

Whipple, R. A., Balzer, E. M., Cho, E. H., Matrone, M. A., Yoon, J. R., and Martin, S. S. (2008). Vimentin filaments support extension of tubulin-based microtentacles in detached breast tumor cells. *Cancer Research*, 68(14):5678–88.

Wulf, E., Deboben, A., Bautz, F. A., Faulstich, H., and Wieland, T. (1979). Fluorescent phallotoxin, a tool for the visualization of cellular actin. *Proceedings of the National Academy of Sciences of the United States of America*, 76(9):4498–4502.

Xia, N., Thodeti, C. K., Hunt, T. P., Xu, Q., Ho, M., Whitesides, G. M., Westervelt, R., and Ingber, D. E. (2008). Directional control of cell motility through focal adhesion positioning and spatial control of Rac activation. *FASEB Journal*, 22(6):1649–59.

Yang, Y., Jamilpour, N., Yao, B., Dean, Z. S., Riahi, R., and Wong, P. K. (2016). Probing leader cells in endothelial collective migration by plasma lithography geometric confinement. *Scientific Reports*, 6:22707.

Yarrow, J. C., Lechler, T., Li, R., and Mitchison, T. J. (2003). Rapid de-localization of actin leading edge components with BDM treatment. *BMC Cell Biology*, 4:5.

Yuan, X., Zhou, M., Gough, J., Glidle, A., and Yin, H. (2015). A novel culture system for modulating single cell geometry in 3D. *Acta Biomaterialia*, 24:228–240.

Zhao, X.-H., Laschinger, C., Arora, P., Szászi, K., Kapus, A., and McCulloch, C. A. (2007). Force activates smooth muscle alpha-actin promoter activity through the Rho signaling pathway. *Journal of Cell Science*, 120(Pt 10):1801–9.

Zheng, W., Xie, Y., Sun, K., Wang, D., Zhang, Y., Wang, C., Chen, Y., and Jiang, X. (2014). An on-chip study on the influence of geometrical confinement and chemical gradient on cell polarity. *Biomicrofluidics*, 8(5):052010.

APPENDICES

A.1 ImageJ script for anonymising images

The following script was used to anonymise images of treated and control micropatterned cells prior to image analysis, to minimise the risk of experimenter bias. Images from each experimental run were pooled and given unique code names with random numbers for each individual image, and a reference file with the original file names was saved to re-identify anonymised images after data capture.

```
1  // Get path of directory containing images folder
2  dir = getDirectory("Choose directory containing folder of
       images to be listed (should already contain matched file
       with code numbers).");
3
4  // Check that images folder is present
5  imfolder = File.isDirectory(dir+"/images");
6  if (imfolder==0) {
7           exit("Error! No 'images' directory present!");
8           }
9
10 // Count images to be processed
11 filename = getFileList(dir+"/images");
12 numImages = filename.length;
13
14 // Create subfolder for anonymised images
15 ANONdir = dir+"anon/";
16 File.makeDirectory(ANONdir);
17
18 // Get code numbers as an array
19 pathfile = File.openDialog("Select text file containing code
       numbers.");
20 filestring = File.openAsString(pathfile);
21 codenum = split(filestring, "\n");
22
```

```
23 // Check that sufficient code numbers are present to rename all
       files
24 if (codenum.length<numImages) {
25         exit("Error! Not enough code numbers in file!");
26         }
27
28 // Get prefix to for codenames
29 Dialog.create("Codename prefix");
30 prefix = "R1-";
31 Dialog.addString("Prefix for renaming images:", prefix);
32 Dialog.show();
33 prefix = Dialog.getString();
34
35 // List original filenames sequentially in Log window along
      with codename, and rename
36 print("filename\t", "codename\t");
37 for (i=0; i<numImages; i++) {
38         codename = prefix+codenum[i];
39         open(dir+"/images/"+filename[i]);
40         saveAs("Jpeg",ANONdir+codename);
41         close();
42         print(filename[i], codename);
43 }
44
45 // Create tab-delimited text file for names (single line per
      file) - transfer list of filenames from Log window
46 File.append(getInfo("log"),dir+"codenames.txt");
47 print("\\Clear");
```

A.2 ImageJ script for isolating micropatterns

The following script was used to rapidly isolate individual micropatterns from captured images (previously given unique, anonymised codenames), saving both the isolated image, and the ROI used to capture it, with a filename that references the original image and uniquely identifies that micropattern for future analysis.

```
1 dir = getDirectory("image");
2 scaffolddir = dir+"ROI/";
3 File.makeDirectory(scaffolddir);
4
5 Dialog.create("Note");
```

```
Dialog.addMessage("Choose scaffolds for analysis with rectangle
    selection tool (leave plenty of space). Ctrl+t to select.
   Shift when completed.");
Dialog.show();

continue = 0;

while (continue==0) {

        roiManager("reset");

        imagename=getInfo("image.filename");
        dotIndex = indexOf(imagename, ".");
        imageID = substring(imagename, 0, dotIndex);

        while (isKeyDown("Shift")==0) {}

        // Identify scaffolds in ROI
        n = roiManager("count");
        for (i=0; i<n; i++)  {
                roiManager("select", i);
                roiID=i+1;
                scaffoldID=imageID+"-"+roiID;
                roiManager("rename", scaffoldID);
                run("Duplicate...", "title=["+scaffoldID+".jpg]
                   ");
                run("Invert");
                saveAs("Jpeg",scaffolddir+scaffoldID);
                close();
                }

        // Save ROI for later use
        roiManager("deselect");
        roiManager("Save",dir+imageID+" ROI"+".zip");

        run("Open Next");

}

run("Close All");
```

A.3 ImageJ script for counting protrusions

The following script was used to facilitate rapid manual counting of protrusions at each of the eight segments at the periphery of anonymised micropatterns. Count data is captured automatically following the marking of each protrusion in a given segment (or segments are marked as 'uncounted' in the event that cells have escaped over, or failed to reach, the boundary of the underlying pattern, or if the pattern is otherwise obscured), and the script automatically steps through segments and image files for efficient image processing. In addition to time-stamped numerical data, annotated image files are output to leave a record of the data-gathering process for later checks.

```
1  // Create subfolder for annotated copies of images
2  dir = getDirectory("image");
3  lamellidir = dir+"lamellipodia/";
4  File.makeDirectory(lamellidir);
5
6  // Get date-time-stamp to identify results of this session;
       format yymmddhhmm
7  getDateAndTime(year, month, dayOfWeek, dayOfMonth, hour, minute
       , second, msec);
8  outputID = substring(year,2);
9  month = month+1;
10 if (month<10) {outputID = outputID+"0";}
11 outputID = outputID + month;
12 if (dayOfMonth<10) {outputID = outputID+"0";}
13 outputID = outputID + dayOfMonth;
14 if (hour<10) {outputID = outputID+"0";}
15 outputID = outputID + hour;
16 if (minute<10) {outputID = outputID+"0";}
17 outputID = outputID + minute;
18
19 // Create tab-delimited text file for measurements (single line
       per segment) - transfer from Log window
20 print("session\t", "imageID\t", "segmentID\t", "lamellipodia\t"
       );
21 outputfile = File.open(lamellidir+outputID+" data.txt");
22 File.append(getInfo("log"),lamellidir+outputID+" data.txt");
23 print("\\Clear");
24
25 // ROIs to be displayed as they are created
26 roiManager("Set Color", "white");
27 roiManager("Show All with labels");
```

```
28 roiManager("UseNames", "true");
29
30 // Instructions to user
31 showMessage("'Alt' if segment is correct shape; 'Space' if
      segment is misshapen (skip to next segment).");
32 showMessage("Top-left shows the segment currently being
      evaluated; use point tool to mark lamellipodia, then hit '
      Shift' when complete.");
33 showMessage("Start with segment 1 (shorter 'finger'), and
      continue in numerical order (move in direction of longer '
      finger'.");
34
35 // Loop to process and analyse each image
36 continue = 1;
37 while (continue==1) {
38
39         roiManager("reset");
40
41         run("Set... ", "zoom=180 x=0 y=0");
42
43         // Identify image being analysed
44         imagename=getInfo("image.filename");
45         dotIndex = indexOf(imagename, ".");
46         imageID = substring(imagename, 0, dotIndex);
47
48         // Loop to process and analyse each segment in the
              image
49         segmentID = 1;
50         prevROI = 0;
51         while (segmentID<9)  {
52
53                 // Create ROI to record segment results as
                      annotation & prompt for segment
54                 vertdisp = 8; // Vertical displacement of each
                      ROI to form the grid
55                 vert = (segmentID-1)*vertdisp;  // Vertical (y)
                       coordinate
56                 makeRectangle(0,vert,40,vertdisp); // Place
                      each segment ROI sequentially in a grid at
                      the top left
57                 setKeyDown("none"); // NB: holding down 'Alt'
                      modifies roiManager("Add") to "Add and
                      rename"
58                 roiManager("Add");
59                 roiManager("select", prevROI);
60                 roiManager("rename", "S"+segmentID+" OK?");
```

```
61
62                  // Note if segment is correct shape (Alt) or
                        misshapen (Space)
63                  segOK=0;
64                  segNOK=0;
65                  while (segOK==0 && segNOK==0) {
66                          segOK=isKeyDown("Alt");
67                          segNOK=isKeyDown("Space");
68
69                          // segment can't be 'OK' and 'not OK'
                                at the same time
70                          if (segOK==1 && segNOK==1) {
71                                  segOK=0;
72                                  segNOK=0;
73                          }
74
75                  }
76
77                  // Pause until key is released
78                  do {
79                          checkalt = isKeyDown("Alt");
80                          checkspace = isKeyDown("Space");
81                  } while (checkalt + checkspace != 0);
82
83                  // If segment is correct shape, identify
                        lamellipodia manually
84                  if (segOK==1) {
85
86                          // Prompt for lamellipodia count
87                          roiManager("select", prevROI);
88                          roiManager("rename", "S"+segmentID+" =
                                ?");
89
90                          // Wait until user finishes marking all
                                lamellipodia
91                          setTool("point");
92                          selectWindow("Log");
93                          selectWindow(imagename); // Added
                                switch to Log and back to get around
                                mysterious bug when lam = 0
94                          while (isKeyDown("Shift")==0) {
95                          }
96
97                          // Calculate number of lamellipodia
98                          nROI = roiManager("count");
```

```
99                          lamellipodia = nROI - prevROI - 1; //
                               taking into account ROI from
                               previous segments, and 'segment
                               annotation' ROI
100
101                         // Update segment annotation
102                         roiManager("select", prevROI);
103                         roiManager("rename", "S"+segmentID+" =
                               "+lamellipodia);
104
105                         // Rename lamellipodia ROI to reflect
                               segmentID
106                         for (i=prevROI+1; i<nROI; i++)  {
107                                 roiManager("select", i);
108                                 roiManager("rename", "S"+
                                       segmentID+" #"+i-prevROI);
109                         }
110
111                 } else {
112
113                         // Update segment annotation
114                         lamellipodia = "N";
115                         roiManager("select", prevROI);
116                         roiManager("rename", "S"+segmentID+" =
                               "+lamellipodia);
117
118                 }
119
120                 // Pause until key is released
121                 do {
122                         checkshift = isKeyDown("Shift");
123                 } while (checkshift != 0);
124
125                 prevROI = roiManager("count"); // update count
                       of ROI for next calculation
126
127                 // Output data to Log window
128                 print(outputID, "\t", imageID, "\t", segmentID,
                        "\t", lamellipodia);
129
130                 segmentID = segmentID+1;
131
132         }
133
134         // Add pause to allow analysis to be stopped without
               saving (in case of error, incomplete analysis, etc)
```

```
135         continue = getBoolean("Continue?");
136         if (continue==1) {
137
138                 // Flatten ROIs for reference image
139                 roiManager("deselect");
140                 run("Select None");
141                 run("Flatten");
142
143                 // Save ROIs
144                 roiManager("Save",dir+imageID+" "+outputID+".
                        zip");
145                 roiManager("reset");
146
147                 // Save image with lamellipodia markings for
                        reference
148                 saveAs("Jpeg", lamellidir+imageID+" "+outputID)
                        ;
149                 close();
150
151                 // Save results and clear log window
152                 File.append(getInfo("log"),lamellidir+outputID+
                        " data.txt");
153                 print("\\Clear");
154
155                 run("Revert");
156                 run("Open Next");
157
158         } else {
159
160                 // Clear Log window
161                 print("\\Clear");
162
163                 continue = 1;
164         }
165
166 }
```

A.4 R script for plotting segment cell density data with results table

The following R script was used to generate Table 4.3 (p.36), and both plots in Figure 4.5 (p.38).

```
## For creating a box-and-whisker plot of cell counts along
## ... individual scaffold segments with a table of statistics
## ... (including upper and lower quartiles), and a bar plot of
## ... segment length (in um) divided by mean segment cell
## ... count (to give an indication of the length of 'edge'
## ... occupied by cells in each segment)


## get directory containing data
dir <- "C:/Users/Kim Martin/PhD thesis R analysis"

## create timestamped directory for output
tstamp <- paste("Segment density", format(Sys.time(), "%y%m%d%H
    %M%S"))
outdir <- paste(dir, tstamp, sep = "/")
dir.create(outdir)
setwd(outdir)

# import data
datafile <- paste(dir, "seg cell density.csv", sep = "/")
segdata <- read.csv(file = datafile, header = TRUE, na = "NA")
datafile <- paste(dir, "seg length.csv", sep = "/")
lendata <- read.csv(file = datafile, header = TRUE, na = "NA")


# add CFV segment numbering (ordered by original segment number
    , 1-8)

CFV.match <- c("V2", "C1", "V3", "F1", "C3", "V1", "C2", "F2")

for (seg in 1:8) {

  segdata$segCFV[segdata$segmentID == seg] <- CFV.match[seg]
  lendata$segCFV[lendata$seg.ID == seg] <- CFV.match[seg]
}


# order CFV segment numbering factor by curvature (C1, C2, C3,
    F1, ..., V3)
```

```
37
38 match.names = sort(CFV.match)
39
40 segdata$segCFV <- factor(segdata$segCFV, levels = match.names)
41
42
43 ## create table of statistics for cell counts along each
      segment
44
45 # isolate data by segment
46 seg.nuc <- split(segdata$nuclei, segdata$segCFV)
47
48
49 # get number (N) of data points, mean, std deviation, and
      median
50
51 nuc.n <- sapply(seg.nuc, length)
52 nuc.av <- sapply(seg.nuc, mean)
53 nuc.sd <- sapply(seg.nuc, sd)
54 nuc.med <- sapply(seg.nuc, median)
55
56
57 # get interquartile range (IQR), min, max
58
59 nuc.min <- sapply(seg.nuc, quantile)[1, ] # minimum cells
60 nuc.max <- sapply(seg.nuc, quantile)[5, ] # maximum cells
61
62 nuc.LQ <- sapply(seg.nuc, quantile)[2, ]  # lower quartile
63 nuc.UQ <- sapply(seg.nuc, quantile)[4, ]  # upper quartile
64
65 nuc.IQR <- nuc.UQ - nuc.LQ  # interquartile range
66
67
68 # get mode for cells/seg
69
70 getmode <- function(v) {
71   uniqv <- unique(v)
72   uniqv[which.max(tabulate(match(v, uniqv)))]
73 }
74
75 nuc.mode <- sapply(seg.nuc, getmode)
76
77
78 # specify significant figures for mean cell counts
79
```

```
sig.nuc.av <- signif(nuc.av, 2) # round mean to 2 significant
   figures


# specify number of decimal places for cell count standard
# ... deviation (match mean values) all segments except V1
# ... have mean value with 1 decimal place

vsig <- c(rep(1, 5), 0, 1, 1) # V1 has 0 decimal places

sig.nuc.sd <- round(nuc.sd, digits=vsig)


# create table for summary statistics and and output

rows.out <- c("N", "Mean", "SD", "Median", "IQR", "Min", "LQ",
   "UQ", "Max", "Mode")

cols.out <- match.names

seg.nuc.out <- rbind(nuc.n, sig.nuc.av, sig.nuc.sd,
                     nuc.med, nuc.IQR,
                     nuc.min, nuc.LQ, nuc.UQ, nuc.max,
                     nuc.mode)

colnames(seg.nuc.out) <- cols.out
rownames(seg.nuc.out) <- rows.out

write.csv(seg.nuc.out, file=paste(tstamp, "stats.csv"), row.
   names=T)


## create box plot of cell counts along each segment

png(paste(tstamp, "boxplot.png"))

boxplot(nuclei~segCFV, data=segdata, varwidth=T, ylim=c(0,14),
        names=match.names,
        xlab="segments from concave to convex",
        ylab="cells at segment edge",
        cex.axis=1.4, cex.lab=1.6)

points(1:8, nuc.av, pch=15, col="red")  # plot mean values

dev.off() # save completed plot to file

```

```
123
124 ## create bar plot to show average segment edge length taken up
        by cells
125
126 # calculate normalised length/cell
127
128 av.seg.len <- lendata$seg.len.av[lendata$segCFV == match.names]
129 sd.seg.len <- lendata$seg.len.sd[lendata$segCFV == match.names]
130
131 len.cell <- av.seg.len / nuc.av
132
133
134 # calculate standard deviation for length/cell values
135
136 sd.len.cell <- len.cell * sqrt((sd.seg.len/av.seg.len)^2 + (nuc
        .sd/nuc.av)^2)
137
138
139 # output a barplot of all normalised length/cell with standard
        deviation error bars
140
141 png(paste(tstamp, "barplot.png"))
142
143 maxh <- ceiling(max(len.cell + sd.len.cell))  # ensure error
        bars fit in plot window
144
145 bars <- barplot(len.cell, col="white", ylim=c(0,maxh), names.
        arg=match.names,
146                 xlab="segments from concave to convex", ylab="
                        length/cell (um) +/- SD",
147                 cex.axis=1.4, cex.lab=1.6, cex.names=1.4)
148
149 arrows(bars, (len.cell - sd.len.cell),
150        bars, (len.cell + sd.len.cell),
151        length = 0.05, angle = 90, code = 3)
152
153 dev.off() # save completed plot to file
```

A.5 R script for plotting protrusion counts with Poisson distribution

The following R script was used to generate Figure 4.6 (p.40).

```
## For plotting flow control data lamellipodia counts as
## ... histograms (one per segment) with paired box plot
## ... under x axis to indicate range of cell counts per
## ... segment, and overlaid Poisson distribution.

# get directory containing data
dir <- "C:/Users/Kim Martin/PhD thesis R analysis"

# create timestamped directory for output
tstamp <- paste("Poisson histogram", format(Sys.time(), "%y%m%d
    %H%M%S"))
outdir <- paste(dir, tstamp, sep = "/")
dir.create(outdir)
setwd(outdir)

# import data
datafile <- paste(dir, "flow lam counts.csv", sep = "/")
adata <- read.csv(file = datafile, header = TRUE, na = "NA")
datafile <- paste(dir, "seg cell density.csv", sep = "/")
segdata <- read.csv(file = datafile, header = TRUE, na = "NA")

# omit NA and FLOW - keep CTRL data only
adata <- adata[adata$treatment == "CTRL", ]
adata <- na.omit(adata)

# add CFV segment numbering (ordered by original segment number
    , 1-8)

CFV.match <- c("V2", "C1", "V3", "F1", "C3", "V1", "C2", "F2")

for (seg in 1:8) {

  adata$segCFV[adata$segmentID == seg] <- CFV.match[seg]

}

# create table to hold counts for each segment and output raw
    counts

max.lam <- max(adata$lamellipodia)
```

```
38
39 protrusions <- factor(adata$lamellipodia, levels=0:max.lam) #
      change to factor to include all 0 counts
40
41 dist.lam <- table(protrusions, adata$segmentID)
42
43 colnames(dist.lam) <- CFV.match
44
45 write.csv(cbind(rownames(dist.lam), dist.lam),
46           file=paste(tstamp, " ", scriptn, "_v", scriptv, "
                counts.csv"),
47           row.names=FALSE)
48
49 # create table of proportional frequencies
50
51 num.seg <- matrix(colSums(dist.lam), nrow=max.lam+1, ncol=8,
      byrow=T)
52
53 prop.dist <- dist.lam / num.seg
54
55 # get mean and variation of lamellipodia counts by segment
56
57 mean.lam <- tapply(adata$lamellipodia, adata$segmentID, mean)
58
59 var.lam <- tapply(adata$lamellipodia, adata$segmentID, var)
60
61 ## output barplots showing proportional frequencies of
      lamellipodia counts per segment
62 ## + add segment cell density histogram underneath
63
64 for (seg in 1:8) {
65
66   png(paste(tstamp, CFV.match[seg], "hist.png"))
67
68   # adjust for segments with more cells than the maximum
        lamellipodia count (extend x axis especially)
69
70   seg.max.cell <- max(segdata$nuclei[segdata$segmentID == seg])
71
72   if(seg.max.cell > max.lam) {
73
74     y.bound <- seg.max.cell
75
76     extend.axis <- rep(0, times=seg.max.cell-max.lam)
77     names(extend.axis) <- (max.lam+1):seg.max.cell
78
```

```
79      hist.data <- c(prop.dist[, seg], extend.axis)
80
81    } else {
82
83      y.bound <- max.lam
84
85      hist.data <- prop.dist[, seg]
86
87    }
88
89    ## Set up lower plot for boxplot and get offset to match
          boxplot to barplot
90
91    par(fig=c(0, 1, 0, 0.5)) # x,x,y,y coords of boxplot frame
92
93    # plot lamellipodia histogram 'invisibly' to set up axes for
          cell count boxplot
94    barcoords <- barplot(hist.data, beside = TRUE, ylim=c(0.5,2),
95                         col="white", border="white", axes=F,
                                axisnames=F)
96
97    # match actual bar coordinates with axis labels
98    barcoords <- cbind(barcoords, 0:(length(barcoords)-1))
99
100   # convert cell counts to bar coordinates
101   boxdata <- barcoords[match(segdata$nuclei[segdata$segmentID==
          seg], barcoords[,2]),1]
102
103   ## plot segment cell density boxplot
104
105   boxplot(boxdata, horizontal=T, axes=F, add=T)
106
107   seg.mean.cell <- mean(boxdata)
108
109   points(seg.mean.cell, 1, pch=15, col="red", cex=1.5)
110
111   ## plot lamellipodia histogram
112
113   par(fig=c(0, 1, 0.2, 1), new=T)  # x,x,y,y coords of
          histogram frame
114
115   barplot(hist.data, beside = TRUE, ylim=c(0,1),
116         names.arg = rownames(hist.data), cex.names = 1.5, cex.
              axis = 1.5, cex.lab=1.6,
117         ylab="proportion of total counts")
118
```

```
119    # add line showing predicted Poisson distribution
120
121    pois.predict <- dpois(x=barcoords[,2], lambda=mean.lam[seg])
122
123    lines(x=barcoords[,1], y=pois.predict, type="l", col="red",
          lwd=2)
124
125    # add legend
126
127    leg.seg <- CFV.match[seg]
128
129    leg.n <- paste("\n\nN =", num.seg[1,seg])
130
131    leg.mean <- paste("\n\u03BC", "=", round(mean.lam[seg],
          digits=2))
132
133    leg.var <- paste("\n\u03C3\u00B2 =", round(var.lam[seg],
          digits=2))
134
135    leg.x <- y.bound/2
136
137    legend(x=leg.x, y=1.3, bty="n",
138           legend=paste(leg.seg, leg.n, leg.mean, leg.var), cex
              =2.5)
139
140    dev.off() # save completed plot to file
141
142 }
```

A.6 R script for calculating Péclet-Damköhler ratio for flow experiments

The following script was used to calculate an estimate for the Péclet-Damköhler ratio for the flow experiments discussed in Chapter 5.

```
## Dimensions of Quasi-Vivo chamber as given in 2010-Mazzei,
   and modified to take into account micropattern substrate

QV.H.mm <- 9 # height in mm of internal Quasi-Vivo chamber (
   MCmB 2.0) between culture surface and inlet tube

QV.H2.mm <- 9-1 # height in mm of chamber between 1mm-thick
   glass micropattern substrate and inlet tube

QV.H2.um <- QV.H2.mm * 1000 # height in um of chamber between
   micropatterns on top of substrate and inlet tube


# Calculations below based on use of 160um-thick cover glass to
    culture cells (cf 1mm-thick substrate actually used)

# NB: calculations based on position ~0.84mm lower in chamber
   => underestimates both velocity and shear

QV.flow.rate.ul_min <- 3000 # Flow rate in ul/min

QV.velocity.m_s <- QV.flow.rate.ul_min * 2.6e-9 + 1.3e-7 # Flow
    speed experienced by cells in m/s (empirical; 2010-Mazzei)

QV.velocity.mm_s <- QV.velocity.m_s * 1000 # Flow speed
   experience by cells in mm/s

QV.shear.Pa <- QV.flow.rate.ul_min * 1.8e-8 + 1.1e-6 # Shear
   experienced by cells in Pa (empirical; 2010-Mazzei)

QV.shear.dyn_cm2 <- QV.shear.Pa * 10 # Shear experienced by
   cells in dyn/cm2


# Conservative estimate of FGF diffusivity used in 2011-
   Blagovic

FGF.DL.cm2_s <- 10^-6 # estimated diffusivity for FGF in cm2/s

```

```
29 FGF.DL.mm2_s <- FGF.DL.cm2_s * (10)^2 # estimated diffusivity
       for FGF in mm2/s
30
31 FGF.DL.um2_s <- FGF.DL.mm2_s * (1000)^2 # estimated diffusivity
        for FGF in um2/s
32
33
34 # Conservative binding constant for FGF used in 2011-Blagovic:
       ">2x higher than literature values"
35
36 FGF.kon_M_s <- 10^6 # estimated binding constant (kon) for FGF
       in M-1*s-1
37
38 FGF.kon.L_s <- FGF.kon_M_s / 6.022e23 # estimated binding
       constant (kon) for FGF in L*s-1/receptors
39
40 FGF.kon.m3_s <- FGF.kon.L_s * 0.001  # estimated binding
       constant (kon) for FGF in m3*s-1/receptors
41
42 FGF.kon.um3_s <- FGF.kon.m3_s * (1e6)^3 # estimated binding
       constant (kon) for FGF in um3*s-1/receptors
43
44
45 # Conservative estimate for FGF receptor cell density used in
       2011-Blagovic
46
47 FGF.R_um2 <- 10000 / (pi*10^2) # estimated FGF receptor density
        (assuming cell surface radius 10um) in receptors*um-2
48
49
50 # Calculations for Peclet number, Damkohler number, and ratio,
       with checks against calculations in 2011-Blagovic
51
52 Peclet <- (QV.velocity.mm_s * QV.H2.mm) / FGF.DL.mm2_s # (=634;
        will be higher, given velocity is an underestimate)
53
54 Peclet.Blagovic <- (0.03 * 0.25) / FGF.DL.mm2_s  # calculated
       as per 2011-Blagovic system (=75)
55
56
57 Damkohler <- (FGF.kon.um3_s * FGF.R_um2 * QV.H2.um) / FGF.DL.
       um2_s # (=4.2)
58
59 Damkohler.Blagovic <- (FGF.kon.um3_s * FGF.R_um2 * 250) / FGF.
       DL.um2_s  # calculated as per 2011-Blagovic system (=0.132)
60
```

```
61
62 Pec_Dam <- Peclet / Damkohler # (=150; will be higher, given
      Peclet number is an underestimate)
63
64 Pec_Dam.Blagovic <- Peclet.Blagovic / Damkohler.Blagovic #
      calculated as per 2011-Blagovic system (=568)
65
66
67 ## Conclusions: Peclet/Damkohler ratio is >>1, which suggests
      that the conditions used in the flow experiments
68 ## ... were sufficient to suppress any autocrine signaling
      involving diffusible cytokines
69
70
71 ## References:
72
73 # 2010-Mazzei
74 # Mazzei, D., Guzzardi, M. A., Giusti, S., & Ahluwalia, A.
      (2010).
75 # A low shear stress modular bioreactor for connected cell
      culture under high flow rates.
76 # Biotechnology and Bioengineering, 106(1), 127-137.
77 # PMID 20091740
78
79 # 2011-Blagovic
80 # Blagovic, K., Kim, L. Y., & Voldman, J. (2011).
81 # Microfluidic perfusion for regulating diffusible signaling in
       stem cells.
82 # PloS One, 6(8), e22892.
83 # PMID 21829665
```

A.7 R script for plotting drug data and generating results tables

The following R script was used to generate all plots and tables in Chapter 6.

```
## For analysing drug-treated scaffold protrusion rates.
## Produces the following for each drug:

## 1) barplot of mean segment length-normalised protrusion
##    rates for CTRL and drug-treated segments
##    with 95% confidence intervals generated using
##    bootstrapping and with significance stars representing
##    Mann-Whitney-W test p-values

## 2) barplot of ratios of mean segment length-normalised
##    protrusion rates (drug vs CTRL) with 95% confidence
##    intervals generated using an exact poisson rate ratio
##    test and with significance stars representing rate ratio
##    test p-values

## 3) table of general statistics (CTRL and drug data shown
##    separately) including confidence intervals

## 4) table of comparative statistics (difference and ratio of
##    length-normalised protrusion rates) including difference
##    in CTRL and drug mean values, Mann-Whitney-W test
##    p-values, the ratio of drug and CTRL values, and the
##    confidence interval and p-values from the rate ratio test


# load library: "Bootstrap resampling"
library(boot)

# load library: "Exact Rate Ratio Test Assuming Poisson Counts"
library(rateratio.test)

# get directory containing data
dir <- "C:/Users/Kim Martin/PhD thesis R analysis"

## create timestamped directory for output
tstamp <- paste("Drug analysis", format(Sys.time(),
                                        "%y%m%d%H%M%S"))
outdir <- paste(dir, tstamp, sep = "/")
dir.create(outdir)
setwd(outdir)
```

```
41
42
43 ## analyse data from each drug (control data from the same run)
44
45 all.drugs <- c("IONO", "BAPTA", "CYTOD", "BLEBB", "H1152")
46
47 for (drug in 1:length(all.drugs)) {
48
49   # select single drug for comparison
50
51   cf.drug <- all.drugs[drug]
52
53
54   ## prepare normalised data for single drug and matched
       control
55
56   # import data (protrusion counts, segment curvature & length
       measurements)
57
58   datafile <- paste(dir, "drug lam counts.csv", sep = "/")
59   prodata <- read.csv(file = datafile, header = T, na = "NA")
60
61   datafile <- paste(dir, "seg curve.csv", sep = "/")
62   curdata <- read.csv(file = datafile, header = T, na = "NA")
63
64   datafile <- paste(dir, "seg length.csv", sep = "/")
65   lendata <- read.csv(file = datafile, header = T, na = "NA")
66
67
68   # add CFV segment numbering (ordered by original segment
       number, 1-8)
69
70   CFV.match <- c("V2","C1","V3","F1","C3","V1","C2","F2")
71
72   for (seg in 1:8) {
73
74     prodata$segCFV[prodata$segmentID == seg] <- CFV.match[seg]
75   }
76
77   # reassign control labels
78
79   prodata$treatment <- as.character(prodata$treatment)
80
81   prodata$treatment[prodata$treatment=="DMSO"] <- "CTRL"
82
83
```

```
84  # omit NA and other experiments
85
86  prodata <- prodata[prodata$treatment==cf.drug | prodata$
       treatment=="CTRL", ]
87
88  prodata <- na.omit(prodata)
89
90
91  # omit control data from other runs
92
93  cf.runs <- unique(prodata$run[prodata$treatment==cf.drug])
94
95  run.check <- prodata$run %in% cf.runs
96
97  prodata <- prodata[run.check==T, ]
98
99
100 # ensure CTRL listed as first treatment factor for plotting
101
102 t.order <- unique(prodata$treatment)
103
104 if (match("CTRL", t.order)==2) {t.order <- rev(t.order)}
105
106 prodata$treatment <- factor(prodata$treatment,
107                             levels=t.order)
108
109
110 # add median segment curvature and length values
111
112 prodata$segcurve <- curdata$seg.curv.med[match(prodata$
       segmentID, curdata$seg.ID)]
113
114 prodata$seglen <- lendata$seg.len.med[match(prodata$segmentID
       , lendata$seg.ID)]
115
116
117 # calculate segment length-normalised protrusion rates (
       lamellipodia per um)
118
119 prodata$lamperum <- prodata$lamellipodia/prodata$seglen
120
121
122 ## calculate 95% confidence intervals for protrusion rates by
        bootstrapping
123
```

```
124  # specify function to find mean of a sample of data 'x' drawn
         using index 'd'
125
126  boot.mean <- function(x,d) {return(mean(x[d]))}
127
128
129  ## create vectors to hold calculated values of mean, std
        deviation, and 95%CI
130
131  # vector for segment ID (number 1-8):
132  segID <- vector()
133
134  # vector for mean normalised protrusion rate:
135  lamperum.mean <- vector()
136
137  # normalised protrusion rate standard deviation:
138  lamperum.sd <- vector()
139
140  # norm. protrusion rate 95% CI (upper bound):
141  lamperum.UCI <- vector()
142
143  # norm. protrusion rate 95% CI (lower bound):
144  lamperum.LCI <- vector()
145
146
147  ## first CTRL, then drug data - calculate values for each
        segment sequentially
148
149  for (t in 1:2) {
150
151    treat <- t.order[t]
152
153    for (seg in 1:8) {
154
155      # tsindex runs from 1-8 for CTRL data, and 9-16 for
           matched drug data
156
157      tsindex <- seg + (t-1)*8
158
159
160      # populate vectors with CTRL and drug values (mean, sd)
           and matching segment IDs
161
162      segID[tsindex] <- seg
163
```

```
164         lamperum.mean[tsindex] <- mean(prodata$lamperum[prodata$
               treatment==treat & prodata$segmentID==seg])
165
166         lamperum.sd[tsindex] <- sd(prodata$lamperum[prodata$
               treatment==treat & prodata$segmentID==seg])
167
168
169         # generate 1000x mean values for each segment using
               random sampling with replacement
170
171         bootobject <- boot(data=prodata$lamperum[prodata$
               treatment==treat & prodata$segmentID==seg], statistic=
               boot.mean, R=1000)
172
173
174         # populate vectors with CTRL and drug upper and lower 95%
                CI for means of normalised counts
175
176         mean.ci <- boot.ci(bootobject, type="basic")
177
178
179         # lower value of confidence intervals
180         lamperum.LCI[tsindex] <- mean.ci$basic[1,4]
181
182         # upper value of confidence intervals
183         lamperum.UCI[tsindex] <- mean.ci$basic[1,5]
184
185       }
186     }
187
188     # combine vectors as columns and split into two arrays, one
          for CTRL and one for drug
189
190     mean.data <- cbind(segID, lamperum.mean, lamperum.LCI,
          lamperum.UCI)
191
192     ctrl.results <- mean.data[1:8, ]
193     drug.results <- mean.data[9:16, ]
194
195
196     ## run Mann-Whitney-Wilcoxon test to compare CTRL and drug
          data by segment
197
198     # vector for p-values generated from MWW test
199     MWW.p <- vector()
200
```

```
201  # vector for number of significance stars (default to 0)
202  drug.s <- rep(0,8)
203
204
205  # for each segment, test null hypothesis of no effect of drug
         treatment
206
207  for (seg in 1:8) {
208
209    # get p-value from MWW test
210
211    MWW.p[seg] <- wilcox.test(lamperum ~ treatment, data=
           prodata[prodata$segmentID==seg,])$p.value
212
213
214    # get number of significance stars for plot
215
216    if (MWW.p[seg]<0.05) {drug.s[seg] <- 1}  # * => p < 0.05
217    if (MWW.p[seg]<0.01) {drug.s[seg] <- 2}  # ** => p < 0.01
218    if (MWW.p[seg]<0.001) {drug.s[seg] <- 3}  # *** => p <
           0.001
219  }
220
221  # combine results of MWW test with drug array from bootstrap
       for plotting
222
223  drug.results <- cbind(drug.results, MWW.p, drug.s)
224
225
226  ## barplot of length-normalised protrusion rates for CTRL and
         drug segments
227
228  png(paste(tstamp, " ", cf.drug, " lamperum.png", sep=""))
229
230  par(cex.axis=1.4, cex.lab=1.6)
231
232
233  # sort results by curvature (CFV number) and plot
234
235  ctrl.results <- ctrl.results[order(CFV.match),]
236  drug.results <- drug.results[order(CFV.match),]
237
238  bar.pos <- barplot(rbind(ctrl.results[,"lamperum.mean"],
239                           drug.results[,"lamperum.mean"]),
240                     col = c("blue", "red"),
241                     beside = TRUE, space = c(0, 1),
```

```
242                     xlab = "segments from concave to convex",
243                     ylab = "protrusions/segment length (um-1)"
                           ,
244                     ylim = c(0, 0.035),
245                     names.arg = sort(CFV.match))
246
247   abline(h=0)  # add horizontal line at y=0
248
249
250   # include 95% CI error bars
251
252   for (n in 1:8) {
253
254     arrows(bar.pos[, n],
255            rbind(ctrl.results[n, "lamperum.LCI"],
256                  drug.results[n, "lamperum.LCI"]),
257            bar.pos[, n],
258            rbind(ctrl.results[n, "lamperum.UCI"],
259                  drug.results[n, "lamperum.UCI"]),
260            length = 0.05, angle = 90, code = 3)
261   }
262
263   # include significance stars above drug results on bar plot
264
265   for (CFV in 1:8) {
266
267     # distance above bar / other star(s)
268     star.offset <- 0.0015
269
270     # position of drug bar (index for star x position)
271     drug.xpos <- bar.pos[2,CFV]
272
273     # height of highest confidence interval in drug-CTRL pair (
          index for star y position)
274     drug.ypos <- max(0, ctrl.results[CFV,"lamperum.UCI"], drug.
          results[CFV,"lamperum.UCI"])
275
276     # number of stars to be added
277     drug.stars <- drug.results[CFV,"drug.s"]
278
279     while (drug.stars!=0) {  # add stars sequentially
280
281       # calculate star y position
282       star.ypos <- drug.ypos + star.offset*drug.stars
283
284       # place star above and between bars
```

```
285         text(drug.xpos-0.5, star.ypos, "*", cex=3)
286
287         drug.stars <- drug.stars-1
288       }
289     }
290
291     # determine min and max number of segments counted for each
          treatment
292
293     # N CTRL segments analysed
294     n.ctrl <- table(prodata$segmentID[prodata$treatment==t.order
          [1]])
295
296     # N drug segments analysed
297     n.drug <- table(prodata$segmentID[prodata$treatment==t.order
          [2]])
298
299     legend.text.ctrl <- paste(t.order[1], " (N = ", min(n.ctrl),
          "-", max(n.ctrl), ")", sep="")
300     legend.text.drug <- paste(t.order[2], " (N = ", min(n.drug),
          "-", max(n.drug), ")", sep="")
301
302
303     # add legend with min and max segments for CTRL and drug
304
305     legend.text <- c(legend.text.ctrl, legend.text.drug)
306     legend("topleft", legend.text, pch=22, pt.bg=c("blue", "red")
          , pt.cex=1.5, cex=1.5, bty="n")
307
308     dev.off() # save completed plot to file
309
310
311     ## run poisson exact test on all drug-CTRL segment pairs
312
313     # vector for p-value (null hypothesis: rate ratio = 1)
314     rr.pval <- vector()
315
316     # vector for estimated rate ratio
317     rr.est <- vector()
318
319     # vector for estimated rate ratio 95% CI lower bound
320     rr.LCI <- vector()
321
322     # vector for estimated rate ratio 95% CI upper bound
323     rr.UCI <- vector()
324
```

```
325   # vector for p-value significance stars (default at 0)
326   rr.star <- rep(0,8)
327
328
329   # run Exact Poisson Rate Ratio test on drug-CTRL segment pair
330
331   for (seg in 1:8) {
332
333     # total number of protrusions counted in all segments
          included in analysis
334
335     drug.count <- sum(prodata$lamellipodia[prodata$treatment==
          cf.drug & prodata$segmentID==seg])
336
337     ctrl.count <- sum(prodata$lamellipodia[prodata$treatment=="
          CTRL" & prodata$segmentID==seg])
338
339
340     # total length of all segments included in analysis (
          equivalent to 'exposure'/'time at risk')
341
342     drug.exp <- sum(prodata$seglen[prodata$treatment==cf.drug &
           prodata$segmentID==seg])
343
344     ctrl.exp <- sum(prodata$seglen[prodata$treatment=="CTRL" &
          prodata$segmentID==seg])
345
346
347     # get results from rate ratio test
348
349     rr.test <- rateratio.test(c(drug.count, ctrl.count), c(drug
          .exp, ctrl.exp))
350
351     # rate ratio test p-value
352     rr.pval[seg] <- rr.test$p.value
353
354     # ratio of drug and CTRL values
355     rr.est[seg] <- rr.test$estimate[1]
356
357     # 95% confidence interval lower bound
358     rr.LCI[seg] <- rr.test$conf.int[1]
359
360     # 95% confidence interval upper bound
361     rr.UCI[seg] <- rr.test$conf.int[2]
362
363
```

```
364     # get number of significance stars for plot
365
366     if (rr.pval[seg]<0.05){rr.star[seg] <- 1}  # * => p < 0.05
367     if (rr.pval[seg]<0.01){rr.star[seg] <- 2}  # ** => p < 0.01
368     if (rr.pval[seg]<0.001){rr.star[seg] <- 3} # *** => p <
          0.001
369   }
370
371   # combine results of rate ratio test into array for plotting
372
373   rr.results <- cbind(1:8, rr.est, rr.LCI, rr.UCI, rr.pval, rr.
        star)
374
375
376   ## barplot of ratio of length-normalised protrusion rates (
        drug and CTRL)
377
378   png(paste(tstamp, " ", cf.drug, " rratio.png", sep=""))
379
380   par(cex.axis=1.4, cex.lab=1.6)
381
382
383   # sort results by curvature (CFV number) and plot
384
385   rr.results <- rr.results[order(CFV.match),]
386
387   bar.pos <- barplot(rr.results[,"rr.est"],
388                      beside = TRUE, space = 1,
389                      xlab = "segments from concave to convex",
390                      ylab = "protrusion rate ratio",
391                      ylim=c(0,5), names.arg = sort(CFV.match))
392
393   # add horizontal line at y=1 (indicating no difference
        between control and drug treatment)
394
395   abline(h=1, lty=2)
396
397   abline(h=0)  # add horizontal line at y=0 (base)
398
399
400   # include 95% CI error bars
401
402   for (n in 1:8) {
403
404     arrows(bar.pos[n], rr.results[n, "rr.LCI"],
405            bar.pos[n], rr.results[n, "rr.UCI"],
```

```
406             length = 0.05, angle = 90, code = 3)
407   }
408
409   # include significance stars above drug results on bar plot
410
411   for (CFV in 1:8) {
412
413     # distance above bar / other star(s)
414     star.offset <- 0.2
415
416     # position of drug bar (index for star x position)
417     bar.xpos <- bar.pos[CFV]
418
419     # highest confidence interval
420     bar.ypos <- max(0, rr.results[CFV,"rr.UCI"])
421
422     # number of stars to be added
423     sig.stars <- rr.results[CFV,"rr.star"]
424
425     while (sig.stars!=0) {  # add stars sequentially
426
427       # calculate star y position
428       star.ypos <- bar.ypos + star.offset*sig.stars
429
430       # place star above and between bars
431       text(bar.xpos, star.ypos, "*", cex=3)
432
433       sig.stars <- sig.stars-1
434     }
435   }
436
437   dev.off() # save completed plot to file
438
439
440   ## create general statistics table (protrusion rates in CTRL
        vs drug-treated segments)
441
442   # standard error of the mean (CTRL)
443   ctrl.SEM <- lamperum.sd[1:8]/sqrt(n.ctrl)
444
445   # assemble general statistics
446   gen.ctrl <- format(round(cbind(lamperum.mean[1:8],
447                                  lamperum.LCI[1:8],
448                                  lamperum.UCI[1:8],
449                                  ctrl.SEM),
450                            digits=4), scientific=F)
```

```
451
452   # label segments with no drug
453   gen.ctrl <- cbind(CFV.match, "(-)", n.ctrl, gen.ctrl)
454
455   # standard error of the mean (drug)
456   drug.SEM <- lamperum.sd[9:16]/sqrt(n.drug)
457
458   # assemble drug statistics
459   gen.drug <- format(round(cbind(lamperum.mean[9:16],
460                                  lamperum.LCI[9:16],
461                                  lamperum.UCI[9:16],
462                                  drug.SEM),
463                            digits=4), scientific=F)
464
465   # label segments with drug
466   gen.drug <- cbind(CFV.match, "(+)", n.drug, gen.drug)
467
468
469   # combine CTRL and drug statistics, assign column names, and
        order segments by curvature
470
471   gen.out <- rbind(gen.ctrl, gen.drug)
472
473   colnames(gen.out) <- c("Segment", "treat", "N", "Mean", "95%
        CIL", "95% CIU", "SEM")
474
475   gen.out <- gen.out[order(gen.out[,"Segment"],
476                            gen.out[,"treat"]), ]
477
478
479   # output table to file
480
481   write.csv(gen.out, file=paste(tstamp, " ", cf.drug, " general
          stats.csv", sep=""), row.names=FALSE)
482
483
484   ## create comparative statistics table (ratios of CTRL and
        drug protrusion rates)
485
486   # calculate difference in mean normalised protrusion rates
        for each segment
487
488   mean.diff <- format(round(lamperum.mean[9:16] - lamperum.mean
        [1:8], digits=4), scientific=F)
489
490
```

```
491   # add significance stars to Mann-Whitney-Wilcox p-value for
          table
492
493   MWW.ps <- format(round(MWW.p, digits=4), scientific=F)
494   MWW.ps[MWW.p<0.05] <- paste(MWW.ps[MWW.p<0.05], "*", sep="")
495   MWW.ps[MWW.p<0.01] <- paste(MWW.ps[MWW.p<0.01], "*", sep="")
496   MWW.ps[MWW.p<0.001] <- paste(MWW.ps[MWW.p<0.001], "*", sep=""
          )
497
498
499   # add significance stars to rate ratio p-value for table
500
501   rr.ps <- format(round(rr.pval, digits=4), scientific=F)
502   rr.ps[rr.pval<0.05] <- paste(rr.ps[rr.pval<0.05], "*", sep=""
          )
503   rr.ps[rr.pval<0.01] <- paste(rr.ps[rr.pval<0.01], "*", sep=""
          )
504   rr.ps[rr.pval<0.001] <- paste(rr.ps[rr.pval<0.001], "*", sep=
          "")
505
506
507   # combine table data and give column names
508
509   test.out <- format(round(cbind(rr.est, rr.LCI, rr.UCI),
          digits=2), scientific=F)
510
511   test.out <- cbind(CFV.match, mean.diff, MWW.ps, test.out, rr.
          ps)
512
513   colnames(test.out) <- c("Segment", "Diff.", "MWW p-value", "
          Rate ratio", "95% CIL", "95% CIU", "p-value")
514
515
516   # output table with rows in order of curvature (CFV number)
517
518   test.out <- test.out[order(test.out[,"Segment"]),]
519
520   write.csv(test.out, file=paste(tstamp, " ", cf.drug, " ratio
          stats.csv", sep=""), row.names=FALSE)
521
522 }
```

A.8 Journal of Anatomy publication

The manuscript on the following pages, which presents the results from Chapter 5, has been accepted for publication in the Journal of Anatomy (DOI:10.1111/joa.12599; currently pre-proof; article accepted on 16 January, 2017):

Symmetry-breaking in branching epithelia: cells on micro-patterns under flow challenge the hypothesis of positive feedback by a secreted autocrine inhibitor of motility.

Kimberly C. Martin, Xiaofei Yuan, Gregory Stimac, Kieran Bannerman, Jamie Anderson, Chloe Roy, Fokion Glykofrydis, Huabing Yin and Jamie A. Davies.

Abstract

Branching morphogenesis of epithelia involves division of cells into leader (tip) and follower (stalk) cells. Published work on cell lines in culture has suggested that symmetry breaking takes place via a secreted autocrine inhibitor of motility, the inhibitor accumulating more in concave regions of the culture boundary, slowing advance of cells there, and less in convex areas, allowing advance and a further exaggeration of the concave/ convex difference. Here we test this hypothesis using a 2D culture system that includes strong flow conditions to remove accumulating diffusible secretions. We find that, while motility does indeed follow boundary curvature in this system, flow makes no difference: this challenges the hypothesis of control by a diffusible secreted autocrine inhibitor.

Keywords

Branching morphogenesis, self-organization, positive feedback, autocrine secretion, cell motility, shape.

Introduction

In this report, we test a prediction based on a published hypothesis about epithelial symmetry-breaking and, by showing that the prediction is not met in a 2-dimensional system using renal cells, it casts doubt on the universal validity of that hypothesis.

The anatomy of many internal organs is based on the structure of a system of branched epithelial tubes; examples include the airways of the lungs, the urinary collecting ducts of the kidneys, the exocrine ducts of the pancreas and the tubule systems of the salivary, mammary, and uterine glands (reviewed by Iber and Menshykau, 2013). The growth of these tubes relies on the cells at the branch tip advancing through the surrounding matrix or mesenchyme and the creation of new branches depends either on the tip region splitting or, for lateral branching, on a new tip region forming from the side of a stalk. Both mechanisms of new branch formation can be seen in the same developing tree (Watanabe and Costantini, 2004). The differing behaviour of invasive tip cells and non-invasive stalk cells is a feature of the more general phenomenon of collective cell migration (Khalil and Friedl, 2010). This is characterised by the emergence of specialised 'leader' cells, which are characterised by a highly migratory phenotype, and associated with large traction forces exerted against the underlying substrate (Reffay et al., 2014). In contrast, the 'follower' cells appear to be dragged passively behind the leader, although it has been shown that they extend protrusions under the cells in front of them, in a sign of active crawling (Farooqui and Fenteany, 2005).

In general, tip and stalk cells develop from the same starting population as when, for example, the lung bud develops from the foregut wall or the ureteric bud develops from the wall of the nephric duct, both probably in response to inductive signals from nearby tissues (Warburton et al., 2010; Woolf and Davies, 2013). Spontaneous branching morphogenesis can also be observed, however, when clones of epithelial cells are grown in simple 2D and 3D cultures with no pre-existing asymmetries, showing self-organized symmetry-breaking into tips and non-tips to be an innate property of these cells (Barros et al., 1995; Sakurai et al., 1997). Recent experimental work with cells in culture has directed increasing attention towards parameters such as cell shape as being a potential factor in directing symmetry-breaking of leaders and followers (Mark et al., 2010). Cells constrained by culture on two-dimensional scaffolds, as well as in three-dimensional shapes, appear to respond to convex curves with an increasing propensity to protrude, while concave curves in contrast appear to inhibit protrusion.

These responses can be shown to be proportional to the radius of curvature, which has interesting implications in terms of a potential positive feedback loop involved in symmetry-

breaking (through amplification of initial stochastic differences in cell shape) and in collective migration-based developmental processes (through reinforcing and directing coherent movement of the collectives) (Mark et al., 2010; Davies, 2013). It should be stressed that there are theoretical arguments against curvature-dependent protrusion being the only determinant of branching morphogenesis of tubules such as those in kidney and lung, because it cannot itself promote stable bifurcation (Menshykau et al., 2014): it is being studied by us, and by others, as one aspect of the behaviour of collecting cell migration not as a sole explanation of every aspect.

The curvature-protrusion feedback model was proposed based on observations of epithelial cells in a culture system that confined them behind a boundary between adhesive and non-adhesive substrates but that allowed the non-adhesive substrate to be removed rapidly to create new and unoccupied territory for the cells to invade. The cells along the released boundary did not advance as a line, but broke symmetry and formed finger-like shapes with leader cells directing cohorts of followers (Poujade et al., 2007).

Micro-patterning groups of cells in three dimensions (3D) has led to one hypothesis of the underlying mechanism for the relationship. Nelson and colleagues used a micro-fabricated mould to create wells of defined geometry in collagen gel, allowing them to generate precisely-defined double-layered tubules consisting of mammary myoepithelial and luminal epithelial cells. When stimulated with appropriate global cytokines, these tubules branched into the surrounding collagen. Shaped wells showed that branching was inhibited at concave regions, and promoted at convex regions (Nelson et al., 2006): see Fig S4 for a schematic. The authors hypothesized that the position-dependence of the branch initiation was due to the relative concentration of an autocrine inhibitor secreted by the cells. With secretion rate constant, the greater space available at convex curves would be expected to result in a lower relative concentration, with converse being true at concave curves. Mathematical simulation supported the idea and further evidence for this ‘autocrine inhibitor accumulation’ hypothesis came from the use of paired wells, each a rectangle with rounded ends, placed in tandem about 30 μm apart (see Figure 3 in Nelson et al., 2006, and our FigS4 for a summary). In this arrangement, the curvatures of all of the well ends were the same but the inner ends were predicted to experience more secreted autocrine inhibitor as cells in both the wells contributed to its accumulation in that area. Cells showed much more motility at the outer ends of the wells than the inner ends, suggesting that motility is controlled by a secreted inhibitor rather than directly by curvature. The separation between the wells, about 30 μm apart, was small enough that inhibitor could accumulate but large enough to make direct contact inhibition of locomotion unlikely: images of cells stained for actin in Fig 2 of the same paper show no evidence of cellular processes capable of spanning such a gap. TGFb1 was suggested as a candidate for

the secreted inhibitor and inhibiting TGFb1 signalling abolished the relationship between well shape and motility. The system did not, though, permit a direct test that differential accumulation (rather than simple presence) of TGFb1 was critical, and it remained formally possible that a different molecule was the regulator that linked well shape to motility.

We have recently shown the secreted autocrine signal, BMP7, to be important in the large-scale patterning of the renal collecting duct tree. The tips of growing branches avoid colliding with existing branches even if set up in multi-tree culture conditions that might be expected to cause collisions, and a combination of inhibitor, BMP7-secreting bead, and trans-filter gradient experiments, suggest that this mutual avoidance is due to tips secreting BMP7 and avoiding areas of highest BMP7 intensity: when the signalling system is inhibited branches can run parallel and collide instead of diverging to form a spread tree (Davies et al., 2014). We therefore sought to determine whether this signal was related to leader/ follower symmetry-breaking signals, and developed a 2D micro-pattern culture system to (i) verify that renal epithelial cells replicate the relationship between curvature and protrusion observed in other cells; (ii) to test that this was due to accumulation of an autocrine inhibitor; and (iii) to test whether that inhibitor was the same one, BMP7, implicated in large-scale patterning of branched renal epithelia.

Methods

LifeAct-MDCK cells

The MDCK II cells used in this study were obtained from the European Collection of Cell Cultures (ECACC; cat. 00062107; lot 10D039) at passage 28. They were modified to constitutively express the live actin-marker 'Lifeact-GFP' (Riedl et al., 2008). The expression vector pEGFP-N1-Lifeact was a kind gift from Dr Tim Czopka at the University of Edinburgh. The cells were cultured at 37ºC and 5% CO_2 in Minimum Essential Medium Eagle (MEM; Sigma, M5650) supplemented with 2mM L-glutamine (Gibco, 25030–024), 100U penicillin/streptomycin (Gibco, 15140), and 5% fetal calf serum (Invitrogen, 10108165).

Variable-curvature micropatterns

Micro-patterned substrates, consisting of an amino-terminated adhesion-permissive substrate (APTES; Sigma-Aldrich) surrounded by an adhesion-resistant substrate (PEG-silane; Gelest), were prepared on glass slides as previously described (Yuan et al., 2015). One day after their last passage, cells were suspended at $2.25x10^5$ cells per ml and 4ml of the suspension was placed in the well of a 6-well plate, at the bottom of which was a $1cm^2$ glass plate carrying the micro-patterns, for 2h at 37ºC. Plates were washed twice with warm PBS, then placed in culture medium.

Quasi-Vivo flow culture

Flow experiments were conducted using a Quasi-Vivo QV500 chamber system (Kirkstall) with a peristaltic pump (EP–1, Bio-Rad). Two flow chambers were set up in series, as per the QV500 user manual (Issue Number 3.0), and the volume flow rate through the entire system was measured at 3 ml/min. Prior to placing micropatterned cells in the flow chambers, the system was washed with PBS, and then primed with warm complete media. Micro-patterns were placed facing upwards, narrow end towards the inlet, and flow was maintained for 1.5h. Control and flow-treated cells were kept in the same incubator for the duration of the treatment.

Imaging

Live imaging was conducted using a heated on-stage chamber, gassed with warmed, humidified air containing 5% CO_2, on an inverted microscope. For imaging of fixed cells, culture plates were washed briefly with warm FCS-free media, then fixed in 4% formaldehyde (PFA) at room temperature for a minimum of 30 minutes prior to imaging. Images were captured using a Zeiss AxioImager D1 (inverted) fluorescence microscope equipped with an AxioCam MRm camera and a GFP filter (excitation 470/40; emission 525/50). The 10x

objective allowed the maximum number of patterns to be captured in each image, while still giving sufficient resolution for counting protrusions.

Image analysis.

The boundary of the micro-pattern was considered to be divided into distinct segments, defined by points of inflection around the edge of the micropattern, and ImageJ was used to manually delineate each segment, ignoring protrusions (Fig. 1A). Length measurements were taken directly, and then ImageJ's 'Fit Circle' function was used to measure the radius of curvature for each segment - defined as the radius of the circle that fits the curve (Fig. 1B-C). Curvature was calculated as radius^{-1}, and assigned a negative value for concave curves, and a value of 0 for flat sections (equivalent to a circle with an infinite radius). Measurements were made in pixels and converted into μm based on measurement of a scale bar supplied by the microscope software. Segment curvature and length from measurements of 10 independent micro-patterns are shown in Fig. 1D-E.

For image analysis of samples, segments were included in the analysis if the full length of the segment edge conformed to the expected shape of the micropattern and was visible for assessment for protrusions; for example, segments were ignored when debris or cells that were in the process of being extruded had adhered to cells at the segment edge, potentially concealing protrusions, or if cells had migrated outside the borders of the micro-pattern. Actin-containing regions that extended outside the recognisable shape of the variable-curvature micropattern (beyond the smooth edges defined by the adherent cells) were considered to be protrusions, and where protrusions formed from adjacent cells, they were counted separately.

Statistical analysis

Wilcoxon's signed-rank test (implemented using the 'wilcox.test' function in R) was used to calculate p-values for differences between protrusion rates (protrusion counts normalised by segment length) between segments (Crawley, 2007). Confidence intervals for protrusion rates at each segment were calculated by bootstrapping (sampling with replacement 1000 times), using the R 'boot' package. An Exact Poisson rate ratio test (implemented using the 'rateratio.test' R package contributed by Michael Fay) was used as an additional test of the significance of relative differences between protrusion rates, and to calculate confidence intervals for protrusion rate ratios. Tables of statistics plotted in the figures here are available as supplementary data (Fig S1, S2).

Data archive

Images and analysis spreadsheets are available on Edinburgh University's DataShare server: http://datashare.is.ed.ac.uk/handle/10283/2348

Results

MDCK cells remain confined to patterned substrates but extend lamellipodia dynamically beyond their boundaries.

Time-lapse observation of Lifeact-MDCK cells, seeded on micropatterns, revealed that most cells remained confined to the micropattern but showed dynamic extension of lamellipodia on to the non-adhesive substrate. A series of images captured every two minutes (Fig. 2) showed actin-rich processes protruding from the cells. These processes typically had the irregular border and feathery appearance of lamellipodia, which have been observed by previous authors to extend over non-adhesive surfaces, as well as in the presence of adhesion-blocking peptides (Bailly et al., 1998). In addition to producing lamellipodia, cells sometimes produced narrow spike-like, and broader-based triangular protrusions, apparently as transition phases during the establishment and retraction of broad lamellipodia.

Live imaging of the micropatterned Lifeact-MDCK also enabled limited observation of actin-based dynamics on the apical surfaces of cells. This surface showed ruffles, which are folds in the surface of cells associated with compacted actin that move centripetally from the cell periphery and are associated with frustrated adhesion of motile cells (Borm et al., 2005; Giannone et al., 2007; Okeyo et al., 2011). One representative ruffle is highlighted in Fig 3.

Overall, the behaviour of the cells, in remaining fixed while extending structures associated with motility over their non-adhesive surroundings, suggested that this system would be suitable for study of the relationship between cell curvature and attempted motility.

Frequency of protrusion is a function of curvature.

In order to test the hypothesis that protrusive activity would be linked to curvature in our system, Lifeact-MDCK cells were seeded on micro-patterns, cultured for 24 hours and fixed. The frequency of lamellipodial protrusion was determined for each segment of each micro-pattern. The whole experiment was performed three times, each time including many micro-patterns, so that each segment was analysed on a minimum of 483 individual micro-patterns. As a basic statistical check that cells in each segment were behaving independently, the frequency of zero, one, two and more protrusions was compared to a Poisson distribution, and showed a good fit for all segments (Fig S2). In addition, variance values were approximately equal to the mean as expected for such a distribution (Crawley, 2007).

When the frequency of protrusions per unit length of segment was plotted against curvature, a strong trend emerged (Fig. 4). Flat segments showed modest protrusion. Segments of increasing convexity showed a marked elevation of the frequency of lamellipodial protrusion ($p < 0.001$). Concave segments, on the other hand, generally showed less protrusion then flat ($p < 0.001$) although the most concave segment C1 was an exception, showing rates of protrusion similar to flat segments. It is clear that, in general, there is a strong relationship between curvature and protrusion, with more convex segments having higher protrusion rates. These results confirm in our system the observations of other researchers (Nelson et al., 2006; Mark et al., 2010) in other systems, and validate the use of our micro-patterns as a platform for further investigation of the underlying mechanism that couples curvature with motile response.

The curvature-motility relationship is unaffected by medium flow

One potential explanation for the relationship between protrusion and curvature, at least in three-dimensional, matrix-embedded multicellular collectives, involves the secretion of a diffusible autocrine inhibitor of protrusion (Nelson et al., 2006). In this model, cells present at convex curves experience a lower concentration of diffusing inhibitor, while those at concave curves experience a higher concentration as the inhibitor accumulates in zones partially surrounded by cells. While the authors were able to provide some convincing support for their model, and subsequent work has suggested a role for autocrine inhibitor secretion in patterning branching morphogenesis of the renal collecting duct system (Davies et al., 2014), it remained unclear whether this proposed mechanism could explain the relationship between curvature and protrusion seen in a two-dimensional, matrix-free system. It should be noted that the ratio of protein diffusion constants in free solution and in collagen gels is only around 1.3 : 1 (Galgoczy et al., 2014), so accumulation of secreted proteins does not depend on presence of a 3D gel.

Whereas Nelson et al. were able to support the likely role of an autocrine inhibitor by targeting a particular cytokine, TGFb1, in their mammary cell system, TGFb1 has been shown to have a positive rather than negative effect on motility in the MDCK II cell line (Peinado et al., 2003). As an alternative to taking a targeted approach that would involve identifying candidate inhibitors, a blanket approach was taken initially: using rapid flow of culture medium to interfere with the accumulation of any autocrine signalling molecules. This approach has been used to demonstrate perturbation of other aspects of autocrine signalling in cultured cells (Blagovic et al., 2011). Removal of diffusible inhibitor would be expected to have two effects; an overall increase in protrusion (as there is less inhibitor experienced by all cells) and

reduction or abolition, if the flushing were perfectly efficient, of the difference between protrusion rates in concave and convex areas.

The use of flow for this purpose depends on choosing a flow rate adequate to disrupt accumulation of secreted molecules but not so strong that cells are subjected to shear stress. Calculations using the formulae of Blagovic et al. (2011), the dimensions of the Kirkstall Quasi-Vivo perfusion chamber used here, and a flow rate of 3ml/ml suggests that the effect of flow should massively overwhelm the effects of diffusion on the distribution of molecules (see Fig S3 for the calculations and Fig S5 for an empirical demonstration that flow does indeed flush proteins away). The Quasi-Vivo perfusion culture chamber used here was developed by Ahluwalia and colleagues specifically to minimise shear stress experienced while maximising mass transport (Sbrana and Ahluwalia, 2012). Its use has been successfully demonstrated with 'difficult' shear-sensitive, metabolically-demanding primary hepatocytes; maintaining viability and liver-specific function (Mazzei et al., 2010). At the flow rate of 3ml/ min, the expected shear stress to which cells will be subjected can be calculated, by the equations in Mazzei et al., 2010, to be less than 0.0005 Pa, far less than the shear stress of 0.054 Pa that is known to have only a very limited effect on MDCK cells, even after extended exposure (Wang et al., 2010). The benign nature of this flow was supported by our observing no changes in viability, proliferation rates or morphology of MDCK II cells cultured on patterned substrates under these flow conditions for 12h: they were indistinguishable from controls.

To test the hypothesis that flow would, by removing accumulated autocrine molecules, abolish the relationship between curvature and motility, MDCK II cells on micro-patterns were placed in the Quasi-Vivo flow chamber with long axis of the pattern parallel to the direction of flow, pointing upstream.

Counting protrusions in flow-treated micro-pattern segments and plotting protrusion frequency per unit length showed that the relationship between curvature and protrusion was unchanged by exposure to flow (Fig. 5). Concave (C) and flat (F) segments had low protrusion rates, and convex (V) segments showed a positive relationship between curvature and protrusion rate. There was also no general trend of increased protrusion rates at all segments, as would be expected if an inhibitor were usually present and were now washed away by the flow.

Comparing protrusion rates in control and flow-treated micropatterns for each segment did show small differences at some segments. Flow-treated micropatterns showed a slight increase at both flat segments (F1 and F2) and at one of the concave segments (C3), as well as a slight decrease at the most convex segment (V3); see Figure 5. While the increases at C3, F1, and F2 might suggest that the concentration of an autocrine inhibitor is being reduced,

this conclusion is challenged by the lack of significant change at ‘upstream’ segment C1 in particular, as well as by the decrease in the protrusion rate at ‘upstream’ segment V3. It was concluded that the differences in protrusion rates were too small to indicate a meaningful effect of flow treatment.

Conclusions

Our results demonstrate that MDCK-II cells show the relationship between curvature and motile activity that can be expected from published observations of other cell types (Nelson et al., 2006; Poujade et al., 2007). Concave boundaries show little protrusive activity while convex ones show more; much more if the convex curvature has a small radius. That pattern would be compatible with the idea of control of curvature by a secreted autocrine inhibitor. If this hypothesis were correct, one would expect that washing the inhibitor away with a strong flow of medium would release all cells from the inhibition, and the relationship between curvature and protrusion would be lost. What is more, one would expect all segments now to show protrusion rates higher than that of the highest rate observed in non-flowing medium. This did not happen: instead, when the culture system was placed under conditions of strong flow, nothing changed.

The obvious conclusion to be drawn is that the curvature-protrusion relationship in this 2D system does not in fact rely on secretion and accumulation of a diffusible inhibitor of motility. The robustness of that conclusion depends on the confidence we can have that conditions of flow were adequate to eliminate or at least severely reduce curvature-controlling accumulations of the secreted molecule. We argue on two grounds that reasonable confidence can be placed in this. The first is the series of calculations made using published equations developed for this exact equipment (Mazzei et al., 2010): our calculations are presented in detail in Fig. S3. They show that the flow rates would be adequate by a very large margin. The second is the quantitative comparison between the behaviour of cells with and without flow. If our calculations were wrong and flow were adequate to remove only some of the inhibitor, leaving enough behind to affect cells, then one would at least expect to see the incidence of protrusion to increase, quantitatively, throughout as some inhibitor is lost, even if a relationship between curvature and protrusion were maintained. This did not occur: flow made no difference.

How else might the relationship between curvature and protrusion arise? One possible mechanism is tension-mediated activation of motility. Tension in the membrane and its associated cytoskeleton will be highest where the membrane is bent around a convex curve and lowest along a concave curve: the correlation between cytoskeletal tension against the substrate, and motility, has been measured directly in MDCK cells on 2D patterned substrates (Rausch et al., 2013). A variety of experiments, in systems as diverse as *C. elegans* sperm, COS1 cells, and MDCK cells as used here, has shown that high membrane tension encourages production of a motile process whereas reduced tension inhibits it (Batchelder et al., 2011; Tsujita et al., 2015; Rausch et al., 2013).

Finally, how can the results presented here be reconciled with those of Nelson et al. (2006), who showed the behaviour of mammary cells in tandem-array 3D wells could be explained by the secreted inhibitor model but not by direct curvature? There are two obvious possibilities: the first is that mechanisms of symmetry breaking are organ-specific rather than universal, and that mammary gland uses a secreted inhibitor whereas the kidney uses direct sensing of curvature. The second possibility is that symmetry-breaking in 2D systems is very different from 3D because epithelial cells have a different polarity. In 2D culture, the epithelial sheet is discontinuous, ending at the edges of the micro-pattern, and the basal surfaces of the cells face the substrate rather than the space into which cells might travel. In 3D culture, the epithelium is continuous without free lateral edges, and the basal surface of the cells faces the gel into which cells might travel. It might be that the edge-effect present in 2D culture allows curvature to exert such a dominant influence that variations in the concentration of a secreted inhibitor are irrelevant to cell behaviour whereas, without edge effects, 3D culture allows the secreted molecule to exert control. These questions could perhaps be explored by using a range of cell types from different organs in both the 2D and 3D systems.

Acknowledgements

While doing this work, KCM was supported by an Anatomical Society Studentship and some experiments were supported by BBSRC grant Bb/M018040/1. We thank Melanie Lawrence for her helpful comments on draft versions of this manuscript.

Author contributions

K.C.M. performed the experiments that produced the data presented here and produced the first draft of the manuscript; G.S., K.B., J.A., and C.R. were project students who performed pilot studies critical to the eventual experimental design; X.Y. produced the micro-patterns under the supervision of H.Y.; J.A.D. conceived and supervised the study and contributed to writing the manuscript. No authors have any conflict of interest.

References

Bailly, M., Yan, L., Whitesides, G. M., Condeelis, J. S., and Segall, J. E. (1998). Regulation of protrusion shape and adhesion to the substratum during chemotactic responses of mammalian carcinoma cells. *Experimental Cell Research*, 241(2):285–99.

Barros, E. J., Santos, O. F., Matsumoto, K., Nakamura, T., Nigam, S.K. (1995). Differential tubulogenic and branching morphogenetic activities of growth factors: implications for epithelial tissue development. *Proc Natl Acad Sci U S A*. 92(10):4412-6.

Batchelder, E.L., Hollopeter, G., Campillo, C., Mezanges, X., Jorgensen, E.M., Nassoy, P., Sens, P., and Plastino, J. (2011) Membrane tension regulates motility by controlling lamellipodium organization. *Proc Natl Acad Sci U S A*. 108: 11429-11434.

Blagovic, K., Kim, L. Y., and Voldman, J. (2011). Microfluidic perfusion for regulating diffusible signaling in stem cells. *PloS ONE*, 6(8):e22892.

Borm, B., Requardt, R. P., Herzog, V., and Kirfel, G. (2005). Membrane ruffles in cell migration: Indicators of inefficient lamellipodia adhesion and compartments of actin filament reorganization. *Experimental Cell Research*, 302(1):83–95.

Crawley, M. J. (2007). *The R Book*. Wiley, Chichester, England.

Davies, J. A. (2013). *Mechanisms of Morphogenesis*. Academic Press, London, 2nd edition.

Davies, J. A., Hohenstein, P., Chang, C.-H., and Berry, R. (2014). A self-avoidance mechanism in patterning of the urinary collecting duct tree. *BMC Developmental Biology*, 14(1):1–12.

Farooqui, R. and Fenteany, G. (2005). Multiple rows of cells behind an epithelial wound edge ex-tend cryptic lamellipodia to collectively drive cell-sheet movement. *Journal of Cell Science*, 118(Pt 1):51–63.

Galgoczy, R., Pastor, I., Colom, A., Giménez, A., Mas, F., and Alcaraz, J. (2014). A spectrophotometer-based diffusivity assay reveals that diffusion hindrance of small molecules in extracellular matrix gels used in 3D cultures is dominated by viscous effects. *Colloids Surf B Biointerfaces.* 120:200-207.

Giannone, G., Dubin-Thaler, B. J., Rossier, O., Cai, Y., Chaga, O., Jiang, G., Beaver, W., Döbereiner, H.-G., Freund, Y., Borisy, G., and Sheetz, M. P. (2007). Lamellipodial actin mechanically links myosin activity with adhesion-site formation. *Cell*, 128(3):561–75.

Iber, D., Menshykau, D. (2013). The control of branching morphogenesis. *Open Biol*. 3(9):130088.

Ireland, G.W., Dopping-Hepenstal, P., Jordan, P., O'Neill, C. (1987) Effect of patterned surfaces of adhesive islands on the shape, cytoskeleton, adhesion and behaviour of Swiss mouse 3T3 fibroblasts. J Cell Sci Suppl. 8:19-33.

Khalil, A. A. and Friedl, P. (2010). Determinants of leader cells in collective cell migration. *Integrative Biology*, 2(11-12):568–74.

Mark, S., Shlomovitz, R., Gov, N. S., Poujade, M., Grasland-Mongrain, E., and Silberzan, P. (2010). Physical model of the dynamic instability in an expanding cell culture. *Biophysical Journal*, 98(3):361–70.

Mazzei, D., Guzzardi, M. A., Giusti, S., and Ahluwalia, A. (2010). A low shear stress modular bioreactor for connected cell culture under high flow rates. *Biotechnology and Bioengineering*, 106(1):127–137.

Menshykau, D., Blanc, P., Unal, E., Sapin, V. and Iber D. (2014) An interplay of geometry and signaling enables robust lung branching morphogenesis. Development. 141(23):4526-36.

Nelson, C. M., Vanduijn, M. M., Inman, J. L., Fletcher, D. A., and Bissell, M. J. (2006). Tissue geometry determines sites of mammary branching morphogenesis in organotypic cultures. *Science (New York, N.Y.)*, 314(5797):298–300.

Okeyo, K. O., Nagasaki, M., Sunaga, J., Hojo, M., Kotera, H., and Adachi, T. (2011). Effect of acto-myosin contractility on lamellipodial protrusion dynamics on a micropatterned substrate. *Cellular and Molecular Bioengineering*, 4(3):389–398.

O'Neill, C., Jordan, P., Riddle, P., Ireland, G. (1990) Narrow linear strips of adhesive substratum are powerful inducers of both growth and total focal contact area. J Cell Sci. 95: 577-586.

Peinado, H., Quintanilla, M., and Cano, A. (2003). Transforming growth factor beta-1 induces snail transcription factor in epithelial cell lines: mechanisms for epithelial mesenchymal transitions. *The Journal of Biological Chemistry*, 278(23):21113–23.

Poujade,M., Grasland-Mongrain, E., Hertzog, A., Jouanneau, J., Chavrier, P., Ladoux, B., Buguin, A., and Silberzan, P. (2007). Collective migration of an epithelial monolayer in response to a model wound. *Proceedings of the National Academy of Sciences of the United States of America*, 104(41):15988–93.

Rausch, S., Das, T., Soiné, J.R., Hofmann, T.W., Boehm, C.H., Schwarz, U.S., Boehm, H., and Spatz, J.P. (2013) Polarizing cytoskeletal tension to induce leader cell formation during collective cell migration. Biointerphases. 8: 32. doi: 10.1186/1559-4106-8-32

Reffay, M., Parrini, M. C., Cochet-Escartin, O., Ladoux, B., Buguin, A., Coscoy, S., Amblard, F., Camonis, J., and Silberzan, P. (2014). Interplay of RhoA and mechanical forces in collective cell migration driven by leader cells. *Nature Cell Biology*, 16(3).

Riedl, J., Crevenna, A. H., Kessenbrock, K., Yu, J. H., Bista, M., Bradke, F., Jenne, D., Holak, T. A., Werb, Z., Sixt, M., Wedlich-Soldner, R., Klopferspitz, A., Avenue, P., Francisco, S., Neukirchen, D., Bista, M., Bradke, F., Jenne, D., Holak, T. A., Werb, Z., Sixt, M., Wedlich-Soldner, R., Klopferspitz, A., Avenue, P., and Francisco, S. (2008). Lifeact: a versatile marker to visualize F-actin. *Nature Methods*, 5(7):605–7.

Sakurai, H., Barros, E. J., Tsukamoto, T., Barasch, J. and Nigam, S. K. (1997) An in vitro tubulogenesis system using cell lines derived from the embryonic kidney shows dependence on multiple soluble growth factors. *Proc Natl Acad Sci U S A.* 94(12):6279-84.

Sbrana, T. and Ahluwalia, A. (2012). Engineering Quasi-Vivo in vitro organ models. In Balls, M., Combes, R. D., and Bhogal, N., editors, *New Technologies for Toxicity Testing*, volume 745 of the, pages 138–53. Springer US.

Tsujita, K., Takenawa, T., and Itoh, T. (2015) Feedback regulation between plasma membrane tension and membrane-bending proteins organizes cell polarity during leading edge formation. *Nat Cell Biol*. 17: 749-58.

Wang, J., Heo, J., and Hua, S. Z. (2010). Spatially resolved shear distribution in microfluidic chip for studying force transduction mechanisms in cells. *Lab on a Chip*, 10(2):235–9.

Watanabe, T., and Costantini, F. (2004). Real-time analysis of ureteric bud branching morphogenesis in vitro. *Dev Biol*. 271: 98-108.

Warburton, D., El-Hashash, A., Carraro, G., Tiozzo, C., Sala, F., Rogers, O., De Langhe, S., Kemp, P. J., Riccardi, D., Torday, J., Bellusci, S., Shi, W., Lubkin, S. R.,and Jesudason, E. (2010). Lung organogenesis. *Curr Top Dev Biol.* 90:73-158.

Woolf, A. S. and Davies, J. A. (2013) Cell biology of ureter development. *J Am Soc Nephrol.* 24(1):19-25.

Yuan, X., Zhou, M., Gough, J., Glidle, A., and Yin, H. (2015). A novel culture system for modulating single cell geometry in 3D. *Acta Biomaterialia*, 24:228–240.

Figure legends

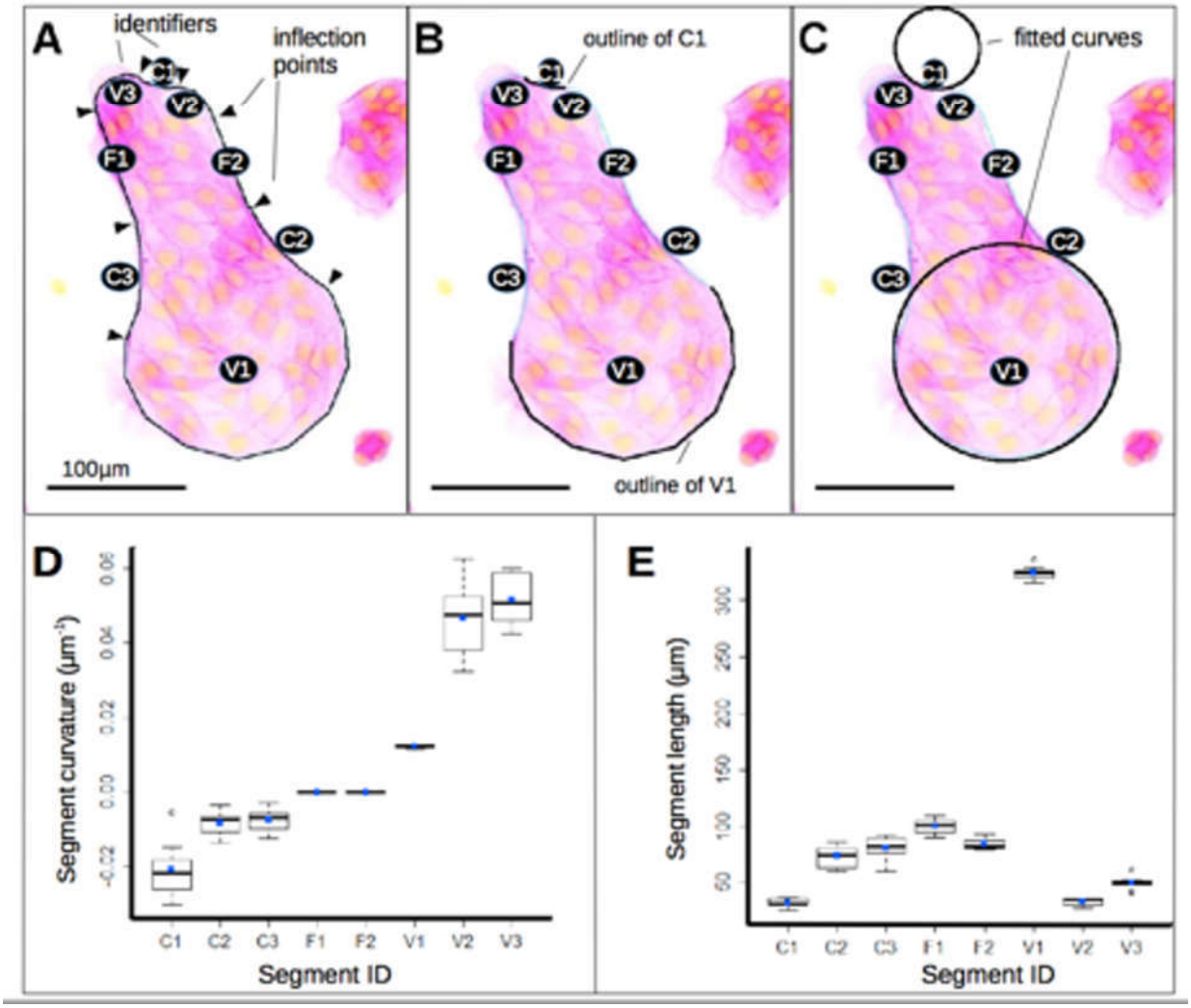

Figure 1: shape and segmentation of micro-pattern boundaries. All three images show a typical view of cells growing on one micro-pattern, the original green-on-black fluorescence image being inverted with respect to colours to become magenta on white for ease of labelling. (A) shows the position of points of inflection (arrow-heads) of the curved micro-pattern periphery (when any temporary lamellipodial extensions cells are making are ignored). The regions between these points of inflection are considered to be segments of the shape and are labelled C1-3 for concave areas, F1-2 for flat and V1-3 for convex. (B) highlights the periphery of just two segments (C1 and V1) and (C) shows circles fitted to these using ImageJ's 'Fit Curve' function: the radii of these circles were used to calculate the curvature of each segment (D). (E) shows the length of each segment, used in the analyses to normalize protrusion frequency as protrusions-per-unit-length.

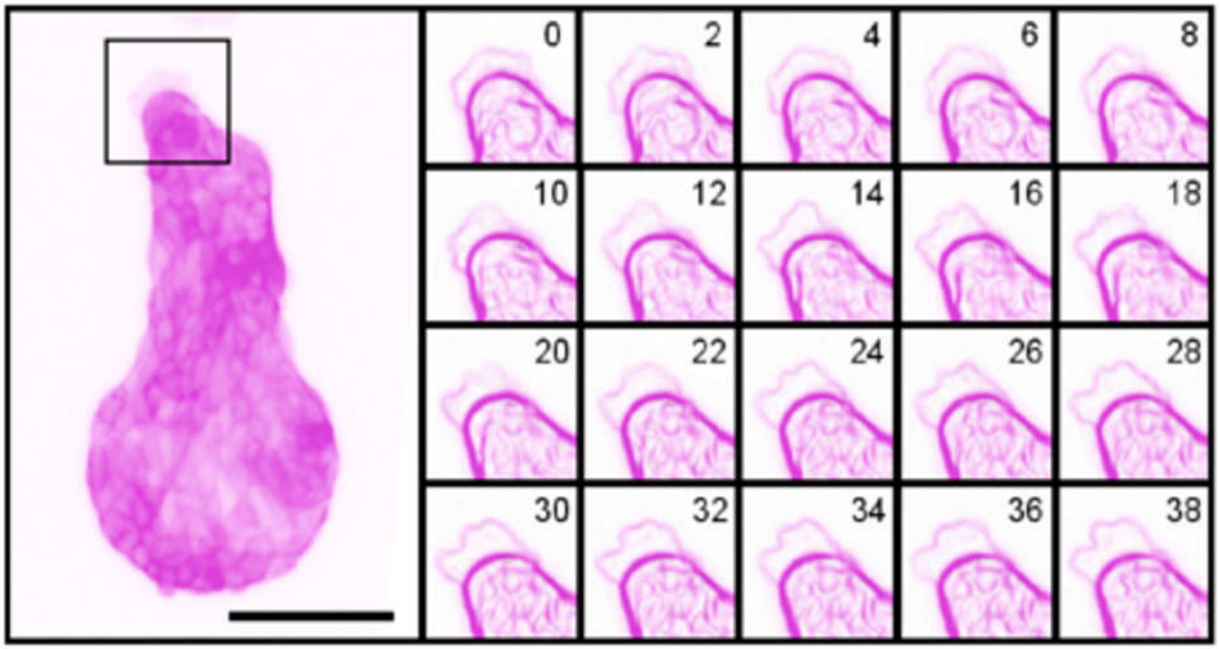

Figure 2: Protrusion dynamics of Lifeact-MDCK cells on micro-patterns, again with the colour information inverted to turn green-on-black into magenta-on-white, for clarity. Images of micro-patterned cells were captured every 2 minutes using a 10x objective, and showed irregular, dynamic protrusions at different regions of the periphery. A time-series of a 75 μm-by-75 μm square (marked in the main panel), using ImageJ's built-in Edge Detection algorithm to highlight sharp changes in intensity, shows the fluctuations of a typical protrusion. Some protrusions were very stable over time, though they changed shape as shown here, whereas others appeared and disappeared within a handful of frames. Scale bar = 100 μm.

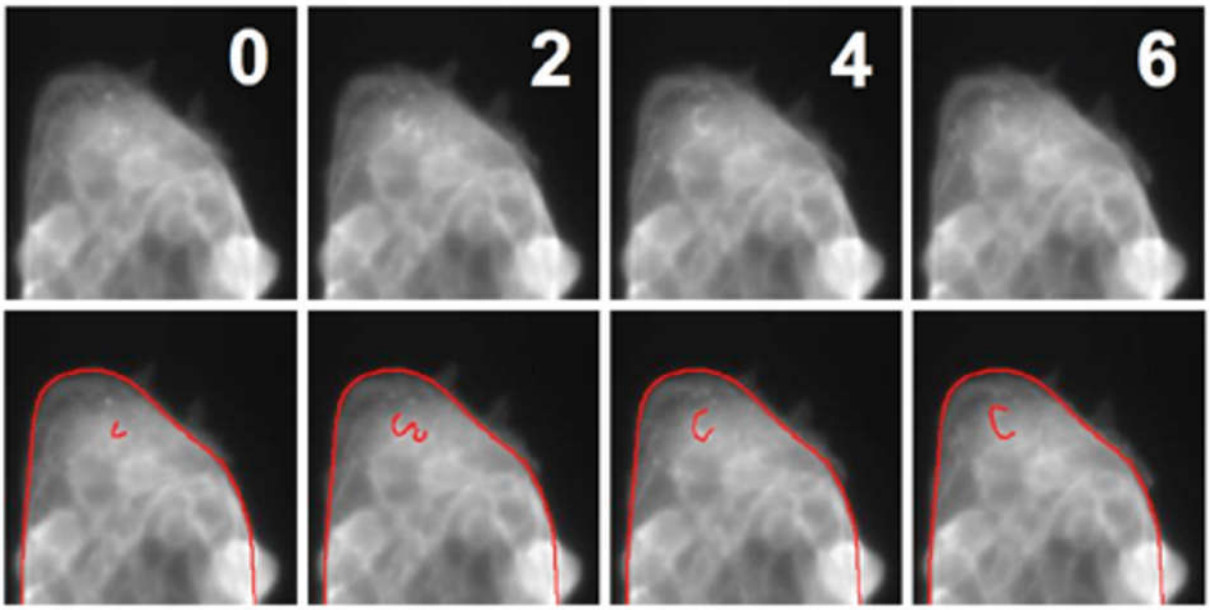

Figure 3: Apical ruffles in live imaged micro-patterned cells. Images of micro-patterned Lifeact-MDCK cells were captured every 2 minutes using a 20x objective, and showed evidence of apical surface ruffles driven by actin dynamics. A time-series of the edge of a micro-pattern (segments V2, C3, and V3 in a 100 μm-by-100 μm square region) is shown, with a typical ruffle highlighted manually in the lower panels.

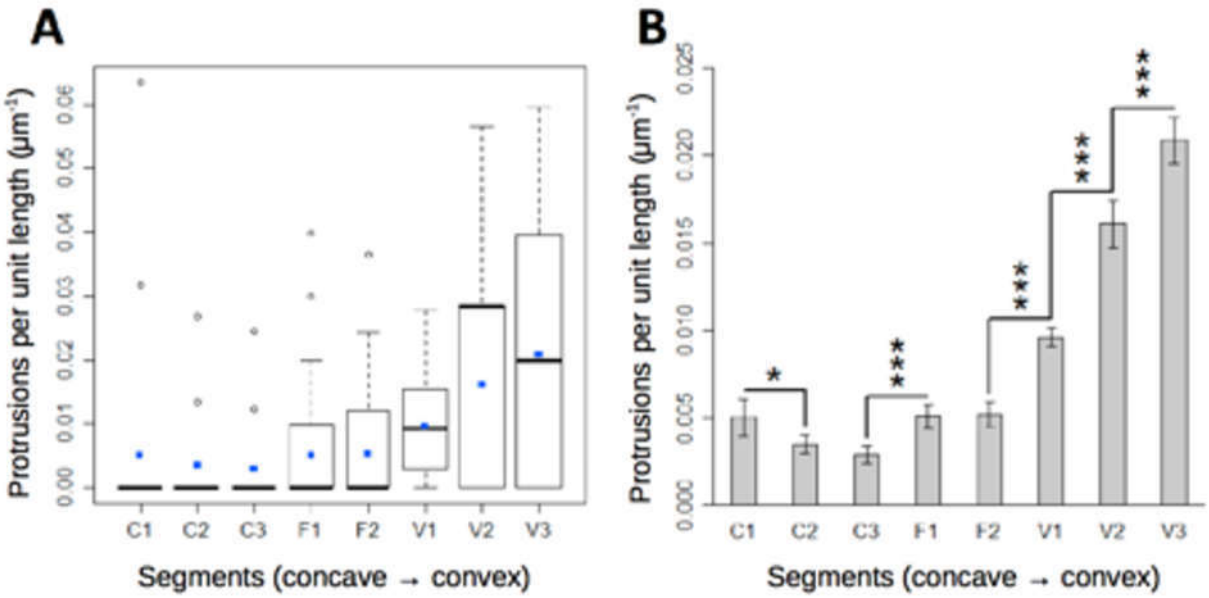

Figure 4: Relationship between curvature and protrusion rate. (A) Tukey box plot of the distribution of protrusion rates by segment. Blue points represent mean values, the bar the median, whiskers extend to outliers up to 1.5x IQR and further outliers are marked as open spots. (B) Protrusion rates (mean with error bars representing 95% confidence interval) show a strong positive trend with curvature, with significance (p-values calculated using an exact Poisson rate ratio test) indicated by stars; * = $p<0.05$; ** = $p < 0.01$; *** = $p < 0.001$.

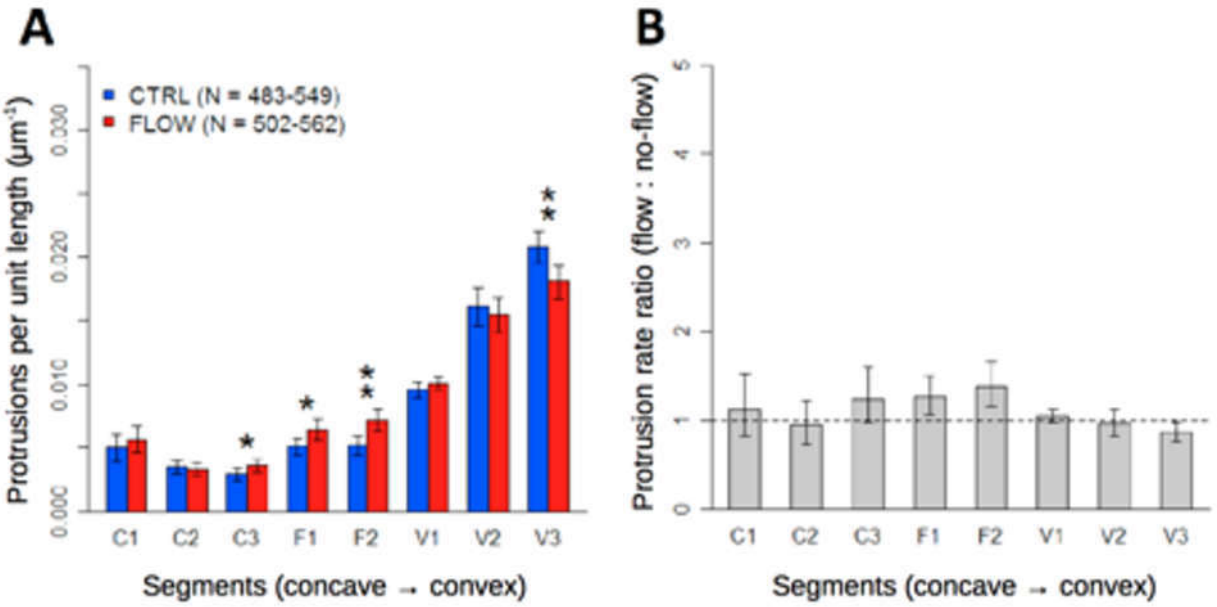

Figure 5: Flow conditions fail to disrupt the relationship between curvature and protrusion. (A) Protrusion rates (mean with error bars depicting 95% confidence interval) show a strong positive trend with curvature, with only minor variations between the control and flow conditions (stars indicate significant p-values from Mann-Whitney-Wilcoxon test: * = $p<0.05$; ** = $p < 0.01$). (B) Shows the same data expressed as a ratio between experiment and control, to emphasize the similarity of these sample groups.